Multi-Scale Modeling and Simulation in Configurational Mechanics

vom Fachbereich Maschinenbau und Verfahrenstechnik
der Technischen Universität Kaiserslautern
zur Verleihung des akademischen Grades
Doktor-Ingenieur (Dr.-Ing.)
genehmigte Dissertation

von
Dipl.-Math. techn. Sarah Ricker
aus Kaiserslautern

Hauptreferent:	Prof. Dr.-Ing. R. Müller
Korreferenten:	Prof. Dr.-Ing. P. Steinmann
	Prof. Dr.-Ing. R. Kienzler
	JP Dr.-Ing. J. Mergheim
Vorsitzender:	Prof. Dr.-Ing. E. Kerscher
Dekan:	Prof. Dr.-Ing. S. Ripperger
Tag der Einreichung:	17. November 2010
Tag der mündlichen Prüfung:	17. Februar 2011

Kaiserslautern, Mai 2011

D 386

Herausgeber
Lehrstuhl für Technische Mechanik
Technische Universität Kaiserslautern
Gottlieb-Daimler-Straße
Postfach 3049
67653 Kaiserslautern

Ich danke der „Prof. Dr. Hans Georg und Liselotte Hahn Stiftung" für die finanzielle Unterstützung bei der Drucklegung.

Druck:

Technische Universität Kaiserslautern
ZBT –Abteilung Foto-Repro-Druck

ISBN 978-942695-02-2

Vorwort

Die vorliegende Arbeit entstand während meiner Zeit als Stipendiatin im DFG Graduiertenkolleg 814 *Ingenieurmaterialien auf verschiedenen Skalen: Experiment, Modellierung und Simulation* und in meiner Tätigkeit als wissenschaftliche Mitarbeiterin am Lehrstuhl für Technische Mechanik der TU Kaiserslautern von 2005 bis 2010.

Besonders herzlich bedanken möchte ich mich bei Herrn Professor Paul Steinmann für die Ermöglichung dieser Arbeit und die hervorragende Betreuung sowohl in Kaiserslautern als auch von Erlangen aus. Ebenso möchte ich mich bei Herrn Professor Ralf Müller für die Fortführung der Betreuung in Kaiserslautern und seine kreativen Ideen, die zum Gelingen dieser Arbeit beigetragen haben, bedanken. Frau Juniorprofessorin Julia Mergheim möchte ich danken für die intensive Beschäftigung mit meiner Arbeit und die daraus entstehende Motivation und konstruktive Kritik, ebenso wie für die gemeinsame Zeit als Zimmerkolleginnen. Weiterhin danke ich Herrn Professor Reinhold Kienzler für die Erstellung des Referates sowie Herrn Professor Eberhard Kerscher für die Übernahme des Vorsitzes.

Allen meinen Kollegen am LTM danke ich für die angehmene Atmosphäre, die nicht nur durch die Zusammenarbeit am LTM, sondern auch während Kaffeepausen und der einen oder anderen Abendveranstaltung entstand. Besonders hervorheben möchte ich die HNO-WG, bestehend aus Charlotte Kuhn, Carolin Plate und Markus Klassen, für das Korrekturlesen vor Einreichung und die Unterstützung beim anschließenden Drucken. Ebenso geht mein Dank an Frau Edeltraut Jeblick und Herrn Dr. Franz-Josef Barth für die Unterstützung bei allen organisatorischen Angelegenheiten.

Meiner Familie und Freunden danke ich für ihre Unterstützung während meiner gesamten Ausbildung. Abschließend (bevor es dann mit der Mechanik losgeht), möchte ich mich noch besonders bei Chriz bedanken, für die Unterstützung, die Motivation, die Ablenkung und das "Einfach-Da-Sein", egal um welche Uhrzeit.

Kaiserslautern, im Mai 2011 Sarah Ricker

Zusammenfassung

Ziel der vorliegenden Arbeit ist die Weiterentwicklung der numerischen Homogenisierung im Hinblick auf neue Problemstellungen. Das Hauptaugenmerk liegt hierbei auf der Entwicklung eines Homogenisierungansatzes zur Bestimmung makroskopischer materieller Größen, wie z.B. Eshelby Spannungstensoren oder materieller Rissspitzenkräfte, basierend auf einer zugrunde liegenden (heterogenen) Mikrostruktur. Ein weiterer Gegenstand dieser Arbeit ist die Homogenisierung aus Partikeln bestehender diskreter mikroskopischer Strukturen. Für diese diskreten Systeme werden zwei unterschiedliche Arten von Sklalenübergängen gegenübergestellt: Zum einen wird ein Skalenübergang analog zur kontinuierlichen Homogenisierung betrachtet, der auf der Vorgabe von Randdaten basiert. Zum anderen werden Systeme fokussiert bei denen im Rahmen der Cauchy-Born Regel alle Partikelpositionen fest vorgeschrieben sind. Weiterhin wird der Übergang zum Kontinuum betrachtet, dargestellt durch Systeme mit einer unendlichen Anzahl von Partikeln.

Die Anwendung von Homogenisierungsmethoden ist wie folgt motiviert:
In vielen Ingenieursanwendungen gewannen im Laufe der letzten Jahrzehnte Materialien mit komplexer Mikrostruktur immer mehr an Bedeutung. So sind z.B. Verbundwerkstoffe und poröse Materialien essentiell in Leichtbaukonstruktionen der Luftfahrt- und Fahrzeugtechnik. Diese Materialien profitieren einerseits von ihrem geringen Gewicht und andererseits von ihren enormen Steifigkeiten. Eine effektive Versteifung von Kompositen wird durch das Einbetten von diversen Fasern erzielt. Eine weitere wichtige Gruppe von mikrostrukturierten Materialien abseits der Ingenieurswerkstoffe sind biologische Materialien, wie Lungengewebe, Arterien oder Knochen, die somit auch Simulationsmethoden erfordern, welche die Mikrostruktur erfassen können.

Aufgrund der starken Abhängigkeit des makroskopischen Verhaltens von den mikroskopischen Eigenschaften, wie z.B. Anordnung und Volumenanteile von verschiedenen Materialien, Fasern oder Einschlüssen, ist es schwierig das makroskopische Materialverhalten im gesamten Simulationsgebiet durch konstitutive Annahmen zu beschreiben. Die hierfür benötigten Materialparameter müssen durch aufwändige Experimente für jede mögliche mikroskopische Anordnung neu bestimmt werden. Darüber hinaus sind die numerischen Kosten einer sehr feinen Auflösung der Mikrostruktur über das gesamte makroskopische Gebiet zu hoch, da Gleichungssysteme dieser Größenordnung mit derzeitigen CPUs nicht lösbar sind. Daher wurden verschiedene Mehrskalen- oder Homogenisierungsmethoden entwickelt, um makroskopische Materialeigenschaften aus der Analyse von

Mikrostrukturen zu gewinnen.

Die Basis der vorliegenden Arbeit ist das numerische Homogenisierungschema, welches einen direkten Makro-Mikro Übergang in jedem makroskopischen Simulationspunkt ausführt. In jedem dieser Simulationspunkte wird die Mikrostruktur in einem sogenannten repräsentativen Volumen Element (RVE) erfasst. Die benötigten makroskopischen Größen ergeben sich als Mittlung über Größen auf dem Rand der RVEs. Der Übergang von der Makro- zur Mikro-Skala kann im Rahmen der angewendeten Finiten Elemente Methode auf zwei Arten geschehen: Zum einen ist ein verzerrungsgesteuertes Vorgehen möglich, bei dem in jedem einzelnen makroskopischen Punkt der Deformationsgradient berechnet und an die Mikro-Skala übergeben wird. Zum anderen kann der Skalen-Übergang auch spannungsgesteuert ausgeführt werden, was zur Übergabe eines geeigneten Spannungsmaßes an die Mikro-Skala führt. Mit Hilfe von zulässigen Randbedingungen wird durch die übergebenen Größen ein mikroskopisches Randwertproblem definiert. Die Zulässigkeit von Randbedingungen ergibt sich für verzerrungsbasiertes Vorgehen aus dem "average strain therorem", welches die Äquivalenz des makroskopischen und des gemittelten Deformationsgradienten postuliert. Es wird gezeigt, dass das "average strain theorem" zu Verschiebungsrandbedingungen oder periodischen Randbedingungen führt. Analog wird für den spannungsbasierten Skalenübergang das "average stress theorem" formuliert, welches die Äquivalenz der makroskopischen und der gemittelten Spannungen fordert. Aus diesem Ansatz ergibt sich eine weitere zulässige Randbedingung, die sogenannten konstanten Randspannungen.

Nach dem Aufbringen der Randbedingungen wird in der vorliegenden Arbeit auch das mikroskopische Randwertproblem im Rahmen der Finiten Elemente Methode gelöst. Aufgrund des geschachtelten Lösungsalgorithmus, der auf zwei Finiten Element Simulationen basiert, wird dieses Vorgehen in der Literatur auch oft als FE^2 Schema bezeichnet. Ein Vorteil der angewandten Methode besteht aber darin, dass das numerische Homogenisierungsschema nicht auf eine FE Rechnung auf der Mikro-Ebene beschränkt ist, sondern auch andere Methoden wie Gitterstatik oder Molekulardynamik angewendet werden können. Ein weiterer Vorteil des verwendeten Schemas ist die Möglichkeit große Deformationen zu simulieren, welche dann ein iteratives Lösungsverfahren, wie z.B. die hier ausgeführte Newton-Raphson Iteration, benötigen. Des Weiteren ist die numerische Homogenisierung nicht auf ein elastisches Materialgesetz in der Mikroebene beschränkt. Auch zeit- oder pfadabhängige Materialverhalten wie Viskoelastitizität oder Plastizität können modelliert werden.

Der gesuchte Zusammenhang zwischen den gemittelten und den makroskopischen (räumlichen) Variablen ergibt sich aus der sogenannten Hill-Mandel Bedingung, welche die Gleichheit der gemittelten virtuellen Arbeit auf der Mikro-Skala und der makroskopischen virtuellen Arbeit im zugehörenden Simulationspunkt fordert. Im Gegensatz zu den Standardansätzen werden hier auch mikroskopische Volumenkräfte in die Betrachtungen einbezogen.

Basierend auf den erarbeiteten Konzepten werden Ansätze zur Bestimmung von

makroskopischen materiellen Größen, wie den Eshelby Spannungen, miteinander verglichen. Dazu werden periodische Randbedingungen in der räumlichen Homogenisierung vorausgesetzt, welche zum Verschwinden der räumlichen Volumenkräfte führen. In den vorliegenden Betrachtungen stellt die materielle Impulsbilanz keine von der räumlichen Impulsbilanz unabhängige Gleichung dar und muss somit nicht explizit gelöst werden. Es genügt daher, die materielle Homogenisierung als Postprozess zur räumlichen Homogenisierung auszuführen. Dazu werden zunächst die gemittelten materiellen Größen definiert, die im Gegensatz zu den räumlichen Größen, zusätzlich zu den Randintegralen, Grenzflächenbeiträge beinhalten. Diese Grenzflächenterme verschwinden bei der räumlichen Mittlung, da im Allgemeinen die räumliche Spannung über Grenzflächen hinaus kontinuierlich ist. Des Weiteren werden auch materielle Volumenkräfte berücksichtigt, die durch Inhomogenitäten auf der Mikro-Skala auftreten können, wie z.B. in einem gradierten mikroskopischen Material, wo somit eine Verzerrungsenergiefunktion berücksichtigt wird, welche explizit von den materiellen Koordinaten abhängt.

In einem nächsten Schritt werden verschiedene Ansätze zur Definition der makroskopischen Spannungen miteinander verglichen. Im ersten intuitiven Ansatz werden die makroskopischen Spannungen direkt als Funktion der bereits gemittelten räumlichen Größen aufgefasst. Zwei weitere Ansätze, basierend auf der Mittlung des Eshelby Spannungstensors und des materiellen Zwei-Feld-Spannungstensors, werden betrachtet. Die Konsistenz der aufgezeigten Ansätze wird anhand von materiellen Gegenstücken zur Hill-Mandel Bedingung überprüft.

Das erarbeitete materielle Homogenisierungsschema wird durch numerische Beispiele veranschaulicht, in denen der Einfluss verschiedener mikroskopischer Charakteristika auf die makroskopische materielle Rissspitzenkraft untersucht wird. In diesen Betrachtungen werden u.a. auch die verschiedenen Vorgehensweisen zur Definition der makroskopischen materiellen Spannungen verglichen.

Contents

1 Introduction

During the last decades, materials with an underlying microscopic structure have become important in a wide class of applications. Typical examples for such materials are composite materials for which the advantages of the single constituents are combined to obtain optimal material properties. Examples are polymer blends and porous media. These kinds of materials possess a wide application range in lightweight constructions, as e.g., requested in aeronautical engineering or in the construction of vehicles which should benefit from a low weight and a high stiffness. A further class of micro-structured materials is represented by biological tissues like bones, arteries or lung tissue. The macroscopic overall behavior of these materials strongly depends on the microscopic properties like the arrangement and volume fraction of different materials or cavities, or the orientation of embedded fibers. Therefore, the determination of the macroscopic effective material properties is a rather difficult task: On the one hand, they may be identified in a bunch of experiments which have to be performed for each single modification of the microscopic constituents. On the other hand, direct simulations which resolve the microscopic structure are computationally far too expensive. Therefore, various types of so-called multi-scale or homogenization approaches have been developed which determine the macroscopic material properties based on the analysis of the underlying micro-structure. To this end, in the work at hand a direct macro-micro transition is applied within the concept of numerical homogenization. The microscopic setting is captured in so-called representative volume elements (RVEs) which are attached to each macroscopic point. In the computational homogenization method applied here, the macroscopic strain (in case of a deformation-driven scheme) or the macroscopic stress (within a stress-driven scheme) is computed in each simulation point within a finite element scheme. By assistance of admissible boundary conditions, these strains or stresses are applied to the boundary of the RVE. The generated microscopic boundary value problem is then solved by an appropriate method, which in the work at hand is given by the finite element method. Nevertheless, the computational homogenization schemes are not restricted to finite element simulations on the micro-level, but also other simulation methods like lattice statics or molecular dynamics can be applied. In a next step, after the solution of the microscopic boundary value problem, the averaging process is carried out. Therefore, the required macroscopic variables like stresses in the deformation-driven scheme and strains in the stress-driven scheme are determined by means of boundary terms of the microscopic RVE. Additionally, the macroscopic tangent modulus is calculated.

One of the main advantages of the applied computational homogenization scheme

is given by its applicability to large deformations which results in an iterative solution scheme, as e.g., given by the Newton-Raphson scheme, on the macro- as well as on the micro-level. A further advantage is the possibility to model a wide range of microscopic material behaviors, such as hyperelasticity, visco-elasticity or plasticity.

The main goal of the current work is the extension of the classical homogenization scheme towards the homogenization of variables resulting from the material motion problem which is inverse to the spatial motion problem. Therefore, volume forces which are normally neglected in the homogenization process have to be taken into account. Configurational (or material) volume forces may occur due to inhomogeneities in the material. With the help of the homogenized Eshelby stress tensor, it is possible to determine macroscopic configurational node point forces depending on the underlying microscopic structure. These node point forces represent defect driving forces. For example the configurational force at a crack tip corresponds to the J-integral introduced by Rice in [70]. Thus, the magnitude of the configurational crack tip force yields a criterion whether a crack propagates depending on the underlying microscopic structure. Likewise, the driving force on a single dislocation in a crystal, which is represented by the Peach-Köhler force, can be obtained in terms of material quantities.

In order to determine these material node point forces numerically, different approaches for the definition of the macroscopic Eshelby stress are given and compared with regard to a Hill-Mandel type condition which claims the equivalence of the averaged microscopic virtual work and the macroscopic virtual work in each material point. Furthermore, the different approaches are compared by numerical studies on the influence of different microscopic properties onto the macroscopic crack tip force.

Another concern in the present work is the applicability of the computational homogenization scheme to discrete micro-structures which are here represented by discrete particle systems, but which can also be treated as atomistic systems. To this end, the discrete analogues to the principle of virtual work, the averaging of variables and different approaches for the scale-transition are elaborated

The work at hand is divided into five parts. To set the stage, in the following chapter the kinematics and the balance equations are summarized for the spatial as well as for the material motion problem. Here, it is assumed that the material balance of momentum follows from the spatial balance of momentum and thus does not state an independent equilibrium equation which has to be solved explicitly. Nevertheless, it allows the determination of the desired material node point forces. Furthermore, the applied constitutive laws are outlined. In order to solve the governing equations numerically within the finite element scheme, the variational (or weak form) and the corresponding discretization and linearization are given.

In Chapter 3, the computational homogenization scheme for the spatial motion problem is reviewed. For this purpose, the required averaged variables and the scale-transition for the strain- and the stress-driven procedure are defined. In a next step, admissible boundary conditions are developed based on the average strain

theorem for the strain-driven scheme or based on the average stress theorem for the stress-driven scheme, respectively. The average strain theorem results in displacement or periodic boundary conditions, whereas the average stress theorem yields the traction boundary conditions. Based on these boundary conditions, the Hill-Mandel condition is applied to yield the consistent scale-transitions by means of the virtual work. Macroscopic variables are derived. In contrast to the standard formulations the focus is also put on microscopic volume forces. Finally, the spatial homogenization scheme is illustrated by various numerical examples which investigate the influence of different boundary conditions and different RVEs on the macroscopic material response.

The extension of the standard computational homogenization scheme towards the homogenization of material quantities is carried out in Chapter 4. Therefore, initially the required averages of the material variables are defined properly. In contrast to the spatial homogenization it is not sufficient to define the averages only in terms of boundary integrals but also interface integrals have to be incorporated due to the discontinuity of material tractions across interfaces. Then, different approaches for the definition of the macroscopic material stresses are given and their consistency with respect to a Hill-Mandel type condition is checked. Therein, material volume forces which occur due to graded micro-materials, i.e., materials where the strain energy functional depends explicitly on the material coordinates, are concerned. The different approaches and the influence of different microscopic properties on the macroscopic material quantities are investigated by illustrative numerical examples.

The self-contained Chapter 5 deals with a further extension of the (spatial) computational homogenization scheme represented by the homogenization of discrete particle systems. The focus is mainly put on two approaches for the scale-transition from the macro- to the micro-level. Unconstrained particle systems for which the scale-transition is performed via periodic boundary conditions are compared to Cauchy-Born constrained systems for which all particle positions are prescribed. The governing equations for these approaches are presented and the approaches are compared within numerical studies.

A conclusion of the results obtained and an outlook to possible future work finalizes the work in Chapter 6. Additionally, helpful auxiliary derivations are summarized in Appendices A, B and C.

2 Continuum Mechanics: A brief Overview

To set the stage, in the following section the kinematics and balance equations are reviewed for the spatial, as well as for the material motion problem. It is not distinguished between the micro- and the macro-level here, since the format of the kinematics and the quasi-static equilibrium equations are valid for both scales. But it is mentioned that in the following chapters which incorporated multi-scale mechanics, the constitutive assumption, which yields the connection between the stresses and the strains, will only be stated on the micro-level. The macroscopic material response is then directly determined in terms of the response of the micro-level.

In the current chapter, the spatial motion parts are mainly based on the textbooks by Ogden [68], Holzapfel [39] and Betten [5], while the parts concerning the material motion problem are based on the textbooks by Maugin [55], Gurtin [29] and Kienzler and Herrmann [45], and the publications by Steinmann [82], Müller and Maugin [64], Denzer et al. [12], Kuhl et al. [53].

Furthermore, the constitutive laws which are applied in the work at hand are reviewed.

2.1 Kinematics

In the sequel, the kinematics of the non-linear spatial and material motion problem are summarized.

2.1.1 Kinematics of the Spatial Motion Problem

The spatial motion problem, see Figure 2.1, is connected to the non-linear deformation map $\boldsymbol{\varphi}$, which maps the position of points $\boldsymbol{X}$ in the reference configuration $\mathscr{B}_0$ to their position in the current configuration $\mathscr{B}_t$, i.e.,

$$\boldsymbol{x} = \boldsymbol{\varphi}(\boldsymbol{X}). \tag{2.1}$$

The gradient of the spatial deformation map yields the spatial deformation gradient and its Jacobian as

$$\boldsymbol{F} = \nabla_{\boldsymbol{X}} \boldsymbol{\varphi} \quad \text{and} \quad J = \det \boldsymbol{F} > 0. \tag{2.2}$$

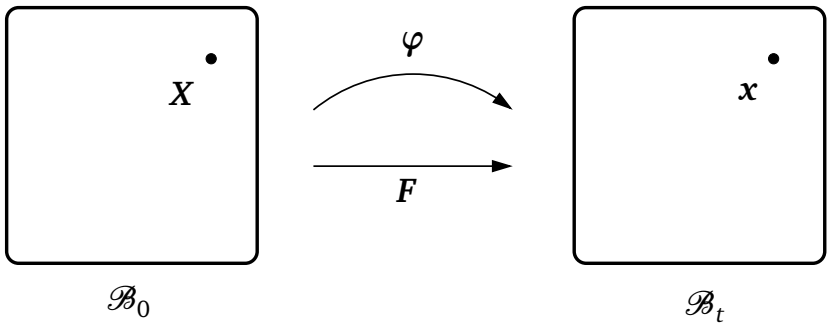

Figure 2.1: Kinematics of the spatial motion problem

Thereby, $\nabla_{\boldsymbol{X}}(\bullet)$ denotes the gradient of a scalar- or vector-valued function with respect to the material positions, i.e., $\nabla_{\boldsymbol{X}}(\bullet) = \dfrac{\partial \bullet}{\partial \boldsymbol{X}}$. The fact that the Jacobian does not equal zero guarantees the invertibility of $\boldsymbol{F}$. Furthermore, the following relation between infinitesimal volume elements $\mathrm{d}v$ in the current and $\mathrm{d}V$ in the reference configuration is valid

$$\mathrm{d}v = J\,\mathrm{d}V, \tag{2.3}$$

which yields that $J > 0$ corresponds to the impenetrability of matter, i.e., two particles cannot occupy the same space at the same time, and thus volume elements cannot have negative volumes. The connection between area elements

$$\mathrm{d}\boldsymbol{a} = \boldsymbol{n}\,\mathrm{d}a \quad \text{and} \quad \mathrm{d}\boldsymbol{A} = \boldsymbol{N}\,\mathrm{d}A, \tag{2.4}$$

whereby $\boldsymbol{N}$ and $\boldsymbol{n}$ define the outward unit normal vectors to the material and the spatial boundary, respectively, is given by the Nanson's formula

$$\mathrm{d}\boldsymbol{a} = J\,\boldsymbol{F}^{-t} \cdot \mathrm{d}\boldsymbol{A}. \tag{2.5}$$

The proof of (2.5) can be found, e.g., in the textbook by Ogden [68].

Furthermore, appropriate deformation measures are introduced in terms of the right and the left spatial motion Cauchy-Green strain tensors as

$$\boldsymbol{C} = \boldsymbol{F}^t \cdot \boldsymbol{F} \quad \text{and} \quad \boldsymbol{b} = \boldsymbol{F} \cdot \boldsymbol{F}^t. \tag{2.6}$$

In contrast to the deformation gradient tensor these deformation measures are symmetric in general, and they do not take rigid body motions into account, i.e., for rigid body motions it holds $\boldsymbol{C} = \boldsymbol{b} = \boldsymbol{I}$, whereby $\boldsymbol{I}$ corresponds to the second order unit tensor. A symmetric strain measure, which equals zero in case of rigid body motions, is given by the Green-Lagrange strain

$$\boldsymbol{E} = \frac{1}{2}\left[\boldsymbol{C} - \boldsymbol{I}\right]. \tag{2.7}$$

2.1.2 Kinematics of the Material Motion Problem

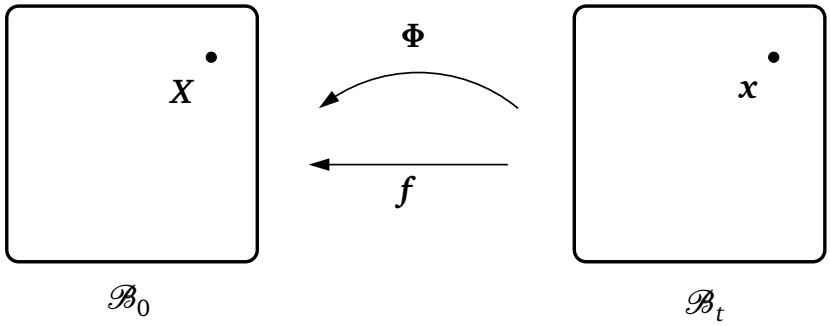

Figure 2.2: Kinematics of the material motion problem

The material motion (or inverse motion) problem, see Figure 2.2, is connected to the non-linear (inverse) deformation map $\boldsymbol{\Phi}$, which maps the position of points $\boldsymbol{x}$ in the current configuration $\mathscr{B}_t$ to their position in the reference configuration $\mathscr{B}_t$, i.e.,

$$\boldsymbol{X} = \boldsymbol{\Phi}(\boldsymbol{x}). \tag{2.8}$$

The following identities emerge from the definitions of the spatial and the material map

$$\boldsymbol{id}_{\mathscr{B}_0} = \boldsymbol{\Phi}(\boldsymbol{\varphi}(\boldsymbol{X})) \quad \text{and} \quad \boldsymbol{id}_{\mathscr{B}_t} = \boldsymbol{\varphi}(\boldsymbol{\Phi}(\boldsymbol{x})). \tag{2.9}$$

The gradient of the material deformation map yields the deformation gradient and its determinant

$$\boldsymbol{f} = \nabla_{\boldsymbol{x}} \boldsymbol{\Phi} \quad \text{and} \quad j = \det \boldsymbol{f} > 0. \tag{2.10}$$

Therein, $\nabla_{\boldsymbol{x}}(\bullet)$ corresponds to the gradient of a scalar- or vector-valued function with respect to the spatial positions, i.e., $\nabla_{\boldsymbol{x}} = \dfrac{\partial \bullet}{\partial \boldsymbol{x}}$ is valid. The connection between the spatial and the material motion gradient is given by

$$\boldsymbol{f}^{-1} = \boldsymbol{F}(\boldsymbol{\Phi}(\boldsymbol{x})) \quad \text{and} \quad \boldsymbol{F}^{-1} = \boldsymbol{f}(\boldsymbol{\varphi}(\boldsymbol{X})). \tag{2.11}$$

In analogy to the spatial motion problem, the material right and left Cauchy-Green strain tensors are defined via

$$\boldsymbol{c} = \boldsymbol{f}^t \cdot \boldsymbol{f} \quad \text{and} \quad \boldsymbol{B} = \boldsymbol{f} \cdot \boldsymbol{f}^t. \tag{2.12}$$

Then, the relation between the spatial and material deformation tensor is given by

$$\boldsymbol{C}^{-1} = \boldsymbol{B} \quad \text{and} \quad \boldsymbol{b}^{-1} = \boldsymbol{c}. \tag{2.13}$$

The material analogon to the Green-Lagrange strain is given by the Euler-Almansi strain tensor

$$\boldsymbol{e} = \frac{1}{2}\left[\boldsymbol{I} - \boldsymbol{c}\right]. \tag{2.14}$$

2.2 Balance Equations and Stress Measures

In the following, different stress measures and the corresponding balance equations are reviewed for the spatial and the material motion problem. Furthermore, pull-back and push-forward operations between the stress measures in the different configurations and the related forces are given. In the subsequent sections div $(\bullet)$ corresponds to the divergence operator with the respect to spatial coordinates $\boldsymbol{x}$, whereas Div$(\bullet)$ denotes the divergence with respect to to material coordinates $\boldsymbol{X}$.

2.2.1 Kinetics of the Spatial Motion Problem

The quasi-static balance of momentum for the spatial motion problem, which ensures the equilibrium of internal and external (physical) forces, reads

$$-\mathrm{Div}\,\boldsymbol{P} = \boldsymbol{b}_0 \quad \Rightarrow \quad -\mathrm{div}\,\boldsymbol{\sigma} = \boldsymbol{b}_t. \tag{2.15}$$

Thereby, $\boldsymbol{P}$ denotes the first Piola-Kirchhoff (or nominal or simply Piola) stress tensor, which yields a two-point stress measure, and $\boldsymbol{\sigma}$ the Cauchy (or true) stress tensor, which provides a stress measure in spatial description. Please note, that in case of a Boltzmann continuum, which is a non-polar continuum, the Cauchy stress tensor is symmetric. Furthermore, $\boldsymbol{b}_0$ and $\boldsymbol{b}_t$ correspond to the spatial volume forces per undeformed or deformed unit volume, respectively.

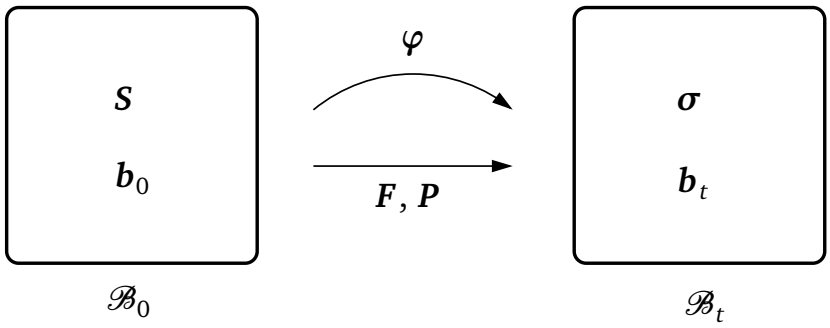

Figure 2.3: Kinetics of the spatial motion problem

The relation between the different stress measures and the volume forces is given by the push-forward operations

$$\boldsymbol{\sigma} = J^{-1}\,\boldsymbol{P}\cdot\boldsymbol{F}^t \quad \text{and} \quad \boldsymbol{b}_t = J^{-1}\,\boldsymbol{b}_0. \tag{2.16}$$

The spatial Piola tractions (force measured per unit surface area in the material configuration) and the Cauchy tractions (force measured per unit surface area in the spatial configuration) are given as

$$\boldsymbol{t}_0 = \boldsymbol{P}\cdot\boldsymbol{N} \quad \text{and} \quad \boldsymbol{t}_t = \boldsymbol{\sigma}\cdot\boldsymbol{n}. \tag{2.17}$$

For the sake of completeness, the second Piola-Kirchhoff stress is introduced as

$$\boldsymbol{S} = \boldsymbol{F}^{-1} \cdot \boldsymbol{P}, \tag{2.18}$$

which yields a symmetric spatial stress measure in pure material description.

Finally, the set of governing equations is completed by the constitutive equation that connects the stresses and the strains by means of the energy density $U_0 = U_0(\boldsymbol{\varphi}, \boldsymbol{F}; \boldsymbol{X})$ via

$$\boldsymbol{P} = \frac{\partial U_0}{\partial \boldsymbol{F}}. \tag{2.19}$$

or formulated in terms of the Cauchy stress

$$\boldsymbol{\sigma} = U_t \boldsymbol{I} - \boldsymbol{f}^t \cdot \frac{\partial U_t}{\partial \boldsymbol{f}}, \tag{2.20}$$

with

$$U_t = U_t(\boldsymbol{\Phi}, \boldsymbol{f}; \boldsymbol{x}) = j\, U_0. \tag{2.21}$$

Furthermore, for conservative systems the volume forces are given in terms of the energy density as

$$\boldsymbol{b}_0 = -\frac{\partial U_0}{\partial \boldsymbol{x}} \quad \text{and} \quad \boldsymbol{b}_t = -\frac{\partial U_t}{\partial \boldsymbol{x}}. \tag{2.22}$$

2.2.2 Kinetics of the Material Motion Problem

The quasi-static balance of momentum for the material motion problem, which guarantees the equilibrium of internal and external (configurational) forces, is given by

$$-\operatorname{div} \boldsymbol{p} = \boldsymbol{B}_t \quad \Rightarrow \quad -\operatorname{Div} \boldsymbol{\Sigma} = \boldsymbol{B}_0. \tag{2.23}$$

Thereby, $\boldsymbol{p}$ corresponds to the material two-point (or first Piola-Kirchhoff) stress and $\boldsymbol{\Sigma}$ represents a material stress measure in pure material description, which is often referred to as Eshelby stress tensor. In contrast to its spatial counterpart, the Eshelby stress tensor is in general not symmetric in Boltzmann continua as, e.g., in an anisotropic material the Eshelby stress can become unsymmetric. The configurational volume forces per undeformed or deformed unit volume are denoted by $\boldsymbol{B}_0$ and $\boldsymbol{B}_t$. Please note, that in the work at hand the material quasi-static balance of momentum does not state an independent equilibrium condition. It is equivalent to the spatial quasi-static balance of momentum and can be obtained by pre-multiplying (2.15) with $\boldsymbol{F}^t$ or $\boldsymbol{f}^t$, respectively, and straight-forward computation. Thus, the quasi-static balance of momentum is not solved explicitly, here.

The material Piola tractions and the Eshelby tractions are defined by the projection of the material two-point stress or the Eshelby stress, respectively, onto the corresponding outward unit normal, i.e.,

$$\boldsymbol{T}_t := \boldsymbol{p} \cdot \boldsymbol{n} \quad \text{and} \quad \boldsymbol{T}_0 := \boldsymbol{\Sigma} \cdot \boldsymbol{N}. \tag{2.24}$$

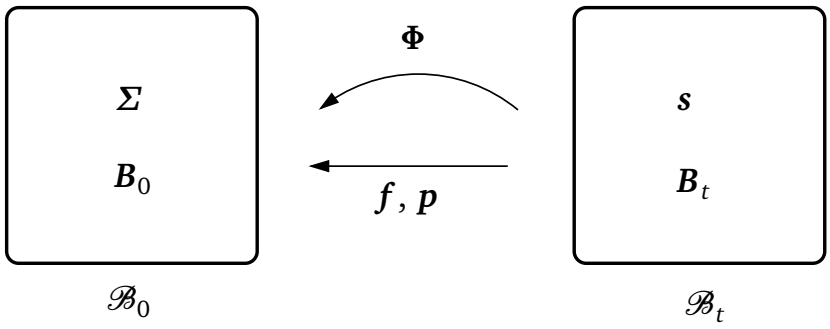

Figure 2.4: Kinetics of the material motion problem

The relations between the different stress measures and the volume forces are given by the pull-back operations

$$\boldsymbol{\Sigma} = J\,\boldsymbol{p}\cdot\boldsymbol{f}^{t} \quad \text{and} \quad \boldsymbol{B}_0 = J\,\boldsymbol{B}_t. \tag{2.25}$$

For the sake of completeness, the material second Piola-Kirchhoff stress, which provides a material stress measure in pure spatial description, is defined as

$$\boldsymbol{s} = \boldsymbol{f}^{-1}\cdot\boldsymbol{p}. \tag{2.26}$$

The constitutive assumption, which connects the stresses and the strains in terms of a stored energy functional completes the set of governing equations for the material motion problem. In terms of the material two-point stress the constitutive equation is given as

$$\boldsymbol{p} = \frac{\partial U_t}{\partial \boldsymbol{f}}, \tag{2.27}$$

while in terms of the Eshelby stress the constitutive assumption reads

$$\boldsymbol{\Sigma} = U_0\,\boldsymbol{I} - \boldsymbol{F}^{t}\cdot\frac{\partial U_0}{\partial \boldsymbol{F}}. \tag{2.28}$$

In case of a conservative system the volume forces may also be described in terms of the energy density via

$$\boldsymbol{B}_t = -\frac{\partial U_t}{\partial \boldsymbol{X}} \quad \text{and} \quad \boldsymbol{B}_0 = -\frac{\partial U_0}{\partial \boldsymbol{X}}. \tag{2.29}$$

Remark 1 *The connection between the spatial and the material stress measures is given through*

$$\boldsymbol{\sigma} = U_t\,\boldsymbol{I} - \boldsymbol{f}^{t}\cdot\boldsymbol{p} \quad \textit{and} \quad \boldsymbol{\Sigma} = U_0\,\boldsymbol{I} - \boldsymbol{F}^{t}\cdot\boldsymbol{P}. \tag{2.30}$$

2.3 Constitutive Laws

In the following, the free energies U_0 per reference unit volume or shortly the strain energy functions are summarized for the material laws used in the work at hand.

2.3.1 Neo-Hooke Hyperelasticity

The Neo-Hookean constitutive law yields an ansatz to model hyperelastic material behavior at large strains, which is sufficient to model and simulate many engineering materials. In case of a geometrical linear behavior the Neo-Hooke law reduces to the classical law of linear elasticity. In the work at hand, we restrict ourselves to an isotropic format of the Neo-Hooke law, i.e., the material possesses the same properties in all directions. Furthermore, a compressible material is modeled, i.e., the material may change its volume due to the applied deformation. For this cases the strain energy of the Neo-Hooke material is given by

$$U_0 = \frac{1}{2}\lambda \ln^2 J + \frac{1}{2}\mu \left[\left[\boldsymbol{F} \cdot \boldsymbol{F}^t \right] : \boldsymbol{I} - n^{\text{dim}} - 2\ln J \right]. \tag{2.31}$$

Thereby, λ and μ represent the so-called Lamé constants which are related to the Young's modulus and the Poisson's ratio in the following way

$$\lambda = \frac{\nu\, E}{(1+\nu)\,(1-2\nu)} \quad \text{and} \quad \mu = \frac{E}{2(1+\nu)}, \tag{2.32}$$

see, e.g., the book by Bonet and Wood [6] for details. Furthermore, n^{dim} corresponds to the dimension of the considered problem, i.e., $n^{\text{dim}} = 1, 2, 3$. By application of equation (2.19) the first Piola Kirchhoff stress for the Neo-Hooke material results in

$$\boldsymbol{P} = \frac{\partial U_0}{\partial \boldsymbol{F}} = \left[\lambda \ln J - \mu\right] \boldsymbol{F}^{-t} + \mu \boldsymbol{F}. \tag{2.33}$$

Thus, the push-forward operation as given in equation (2.16) yields the Cauchy stress as

$$\boldsymbol{\sigma} = J^{-1} \left[\lambda \ln J - \mu\right] \boldsymbol{I} + J^{-1} \mu \boldsymbol{b}. \tag{2.34}$$

In the one-dimensional case the strain energy function of the Neo-Hooke material simplifies to

$$U_0 = \frac{1}{4} E \left[F^2 - 1 - 2\ln(F) \right], \tag{2.35}$$

and thus the Piola stress reads

$$P = \frac{1}{2} E \left[F - \frac{1}{F} \right]. \tag{2.36}$$

A graphical illustration of the stress-stretch relation for the Neo-Hooke material is given in Figure 2.5.

Furthermore, the strain energy function per deformed unit volume can be formulated in terms of the material deformation gradient tensor via

$$U_t = \frac{1}{2} j \lambda \ln^2 \frac{1}{j} + \frac{1}{2} j \mu \left[\left[\boldsymbol{f}^{-1} \cdot \boldsymbol{f}^{-t} \right] : \boldsymbol{I} - n^{\text{dim}} - 2 \ln \frac{1}{j} \right]. \tag{2.37}$$

The material two-point stress for the Neo-Hooke material then results according to equation (2.27) in

$$\boldsymbol{p} = \left[U_t - j \lambda \ln J + j \mu \right] \boldsymbol{F}^t - j \mu \boldsymbol{C} \cdot \boldsymbol{F}^t, \tag{2.38}$$

which by application of the pull-back as given in (2.25) yields the Eshelby stress

$$\boldsymbol{\Sigma} = \left[U_0 - \lambda \ln J + \mu \right] \boldsymbol{I} - \mu \boldsymbol{C}. \tag{2.39}$$

For further details on the spatial and material formulation of the strain energy function and the corresponding stress measures the reader is referred to the work of Kuhl et al. [53].

2.3.2 St. Venant-Kirchhoff Hyperelasticity

The St. Venant-Kirchhoff material is an extension of linear elastic laws to large deformations, for details see, e.g., the textbook on nonlinear finite elements by Belytschko et al. [2]. The strain energy function of the St. Venant-Kirchhoff hyperelasticity is given in terms of the Green-Lagrange strain as

$$U_0 = \frac{1}{2} \boldsymbol{E} : \mathbb{C} : \boldsymbol{E}, \tag{2.40}$$

wherein $\mathbb{C}$ is in general a constant fourth-order tensor which contains the elastic constants. The corresponding second Piola-Kirchhoff stress is given by

$$\boldsymbol{S} = \mathbb{C} : \boldsymbol{E}. \tag{2.41}$$

For an isotropic material the strain energy of the St. Venant-Kirchhoff material can be formulated in terms of the Lamé constants as

$$U_0 = \frac{\lambda}{2} [\ \text{tr}\ (\boldsymbol{E})]^2 + \mu\ \text{tr}\ (\boldsymbol{E}^2), \tag{2.42}$$

which yields the corresponding second Piola-Kirchhoff stress as

$$\boldsymbol{S} = \lambda\ \text{tr}\ (\boldsymbol{E})\, \boldsymbol{I} + 2\mu \boldsymbol{E}. \tag{2.43}$$

The elasticity tensor $\mathbb{C}$ is derived via

$$\mathbb{C} = \frac{\partial \boldsymbol{S}}{\partial \boldsymbol{E}} = \lambda\, \boldsymbol{I} \otimes \boldsymbol{I} + 2\, \mu\, \boldsymbol{I}^{\text{sym}}, \tag{2.44}$$

wherein $\boldsymbol{I}^{\text{sym}}$ denotes the symmetric fourth-order unit tensor, i.e., it holds

$$\begin{aligned} \boldsymbol{I}^{\text{sym}} &= \frac{1}{2}\left[\boldsymbol{I}\overline{\otimes}\boldsymbol{I} + \boldsymbol{I}\underline{\otimes}\boldsymbol{I}\right] \\ I^{\text{sym}}_{IJKL} &= \frac{1}{2}\left[\delta_{IK}\,\delta_{JL} + \delta_{IL}\,\delta_{JK}\right]. \end{aligned} \tag{2.45}$$

Thereby, $\overline{\otimes}$ and $\underline{\otimes}$ denote the non-standard dyadic products which are defined via

$$\begin{aligned} A_{IJKL} &= \boldsymbol{B}\,\overline{\otimes}\,\boldsymbol{D} &&= B_{IK}\,D_{JL} \\ C_{IJKL} &= \boldsymbol{B}\,\underline{\otimes}\,\boldsymbol{D} &&= B_{IL}\,D_{JK}. \end{aligned} \tag{2.46}$$

An advantage of the St. Venant-Kirchhoff elasticity is given by its simple format due to its strain energy functional which is quadratic in $\boldsymbol{E}$ and thus yields a constant elasticity tensor, which does not depend on the applied deformation.

In the one-dimensional case the second Piola-Kirchhoff stress for the St. Venant-Kirchhoff law can be formulated in terms of the deformation gradient as

$$S = \frac{1}{2}E\left[F^2 - 1\right], \tag{2.47}$$

and thus the first Piola-Kirchhoff stress reads

$$P = \frac{1}{2}\left[F^3 - F\right]. \tag{2.48}$$

The stress-stretch relations for the first Piola-Kirchhoff stress of the one-dimensional Neo-Hooke law and the St. Venant-Kirchhoff law are displayed in Figure 2.5.

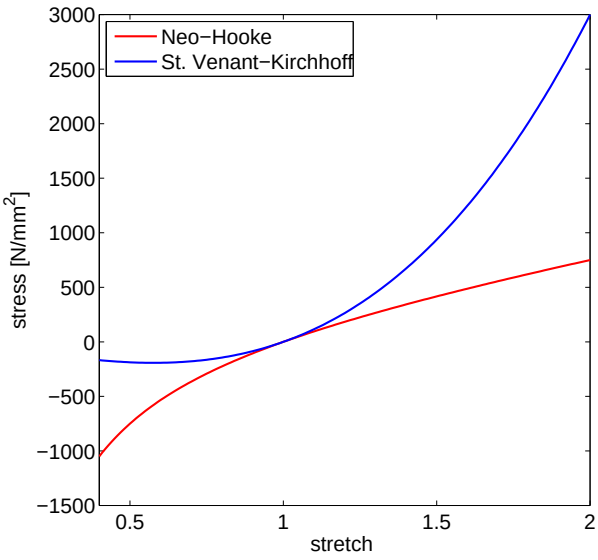

Figure 2.5: Comparison of first Piola Kirchhoff stress (ploted over stretch) for Neo-Hooke and St. Venant-Kirchhoff material

On the one hand this stress-stretch relations show that in contrast to the Neo-Hooke elasticity the St. Venant-Kirchhoff material law yields much bigger stresses for applied tensile load. On the other hand it can be shown that the energy of the St. Venant-Kirchoff material tends to zero in case of a stretch near zero, i.e., under compression, which is a rather unphysical behavior.

2.3.3 Damage Coupled to Hyperelasticity

In the work at hand, a damage model is coupled to a hyperelastic material of the Neo-Hooke type as defined in Section 2.3.1. This damage formulation is according to the work of Simo and Ju [79], [80] and incorporates the effective stress concept introduced by Kachanov in [42]. Due to the fact that here the damage formulation is applied to truss elements, only the one-dimensional formulation is given. In the model at hand, the degradation of material parameters is captured by an internal damage variable which due to the assumed isotropy of the material corresponds to a scalar $d(t) \in [0; d_c]$. Thereby, $d = 0$ describes an undamaged state, $0 < d < d_c$ a damaged state and $d = d_c$ complete local rupture. In the following, the strain equivalence hypothesis, see Lemaitre [54], is assumed, which is given by

> "the strain associated with a damaged state under the applied stress is equivalent to the strain associated with its undamaged state under the effective stress".

That is

$$\epsilon^* = \epsilon. \tag{2.49}$$

The strain equivalence hypothesis is illustrated in Figure 2.6.

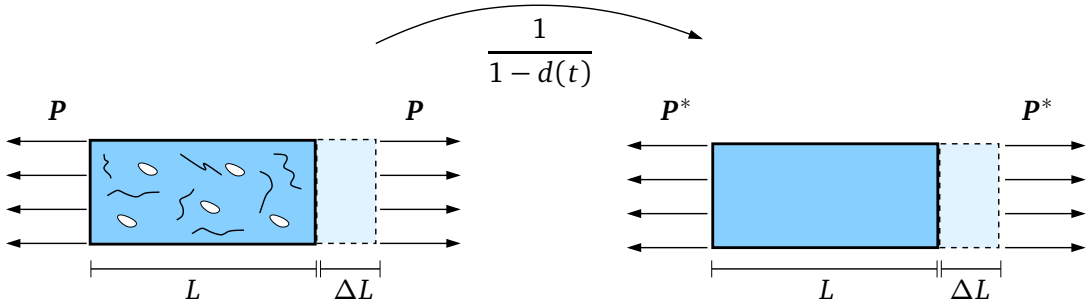

Figure 2.6: Sketch of the strain equivalence hypothesis

Therein, the left-hand side of the illustration corresponds to the physical space which is mapped by the inverse reduction factor onto the effective space displayed on the right-hand side. In this effective space the strain energy functional is defined via

$$U_0^*(\epsilon, \boldsymbol{\kappa}) := [1 - d]^{-1} U_0(\epsilon, d, \boldsymbol{\kappa}), \tag{2.50}$$

whereby $\boldsymbol{\kappa}$ corresponds to the vector of material parameters. Consequently, the effective stress is defined as

$$\sigma^* := \frac{\partial U_0^*}{\partial \epsilon} = \frac{1}{1-d(t)}\,\sigma. \tag{2.51}$$

In a next step the Clausius-Duhem inequality is considered. This inequality corresponds to the second law of thermodynamics and thus is concerned with the irreversibility of processes due to energy dissipation in the system. The local form of the isothermal Clausius-Duhem inequality yields the dissipation as

$$\mathscr{D} = \sigma \frac{\partial \epsilon}{\partial t} - \frac{\partial U_0}{\partial t} \geq 0, \tag{2.52}$$

which by application of the definition of U_0^* results in

$$\mathscr{D} = \left[\sigma - [1-d]\,\frac{\partial U_0^*}{\partial \epsilon}\right] \frac{\partial \epsilon}{\partial t} + U_0^* \frac{\partial d}{\partial t} \geq 0. \tag{2.53}$$

The term in brackets is equivalent to zero due to the definition of the effective stress (2.51) and thus the reduced format of the Clausius-Duhem inequality reads

$$\mathscr{D}^{\text{red}} = U_0^* \frac{\partial d}{\partial t} \geq 0. \tag{2.54}$$

In analogy to the yield function in elasto-plasticity, a damage function ϕ is defined. This damage function is an indicator for the progression of damage. If $\phi = 0$ holds, the damage evolves whereas for $\phi < 0$ no further damage proceeds. Thus, the admissible domain for the effective strain energy is defined in terms of ϕ as

$$\mathscr{A} = \left\{ U_0^* \mid \phi(U_0^*, d, \boldsymbol{\kappa}) = \phi^{\text{dam}}(U_0^*; \boldsymbol{\kappa}) - d \leq 0 \right\}. \tag{2.55}$$

In the work at hand the damage function is defined exponentially via

$$\phi^{\text{dam}} = 1 - \exp(H \left[U_0^i - U_0^0 \right]). \tag{2.56}$$

Therein, H corresponds to a material specific parameter and U_0^0 gives an initial energy threshold for the starting of the damage process, i.e., the damage process initiates if the effective strain energy exceeds the threshold U_0^0. The updated damage threshold U_0^i ensures that the damage parameter d only increases for a further loading, i.e., an increase of U_0^*, and an invariant damage parameter for unloading via

$$U_0^i = \max_{-\infty < \tau < t} \left\{ U_0^*(\tau), U_0^0 \right\}. \tag{2.57}$$

The advancement of the damage can be summarized in the following Kuhn-Tucker equations

$$\frac{\partial U_0^i}{\partial t} \geq 0, \; \phi \leq 0, \; \frac{\partial U_0^i}{\partial t}\phi = 0. \tag{2.58}$$

Thus, damage propagates if $\phi = 0$ and due to (2.55) the damage variable evolutes then according to

$$d = \phi^{\text{dam}}. \tag{2.59}$$

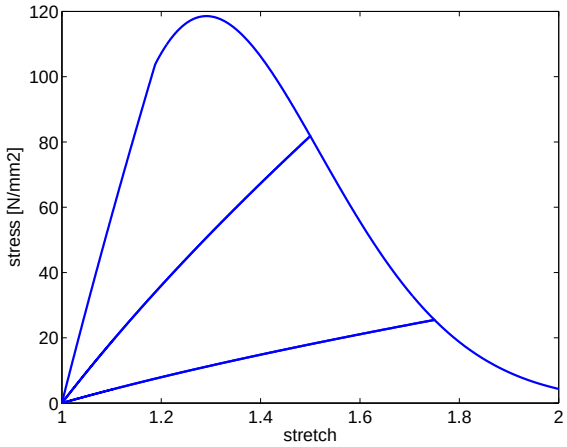

Figure 2.7: Stress-stretch relation for damage coupled to hyperelasticity

The stress-stretch diagram as depicted in Figure 2.7 illustrates the irreversible evolution of damage. The stretch-driven loading and unloading process yields different stress values for the same applied stretch which in Figure 2.7 is observed by the hysteresis-like shape of the stress-stretch curve. Once the damage parameter increased to a certain value a decrease is impossible. For further reading on continuum damage mechanics and more general concepts the reader is referred, e.g., to the work of Chaboche [9] or the textbook by Kachanov [43].

2.4 Variation, Discretization and Linearization of the Governing Equations

In order to solve the governing equations numerically, in the work at hand a finite element scheme is applied. Therefore, firstly the variational or weak formulation is elaborated for the spatial and the material motion problem which is necessary for the principle of virtual work. Then, a discretization in terms of finite elements is carried out. Here, the so-called isoparametric concept is applied, i.e., the same shape functions are applied for the geometry and the deformation map. Furthermore, the Bubnov-Galerkin technique is employed that is based on the same approximations for the unknown deformation map and the virtual displacements. For more details

on the finite element method the reader is referred to the textbooks by Zienkiewicz and Taylor [97], Hughes [40], Belytschko et al. [2] and Wriggers [95] among many other publications in this field.

Finally, a linearization of the discretized (non-linear) weak form is carried out which is required to apply the Newton-Raphson scheme.

2.4.1 Variation, Discretization and Linearization for the Spatial Motion Problem

Firstly, the variational (or weak) form of the spatial motion problem is elaborated. Starting point for this purpose is the quasi-static balance of momentum (2.15) which is multiplied by the spatial virtual displacement (or admissible testfunction) $\mathrm{D}_\delta\boldsymbol{\varphi}$ and integrated over the domain which yields

$$\int_{\mathscr{B}_t} \mathrm{D}_\delta\boldsymbol{\varphi} \cdot \operatorname{div}\boldsymbol{\sigma}\, \mathrm{d}v = -\int_{\mathscr{B}_t} \mathrm{D}_\delta\boldsymbol{\varphi} \cdot \boldsymbol{b}_t\, \mathrm{d}v \quad \forall\ \mathrm{D}_\delta\boldsymbol{\varphi}. \tag{2.60}$$

Thereby, D_δ denotes the variation of a function at fixed material coordinates $\boldsymbol{X}$. Please note, that it is assumed that $\mathrm{D}_\delta\boldsymbol{\varphi}$ fulfills all admissibility conditions and possesses a sufficient smoothness. Integration by parts of the divergence term in (2.60) yields

$$\underbrace{\int_{\partial\mathscr{B}_t} \mathrm{D}_\delta\boldsymbol{\varphi} \cdot \boldsymbol{t}_t\, \mathrm{d}a}_{\mathscr{W}_0^{\mathrm{sur}}} = \underbrace{\int_{\mathscr{B}_t} \nabla_{\boldsymbol{x}}(\mathrm{D}_\delta\boldsymbol{\varphi}) : \boldsymbol{\sigma}\, \mathrm{d}v}_{\mathscr{W}_0^{\mathrm{int}}} - \underbrace{\int_{\mathscr{B}_t} \mathrm{D}_\delta\boldsymbol{\varphi} \cdot \boldsymbol{b}_t\, \mathrm{d}v}_{\mathscr{W}_0^{\mathrm{vol}}} \quad \forall\ \mathrm{D}_\delta\boldsymbol{\varphi}. \tag{2.61}$$

Therein, the first term on the left-hand side represents the variation of work due to surface forces, whereas the terms on the right-hand side correspond to the variation of work due to internal and volume forces, respectively. Thus, the principle of virtual work for the spatial motion problem reads

$$\mathscr{W}_0 = \mathscr{W}_0^{\mathrm{int}} - \mathscr{W}_0^{\mathrm{ext}} = 0 \quad \forall\ \mathrm{D}_\delta\boldsymbol{\varphi}, \tag{2.62}$$

whereby the external contribution includes the volume and the surface forces, i.e.,

$$\mathscr{W}_0^{\mathrm{ext}} = \mathscr{W}_0^{\mathrm{vol}} + \mathscr{W}_0^{\mathrm{sur}}. \tag{2.63}$$

In a next step, this variational formulation requires a discretization in terms of finite elements. To this end the material and the spatial domains are discretized by a finite number n_{el} of elements via

$$\mathscr{B}_0^h = \bigcup_{e=1}^{n_{\mathrm{el}}} \mathscr{B}_0^e \qquad \text{and} \qquad \mathscr{B}_t^h = \bigcup_{e=1}^{n_{\mathrm{el}}} \mathscr{B}_t^e. \tag{2.64}$$

In each of the elements e the geometry is interpolated by means of admissible shape functions N_n with local node numbering $n \in [1, n_{\text{en}}]$, wherein n_{en} defines the number of shape functions or element nodes, respectively. In the following equations $(\bullet)_n$ corresponds to the discrete values of functions at the element nodes within the numerical scheme. Thus, it holds

$$\boldsymbol{X}^h = \sum_{n=1}^{n_{\text{en}}} N_n \boldsymbol{X}_n \qquad \text{and} \qquad \boldsymbol{x}^h = \sum_{n=1}^{n_{\text{en}}} N_n \boldsymbol{x}_n \tag{2.65}$$

Consequently, the related deformation gradients read

$$\nabla_{\boldsymbol{X}} \boldsymbol{x}^h = \sum_{n=1}^{n_{\text{en}}} \boldsymbol{x}_n \otimes \nabla_{\boldsymbol{X}} N_n \qquad \text{and} \qquad \nabla_{\boldsymbol{x}} \boldsymbol{X}^h = \sum_{n=1}^{n_{\text{en}}} \boldsymbol{X}_n \otimes \nabla_{\boldsymbol{x}} N_n. \tag{2.66}$$

Within the applied Bubnov-Galerkin scheme, the virtual displacements are approximated by the same shape functions as the geometry and therefore render the representations

$$\mathrm{D}_\delta \boldsymbol{\varphi}^h = \sum_{n=1}^{n_{\text{en}}} N_n \, \mathrm{D}_\delta \boldsymbol{\varphi}_n \qquad \text{and} \qquad \mathrm{d}_\delta \boldsymbol{\Phi}^h = \sum_{n=1}^{n_{\text{en}}} N_n \, \mathrm{d}_\delta \boldsymbol{\Phi}_n. \tag{2.67}$$

Thus, the corresponding gradients result in

$$\nabla_{\boldsymbol{x}} \, \mathrm{D}_\delta \boldsymbol{\varphi}^h = \sum_{n=1}^{n_{\text{en}}} \mathrm{D}_\delta \boldsymbol{\varphi}_n \otimes \nabla_{\boldsymbol{x}} N_n \qquad \text{and} \qquad \nabla_{\boldsymbol{X}} \, \mathrm{d}_\delta \boldsymbol{\Phi}^h = \sum_{n=1}^{n_{\text{en}}} \mathrm{d}_\delta \boldsymbol{\Phi}_n \otimes \nabla_{\boldsymbol{X}} N_n. \tag{2.68}$$

By assistance of these interpolations the discretized variational formulation is derived as

$$\mathscr{W}_0^h = \mathop{\mathsf{A}}_{e=1}^{n_{\text{el}}} \mathrm{D}_\delta \boldsymbol{\varphi}_n \cdot \left[\int_{\mathscr{B}_t^e} \nabla_{\boldsymbol{x}} N_n \cdot \boldsymbol{\sigma} \, \mathrm{d}v - \int_{\mathscr{B}_t^e} N_n \, \boldsymbol{b}_t \, \mathrm{d}v - \int_{\partial \mathscr{B}_t^e} N_n \, \boldsymbol{t}_t \, \mathrm{d}a \right] = 0 \quad \forall \; \mathrm{D}_\delta \boldsymbol{\varphi}_n. \tag{2.69}$$

Therein, $\mathop{\mathsf{A}}_{e=1}^{n_{\text{el}}}$ denotes the assembly of all n_{en} element node contributions to global node values $I = 1, \ldots, n_{\text{np}}$. In a compact format $\mathscr{W}_0^h$ reads

$$\mathscr{W}_0^h = \mathop{\mathsf{A}}_{e=1}^{n_{\text{el}}} \mathrm{D}_\delta \boldsymbol{\varphi}_n \cdot \left[\boldsymbol{f}_n^{\text{int}} - \boldsymbol{f}_n^{\text{ext}} \right] = 0 \quad \forall \; \mathrm{D}_\delta \boldsymbol{\varphi}_n. \tag{2.70}$$

Due to the arbitrariness of the virtual displacements the discrete equilibrium condition follows as

$$\boldsymbol{r}_I = \boldsymbol{f}_I^{\text{int}} - \boldsymbol{f}_I^{\text{ext}} = \boldsymbol{0} \quad \forall \; I = 1, \ldots, n_{\text{np}}, \tag{2.71}$$

wherein the internal force vector is given by

$$\boldsymbol{f}_I^{\text{int}} = \mathop{\mathsf{A}}_{e=1}^{n_{\text{el}}} \int_{\mathscr{B}_t^e} \nabla_{\boldsymbol{x}} N_n \cdot \boldsymbol{\sigma} \, \mathrm{d}v, \tag{2.72}$$

and the external force vector by

$$\boldsymbol{f}_I^{\text{ext}} = \mathop{\mathsf{A}}_{e=1}^{n_{\text{el}}} \int_{\partial \mathscr{B}_t^e} N_n \, \boldsymbol{t}_t \, \mathrm{d}a + \mathop{\mathsf{A}}_{e=1}^{n_{\text{el}}} \int_{\mathscr{B}_t^e} N_n \, \boldsymbol{b}_t \, \mathrm{d}v. \tag{2.73}$$

Finally, in order to solve the system of equations as given in (2.71) numerically, a linearization procedure is required. This linearization is necessary due to the fact that the variational formulation yields in case of a finite deformation approach a non-linear system of equations which requires an iterative solution scheme, as e.g., the Newton-Raphson method. In this scheme the variational form is expanded into a Taylor series with break after the linear part, i.e.,

$$\boldsymbol{r}_I^{k+1} = \boldsymbol{r}_I^k + \Delta \boldsymbol{r}_I = \boldsymbol{0} \quad \forall \, I = 1, ..., n_{\text{np}}. \tag{2.74}$$

One of the advantages of the Newton-Raphson scheme is given by its quadratic convergence close to the solution. In order to apply the linearization to the discretized variational form the directional derivative of a function $\boldsymbol{r}$ at the position $\boldsymbol{x}$ in direction $\Delta \boldsymbol{x}$ is established as

$$\Delta \boldsymbol{r}(\boldsymbol{x}) = \mathrm{D}_{\Delta \boldsymbol{x}} \boldsymbol{r}(\boldsymbol{x}) \cdot \Delta \boldsymbol{x} := \frac{\mathrm{d}}{\mathrm{d}\epsilon} \left[\boldsymbol{r}(\boldsymbol{x} + \epsilon \, \Delta \boldsymbol{x}) \right] \Big|_{\epsilon=0}. \tag{2.75}$$

Thus, the linearization of the residuum $\boldsymbol{r}_I$ as given in (2.71) reads

$$\Delta \boldsymbol{r}_I(\boldsymbol{x}_J) = \sum_{J=1}^{N_{\text{np}}} \mathrm{D}_{\Delta \boldsymbol{x}_J} \boldsymbol{r}_I(\boldsymbol{x}_J) = \sum_{J=1}^{N_{\text{np}}} \frac{\partial \boldsymbol{r}_I(\boldsymbol{x}_J)}{\partial \boldsymbol{x}_J} \cdot \Delta \boldsymbol{x}_J. \tag{2.76}$$

Therein, the derivative yields the stiffness matrix, i.e.,

$$\boldsymbol{K}_{IJ} = \frac{\partial \boldsymbol{r}_I(\boldsymbol{x}_J)}{\partial \boldsymbol{x}_J} \quad \forall \, I, J = 1, ..., n_{\text{np}}, \tag{2.77}$$

and therefore, the resulting system of equations to compute the update of the spatial positions reads

$$\Delta \boldsymbol{x}_J = - \sum_{I=1}^{N_{\text{np}}} \boldsymbol{K}_{JI}^{-1} \cdot \boldsymbol{r}_I^k \quad \forall \, J = 1, ..., n_{\text{np}}. \tag{2.78}$$

Due to the linearization of the residuum, the stiffness matrix consists of a sum of

two contributions. The geometrical part reads

$$\boldsymbol{K}_{IJ}^{\text{geo}} = \operatorname*{A}_{e=1}^{n_{\text{el}}} \int_{\mathscr{B}_t^e} (\nabla_{\boldsymbol{x}} N_n)^t \cdot \boldsymbol{\sigma} \cdot \nabla_{\boldsymbol{x}} N_m \, \boldsymbol{I} \, \mathrm{d}v, \tag{2.79}$$

whereas the material part is calculated via

$$\boldsymbol{K}_{IJ}^{\text{mat}} = \operatorname*{A}_{e=1}^{n_{\text{el}}} \int_{\mathscr{B}_t^e} (\nabla_{\boldsymbol{x}} N_n)^t \cdot \mathbb{e} \cdot \nabla_{\boldsymbol{x}} N_m \, \mathrm{d}v. \tag{2.80}$$

Therein, $\mathbb{e}$ corresponds to the fourth-order Eulerian tangent modulus. The exact format of $\mathbb{e}$ depends on the constitutive equation. A comprehensive overview of tangent moduli for the spatial and for the material motion problem as well as approaches based on alternative stress measures is given in the work of Kuhl et al. [53].

2.4.2 Variation and Discretization for the Material Motion Problem

Below, the variational (or weak) form of the material motion problem is derived. To this end, the material quasi-static balance of momentum (2.23) is multiplied by the material virtual displacement (or admissible testfunction) $\mathrm{d}_\delta \boldsymbol{\Phi}$ and integrated over the domain which results in

$$\int_{\mathscr{B}_0} \mathrm{d}_\delta \boldsymbol{\Phi} \cdot \mathrm{Div} \boldsymbol{\Sigma} \, \mathrm{d}V = - \int_{\mathscr{B}_0} \mathrm{d}_\delta \boldsymbol{\Phi} \cdot \boldsymbol{B}_0 \, \mathrm{d}V \quad \forall \; \mathrm{d}_\delta \boldsymbol{\Phi}. \tag{2.81}$$

Therein, d_δ denotes the variation of a function at fixed spatial coordinates $\boldsymbol{x}$. The admissibility and a sufficient smoothness of $\mathrm{d}_\delta \boldsymbol{\Phi}$ is postulated. An integration by parts of the divergence term yields

$$\underbrace{\int_{\partial \mathscr{B}_0} \mathrm{d}_\delta \boldsymbol{\Phi} \cdot \boldsymbol{T}_0 \, \mathrm{d}A}_{\mathscr{W}_t^{\text{sur}}} = \underbrace{\int_{\mathscr{B}_0} \nabla_{\boldsymbol{X}} (\mathrm{d}_\delta \boldsymbol{\Phi}) : \boldsymbol{\Sigma} \, \mathrm{d}V}_{\mathscr{W}_t^{\text{int}}} - \underbrace{\int_{\mathscr{B}_0} \mathrm{d}_\delta \boldsymbol{\Phi} \cdot \boldsymbol{B}_0 \, \mathrm{d}V}_{\mathscr{W}_t^{\text{vol}}} \quad \forall \; \mathrm{d}_\delta \boldsymbol{\Phi}. \tag{2.82}$$

Therein, the first term on the left-hand side corresponds to the variation of work due to the forces at the surface, whereas the terms on the right-hand side represent the contributions of the internal and the volume forces, respectively. Please note, that to simplify matters it is assumed that the considered continuum contains no interface or other discontinuities. In case of such a continuum, interface terms depending on the jump of the tractions $\boldsymbol{T}_0$ across the interface need to be incorporated, additionally.

To sum up, the principle of virtual work for the material motion problem is given by

$$\mathscr{W}_t = \mathscr{W}_t^{\text{int}} - \mathscr{W}_t^{\text{ext}} = \mathbf{0} \quad \forall \ \mathrm{d}_\delta \boldsymbol{\Phi}, \tag{2.83}$$

whereby the virtual work due to external forces includes the virtual work due to volume and surface forces, i.e.,

$$\mathscr{W}_t^{\text{ext}} = \mathscr{W}_t^{\text{vol}} + \mathscr{W}_t^{\text{sur}}. \tag{2.84}$$

In a next step, the discretization of the variational formulation is carried out in the spirit of equations (2.72) – (2.68). The discretized variational form then reads

$$\mathscr{W}_t^h = \mathop{\mathsf{A}}_{e=1}^{n_{\text{el}}} \mathrm{d}_\delta \boldsymbol{\Phi} \cdot \left[\int_{\mathscr{B}_0^e} \nabla_{\boldsymbol{X}} N_n \cdot \boldsymbol{\Sigma} \, \mathrm{d}V - \int_{\mathscr{B}_0^e} N_n \boldsymbol{B}_0 \, \mathrm{d}V - \int_{\partial \mathscr{B}_0^e} N_n \boldsymbol{T}_0 \, \mathrm{d}A \right] = 0 \quad \forall \ \mathrm{d}_\delta \boldsymbol{\Phi}. \tag{2.85}$$

In terms of material forces the discretized variational form takes the more compact format

$$\mathscr{W}_t^h = \mathop{\mathsf{A}}_{e=1}^{n_{\text{el}}} \mathrm{d}_\delta \boldsymbol{\Phi} \cdot \left[\boldsymbol{F}_n^{\text{int}} - \boldsymbol{F}_n^{\text{ext}} \right] = 0 \quad \forall \ \mathrm{d}_\delta \boldsymbol{\Phi}. \tag{2.86}$$

The arbitrariness of the virtual displacements results in the following discrete equilibrium condition in terms of the nodal residuum

$$\boldsymbol{R}_I = \boldsymbol{F}_I^{\text{int}} - \boldsymbol{F}_I^{\text{ext}} = \mathbf{0} \quad \forall \ I = 1, ..., n_{\text{np}}, \tag{2.87}$$

wherein the internal vector is given by

$$\boldsymbol{F}_I^{\text{int}} = \mathop{\mathsf{A}}_{e=1}^{n_{\text{el}}} \int_{\mathscr{B}_0^e} \nabla_{\boldsymbol{X}} N_n \cdot \boldsymbol{\Sigma} \, \mathrm{d}V, \tag{2.88}$$

and the external force vector by

$$\boldsymbol{F}_I^{\text{ext}} = \mathop{\mathsf{A}}_{e=1}^{n_{\text{el}}} \int_{\partial \mathscr{B}_0^e} N_n \boldsymbol{T}_0 \, \mathrm{d}A + \mathop{\mathsf{A}}_{e=1}^{n_{\text{el}}} \int_{\mathscr{B}_t^e} N_n \boldsymbol{B}_0 \, \mathrm{d}V. \tag{2.89}$$

In the context of these considerations the material node point force vector is defined as

$$\mathfrak{F} = \mathop{\mathsf{A}}_{e=1}^{n_{\text{el}}} \int_{\mathscr{B}_0^e} \left[\nabla_{\boldsymbol{X}} N_n \cdot \boldsymbol{\Sigma} - N_n \boldsymbol{B}_0 \right] \mathrm{d}V. \tag{2.90}$$

This material node point vector can be applied to establish criteria whether a prescribed crack in a continuum propagates due to the equivalence between the material force at a crack tip and the J-integral.

Due to the fact that in the work at hand the material balance of momentum does

not induce an independent equilibrium condition which need to be solved, the linearization procedure is not elaborated here. Instead of solving the material motion problem only the desired material node point forces are determined by means of equation (2.90).

Further details on the theoretical setting of the material motion problem are given in the work of Steinmann [82] and the corresponding computational setting is elaborated by Steinmann et al. in [83].

3 Computational Homogenization of Spatial Quantities

In this section the homogenization of quantities in the context of the spatial motion problem at finite deformation is elaborated within a computational homogenization framework. In contrast to the standard computational homogenization scheme, which can be found e.g. in the work of Suquet [90], Kouznetsova et al. [50], Miehe [59] and Miehe et al. [57], formulations for interfaces and volume forces on the micro-level are incorporated. In order to simplify the notation, it is mentioned that all quantities in this section belong to the spatial motion problem if no further specifications are given. Exceptions to this will be stated explicitly. Furthermore, the following conventions are made throughout the whole work: microscopic vectors and tensors are denoted by bold lower and uppercase letters ($\boldsymbol{b}_0, \boldsymbol{F}, \boldsymbol{P}$, etc.), homogenized quantities are indicated by a bar ($\bar{\bullet}$) and macroscopic quantities by the index $(\bullet)_M$. In order to keep the notation as simply as possible, no further distinction between vectors and tensors will be made in the description. In case that the order of tensors is not accessible from the context, index notation will be used.

Overview on Homogenization Techniques

The most basic approach to determine effective overall properties of microstructured materials is given by the rule of mixture, i.e., the required overall properties are determined by averaging the properties of the microscopic constituents weighted by their volume ratio. This method only yields a rough estimate of the macroscopic properties due to the fact that the microscopic setting is not taken into account. Furthermore, different possible material behaviors like, e.g., an elastic fiber embedded into a plastic matrix material cannot be regarded and effects like a macroscopic anisotropy due to microscopic fiber-reinforcements are not involved. Therefore, more sophisticated homogenization approaches have been developed. A method to determine upper and lower bounds for the macroscopic moduli has been proposed by Voigt in [93] and Reuss in [69]. An extension of these concepts on the estimation of bounds for overall properties based on a variational formulation is given in the work of Hashin and Shtrikman, see, e.g., [32, 33, 34].

On the other hand, an analytical approach is given by the so-called self-consistent scheme, which is based on the analytical solution for the determination of overall properties for spherical or elliptical inclusions in an infinite matrix established by Eshelby [15]. This self-consistent scheme yields proper results for structures with a geometrical regularity, but it fails for structures with a complex microscopic setting

or in cases of big stiffness ratios between the inclusion and the matrix material. An application of this method to polycrystalline materials can be found in the publication by Kröner [52]. For more details on the self-consistent methods the reader is referred, e.g., to the publications by Hashin [30, 31], Hill [36] and Willis [94] and references therein. Within the context of analytical methods, a further approach is given by the mean-field approximation, or also called Mori-Tanaka method, see, e.g., the work of Tanaka and Mori [91], Mori and Tanaka [61] and Benveniste [4].

A mathematical approach is given by the asymptotic homogenization, see, e.g., the textbook by Bensoussan [3], or the publications of Sanchez-Palenzia [75], Suquet [90], Devries et al. [13], Guedes and Kikuchi [28] and Fish et al. [20]. Within this scheme an asymptotic expansion of displacement and stress fields from the characteristic length scale of a microscopic heterogeneity towards the required macro-variables is performed by means of a variational principle. Therefore, this method provides effective overall properties as well as local stresses and strains. But in most of the cases, the asymptotic homogenization scheme is only applicable to simple geometries at small strains.

Accompanied with more powerful CPUs, methods based on direct micro-macro transitions, the so-called computational homogenization schemes have been developed, see the work of Suquet [90]. In these approaches the micro-structure is captured within a so-called representative volume element (RVE) which has been primarily introduced by Hill in [35] within the context of unit-cell methods. In the direct micro-macro approaches these RVEs are attached to each macroscopic simulation point. With assistance of admissible boundary conditions, a microscopic boundary value problem is generated and solved by appropriate numerical methods. In a next step, the required variables are averaged and thus a macroscopic stress-strain relation in established in each single simulation point. Thus, no constitutive overall assumptions are required at the macro-level, but locally in each simulation point a micromechanically based stress or strain response and the corresponding tangent modulus is calculated. Furthermore, it is possible in order to perform the computation more efficiently to carry out the full micro-macro transition only in regions of interest and assume the constitutive tangents constant in other parts, see Ghosh et al. [26] for details. A further advantage of the computational homogenization is the applicability of large deformations on both scales and the admissibility of any kind of material behavior at the micro-scale like non-linear, inelastic or rate-dependent material laws. At the micro-level various modeling techniques can be applied, e.g., the finite element method, lattice statics or molecular dynamics. In the publications of Feyel [16] and Feyel and Chaboche [18] a classical continuum is coupled to a periodic RVE, and both scales are simulated by means of the finite element method which yields to the denominations of this scheme as FE^2. Miehe [58] contributed an incremental variational formulation for the coupling of a micro-structure consisting of inelastic constituents and a classical macro-continuum at small strains. Numerical algorithms and matrix representations for the micro-macro transition based on the minimization of the averaged incremental energy were developed by Miehe and

Koch in [56]. The extension of the incremental variational formulation to large strains has been elaborated by Miehe et al. in [59], whereas the algorithms and the matrix formulations at large strains are given in Miehe [57], completed by illustrative examples for finite elasto-plastic deformation of composites, texture developments in polycrystalline materials and equilibrium states of particles assemblies. An application of the multi-scale computation to a nonlocal damage model for brittle composite materials based on a three-scale algorithm, wherein the damage evolves at the smallest scale, has been developed by Fish and Yu in [19]. The homogenization concept is implemented for the inelastic material behavior in the work of Stolz [85] for the plastic behavior of polycrystals at finite strains. A comprehensive overview on homogenized variables and averaging theorems in finite plasticity can be found in the work of Nemat-Nasser [66]. Further enhancements of the standard computational homogenization scheme can be found in the work of Hirschberger et al. [38] wherein a homogenization scheme for cohesive interfaces is developed or in the publication of Feyel [17] where generalized continua are considered. In the work of Ricker et al. [72, 73] different approaches towards the homogenization of material quantities like the Eshelby stress and configurational forces are discussed. To this end also see Chapter 4.

More computational homogenization approaches based on Voronoï cell methods can be found in the work of Ghosh et al. [24, 25], whereas methods based on fast Fourier transformations are elaborated in the publications by Fotiu and Nemat-Nasser [21], Moulinec and Suquet [62] and Miehe et al. [60]. Additionally to the homogenization schemes mentioned above, which belong to the class of first order homogenization schemes, also second order homogenization schemes have been developed, see, e.g., the work of Kouznetsova [48] and Kouznetsova et al. [51]. In the second order schemes the gradient of the deformation gradient is incorporated into the boundary conditions. Therefore, in contrast to the first order schemes the size of the microscopic volume element is taken into account and thus also geometrical size effects are regarded. Furthermore, high gradients in the stress-strain relation in critical regions can be captured properly.

Among many other publications in this field, more details on direct micro-macro transitions can be found in the work of Smit et al. [81], Schröder [77], Terada and Kikuchi [92] and Jänike et al. [41]. Comprehensive overviews on homogenization techniques are given, e.g., in the textbook by Nemat-Nasser and Hori [67] or the book by Gross and Seelig [27], or the work of Kanouté [44] and Geers et al. [23].

Scale-Separation

In the work at hand, a first order computational homogenization scheme is applied. Therefore, the separation of scales has to be enforced, i.e., the characteristic length l of the attached RVE in each macroscopic simulation point has to be much smaller than the characteristic length L of the macroscopic specimen, that is

$$l \ll L. \tag{3.1}$$

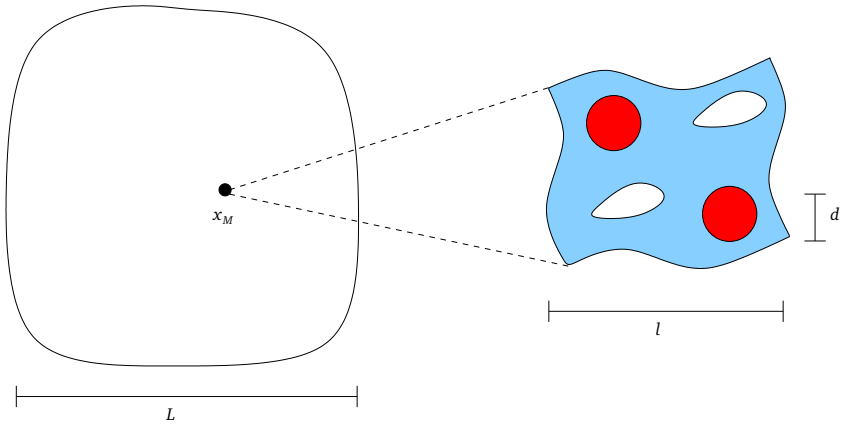

Figure 3.1: Characteristic length scales of macro- and micro-scale, and microscopic heterogeneities

The characteristic length scales are depicted in Figure 3.1. Thereby, the choice of the appropriate size of the RVE is rather delicate task. On the one hand the RVE has to be large enough to give a representative image of the underlying microscopic morphology, i.e., the accumulation and the arrangement of the microscopic heterogeneities need to be captured which yields the connection between the characteristic length d of the heterogeneities and the micro-scale

$$d \ll l. \tag{3.2}$$

On the other hand the RVE should be as small as possible to guarantee effective numerical simulations. The present work focuses only on the algorithmic treatment of the homogenization scheme, not on the choice of the RVE. Thus, this precarious topic is not concerned in detail.

3.1 Averaged Spatial Variables

Firstly, the required variables for the spatial motion problem are defined as averages depending on the microscopic quantities.

These homogenized variables are not simply defined as the volume average of their microscopic analogs, but as averages over boundary terms of the RVE, see Figure 3.2 for the setting. This modus operandi has already been proposed by Hill [37], pp.137–138:

> Macro-variables intended for constitutive laws should thus be capable of definition in terms of surface data alone, either directly, or indirectly. It is not necessary, by any means, that macro-variables so defined should be unweighted volume averages of their microscopic counterparts. Accordingly, we approach the construction of macro-variables by first identifying some relevant averages that depend uniquely on surface data.

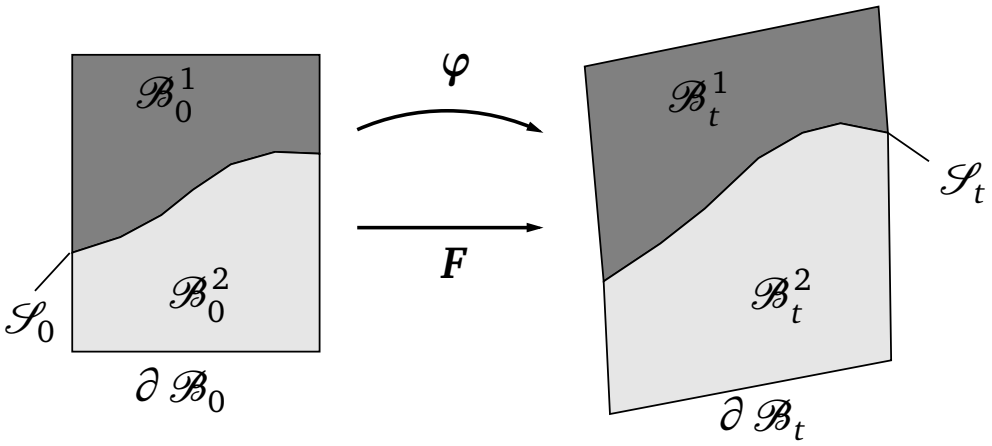

Figure 3.2: Microscopic spatial motion problem

Thus, the averaged deformation gradient tensor is given by

$$\bar{\boldsymbol{F}} := \frac{1}{V_0} \int\limits_{\partial\,\mathscr{B}_0} \boldsymbol{\varphi} \otimes \boldsymbol{N}\, \mathrm{d}A = \frac{1}{V_0} \int\limits_{\mathscr{B}_0} \boldsymbol{F}\, \mathrm{d}V, \tag{3.3}$$

wherein V_0 corresponds to the volume of the RVE in the material configuration. Please note, that if the RVE additionally contains holes or cracks, i.e., $\boldsymbol{\varphi}$ is not continuous, integrals over the boundary $\partial\,\mathscr{H}_0$ of the hole or the crack need to be incorporated, i.e., it holds

$$\bar{\boldsymbol{F}} := \frac{1}{V_0} \int\limits_{\partial\,\mathscr{B}_0} \boldsymbol{\varphi} \otimes \boldsymbol{N}\, \mathrm{d}A = \frac{1}{V_0} \int\limits_{\mathscr{B}_0 \setminus \mathscr{H}_0} \boldsymbol{F}\, \mathrm{d}V - \frac{1}{V_0} \int\limits_{\partial\,\mathscr{H}_0} \boldsymbol{\varphi} \otimes \boldsymbol{N}\, \mathrm{d}A, \tag{3.4}$$

see, e.g., the work of Miehe et al. [59] for more details on such RVEs.

The averaged Cauchy stress, which provides a stress measure in spatial description, and thus needs to be weighted by the actual RVE volume V_t, is defined in terms of the dyadic product of the Cauchy tractions and the spatial position vector as

$$\bar{\boldsymbol{\sigma}} := \frac{1}{V_t} \int\limits_{\partial\,\mathscr{B}_t} \boldsymbol{t}_t \otimes \boldsymbol{\varphi}\, \mathrm{d}a. \tag{3.5}$$

This boundary integral can be transformed into a volume integral via the definition of t_t and application of the Gauß theorem

$$\begin{aligned} \bar{\boldsymbol{\sigma}} &= \frac{1}{V_t} \int\limits_{\partial\,\mathscr{B}_t} \boldsymbol{t}_t \otimes \boldsymbol{\varphi}\, \mathrm{d}a &&= \frac{1}{V_t} \int\limits_{\partial\,\mathscr{B}_t} \left(\left[\boldsymbol{\varphi} \otimes \boldsymbol{\sigma} \right] \cdot \boldsymbol{n} \right)^t \mathrm{d}a \\ &= \frac{1}{V_t} \int\limits_{\mathscr{B}_t} \left(\operatorname{div} \left(\boldsymbol{\varphi} \otimes \boldsymbol{\sigma} \right) \right)^t \mathrm{d}v &&= \frac{1}{V_t} \int\limits_{\mathscr{B}_t} \left[\boldsymbol{\sigma} - \boldsymbol{b}_t \otimes \boldsymbol{\varphi} \right] \mathrm{d}v. \end{aligned} \tag{3.6}$$

Thereby, in the last relation the equivalences div $\boldsymbol{\sigma} = -\boldsymbol{b}_t$ and $\nabla_{\boldsymbol{x}} \boldsymbol{\varphi} = \boldsymbol{I}$ are exploited.

Finally, the averaged Piola stress is given in terms of the material boundary via

$$\bar{\boldsymbol{P}} := \frac{1}{V_0} \int_{\partial \mathscr{B}_0} \boldsymbol{t}_0 \otimes \boldsymbol{X} \, \mathrm{d}A = \frac{1}{V_0} \int_{\mathscr{B}_0} \left[\boldsymbol{P} - \boldsymbol{b}_0 \otimes \boldsymbol{X} \right] \mathrm{d}V. \tag{3.7}$$

A more comprehensive overview on averaged quantities can be found in the textbooks by Mura [65] and Nemat-Nasser and Hori [67].

3.2 Spatial Scale-Transition

In order to connect the macroscopic setting with the underlying RVEs a downscaling has to be performed. Here, two different approaches are presented: on the one hand a deformation-driven approach based on the macroscopic deformation gradient tensor $\boldsymbol{F}_M$ and on the other hand a stress-driven approach based on the macroscopic Piola stress $\boldsymbol{P}_M$. With assistance of this downscaling appropriate boundary conditions are applied to the RVE and once the microscopic boundary value problem is solved, the micro-to-macro-transition is performed according to Section 3.1.

3.2.1 Deformation-Based Approach

In the deformation-driven downscaling approach the microscopic deformation map is given in terms of a constant macroscopic term $\boldsymbol{\varphi}_M$, the macroscopic deformation gradient $\boldsymbol{F}_M$ and spatial fluctuations $\boldsymbol{w}$ as

$$\boldsymbol{\varphi}(\boldsymbol{X}) = \boldsymbol{\varphi}_M + \boldsymbol{F}_M \cdot \boldsymbol{X} + \boldsymbol{w}(\boldsymbol{X}). \tag{3.8}$$

The gradient of this deformation map yields the microscopic deformation gradient as

$$\boldsymbol{F} = \boldsymbol{F}_M + \nabla_{\boldsymbol{X}} \boldsymbol{w}. \tag{3.9}$$

Within the applied deformation-based scheme the scale-transition should be consistent in the deformation gradient, i.e., the average strain theorem which claims the equivalence of the averaged deformation gradient and the macroscopic deformation gradient should be valid, that is

$$\bar{\boldsymbol{F}} \equiv \boldsymbol{F}_M. \tag{3.10}$$

Insertion of the definition of the averaged deformation gradient (3.3) and the microscopic deformation gradient (3.9) into the average strain theorem yields the fol-

lowing constraint on the fluctuations at the boundary

$$\int_{\mathscr{B}_0} \nabla_{\boldsymbol{X}} \boldsymbol{w} \, \mathrm{d}V = \int_{\partial \mathscr{B}_0} \boldsymbol{w} \otimes \boldsymbol{N} \, \mathrm{d}A \equiv \boldsymbol{0}. \tag{3.11}$$

Therefore, the following two types of boundary conditions emerge. Apparently linear displacement boundary conditions which are characterized through vanishing fluctuations, i.e., it holds

$$\boldsymbol{w} = \boldsymbol{0}, \tag{3.12}$$

fulfill equation (3.11). Furthermore, the boundary of the RVE can be split up into a positive and a negative part and then equation (3.11) is satisfied by periodic fluctuations on the boundary

$$\boldsymbol{w}^+ = \boldsymbol{w}^- \quad \text{with} \quad \partial \mathscr{B}_0 = \partial \mathscr{B}_0^+ \cup \partial \mathscr{B}_0^-. \tag{3.13}$$

The periodic boundary conditions and the localized force balance across the boundary imply that in case of a geometrically periodic RVE the tractions behave anti-periodically, that is

$$\boldsymbol{t}_0^+ + \boldsymbol{t}_0^- = \boldsymbol{0} \quad \text{on} \quad \partial \mathscr{B}_0 = \partial \mathscr{B}_0^+ \cup \partial \mathscr{B}_0^-. \tag{3.14}$$

Considering the periodic boundary conditions as given in equation (3.13), focus is put on the micro-to-macro transition in terms of the averaged virtual work, which is considered here by means of potentials. The Hill-Mandel condition –see, e.g., the work of Hill [35] or Suquet [89]– requires the equivalence of the macroscopic virtual (deformational) work and the average of the microscopic virtual (deformational) work.

$$\mathscr{P}_{tM} = j_M \, \mathrm{D}_\delta \, U_{0M} \equiv \bar{j} \, \mathrm{D}_\delta \, \bar{U}_0 = \bar{\mathscr{P}}_t, \tag{3.15}$$

or more explicitly

$$\left[\mathrm{D}_\delta \, \boldsymbol{F}_M \cdot \boldsymbol{F}_M^{-1} \right] : \boldsymbol{\sigma}_M - \mathrm{D}_\delta \, \boldsymbol{\varphi}_M \cdot \boldsymbol{b}_{tM} \equiv \frac{1}{V_t} \int_{\partial \mathscr{B}_t} \mathrm{D}_\delta \, \boldsymbol{\varphi} \cdot \boldsymbol{t}_t \, \mathrm{d}a. \tag{3.16}$$

Thereby, the variation of the deformation map at fixed coordinates $\boldsymbol{X}$ is given by

$$\mathrm{D}_\delta \, \boldsymbol{\varphi} = \mathrm{D}_\delta \, \boldsymbol{\varphi}_M + \mathrm{D}_\delta \, \boldsymbol{F}_M \cdot \boldsymbol{X} + \mathrm{D}_\delta \, \boldsymbol{w}. \tag{3.17}$$

Application of this variation of the microscopic deformation map to the Hill-Mandel condition (3.16) yields for the right-hand side

$$\frac{1}{V_t} \left[\int_{\partial \mathscr{B}_t} \mathrm{D}_\delta \boldsymbol{\varphi}_M \cdot \boldsymbol{t}_t \, \mathrm{d}a + \int_{\partial \mathscr{B}_t} \left[\mathrm{D}_\delta \boldsymbol{F}_M \cdot \boldsymbol{X} \right] \cdot \boldsymbol{t}_t \, \mathrm{d}a + \int_{\partial \mathscr{B}_t} \mathrm{D}_\delta \boldsymbol{w} \cdot \boldsymbol{t}_t \, \mathrm{d}a \right]. \tag{3.18}$$

Herein, the last integral vanishes for periodic boundary conditions due to

$$\mathrm{D}_\delta \boldsymbol{w}^+ = \mathrm{D}_\delta \boldsymbol{w}^- \quad \text{and} \quad \boldsymbol{t}_t^+ = -\boldsymbol{t}_t^- \quad \text{on} \quad \partial \mathscr{B}_t = \partial \mathscr{B}_t^+ \cup \partial \mathscr{B}_t^-. \tag{3.19}$$

Furthermore, $\mathrm{D}_\delta \boldsymbol{\varphi}_M$ and $\mathrm{D}_\delta \boldsymbol{F}_M$ are constant for each single RVE and thus they can be extracted from the integrals, i.e., (3.18) reads

$$\frac{1}{V_t} \left[\mathrm{D}_\delta \boldsymbol{\varphi}_M \cdot \int_{\partial \mathscr{B}_t} \boldsymbol{t}_t \, \mathrm{d}a + \mathrm{D}_\delta \boldsymbol{F}_M : \int_{\partial \mathscr{B}_t} \boldsymbol{t}_t \otimes \boldsymbol{X} \, \mathrm{d}a \right]. \tag{3.20}$$

For a geometrically periodic RVE it follows from (3.14)

$$\int_{\partial \mathscr{B}_t} \boldsymbol{t}_t \, \mathrm{d}a = \int_{\partial \mathscr{B}_t^+} \boldsymbol{t}_t^+ \, \mathrm{d}a + \int_{\partial \mathscr{B}_t^-} \boldsymbol{t}_t^- \, \mathrm{d}a = \int_{\partial \mathscr{B}_t^+} \left[\boldsymbol{t}_t^+ + \boldsymbol{t}_t^- \right] \mathrm{d}a = \boldsymbol{0}, \tag{3.21}$$

for periodic boundary conditions. On the other hand, due to the integrated force balance, this implies that only self-equilibrated volume forces $\boldsymbol{b}_t$ are allowed at the micro-level if antiperiodic tractions are requested, which in turn is a natural consequence of assuming geometrical periodicity of the RVE. Thus it holds

$$\int_{\partial \mathscr{B}_t} \boldsymbol{t}_t \, \mathrm{d}a = -\int_{\mathscr{B}_t} \boldsymbol{b}_t \, \mathrm{d}v = \boldsymbol{0}. \tag{3.22}$$

Furthermore, if condition (3.22) should be valid for arbitrary geometrically periodic domains $\mathscr{B}_t$ the microscopic body forces need to vanish, i.e., it holds

$$\boldsymbol{b}_t = \boldsymbol{0} \quad \Rightarrow \quad \boldsymbol{b}_0 = J \, \boldsymbol{b}_t = \boldsymbol{0}. \tag{3.23}$$

Therefore, the first integral on the right-hand side of equation (3.20) vanishes and the Hill-Mandel condition reads

$$\left[\mathrm{D}_\delta \boldsymbol{F}_M \cdot \boldsymbol{F}_M^{-1} \right] : \boldsymbol{\sigma}_M - \mathrm{D}_\delta \boldsymbol{\varphi}_M \cdot \boldsymbol{b}_{tM} = \mathrm{D}_\delta \boldsymbol{F}_M : \frac{1}{V_t} \int_{\partial \mathscr{B}_t} \boldsymbol{t}_t \otimes \boldsymbol{X} \, \mathrm{d}a. \tag{3.24}$$

In this equation the material coordinates $\boldsymbol{X}$ are substituted by means of the spatial scale-transition (3.8), that is

$$\boldsymbol{X} = \boldsymbol{F}_M^{-1} \cdot \left[\boldsymbol{\varphi} - \boldsymbol{\varphi}_M - \boldsymbol{w} \right], \tag{3.25}$$

which yields

$$\mathrm{D}_\delta \boldsymbol{F}_M : \frac{1}{V_t}\left[\int\limits_{\partial\mathscr{B}_t} \boldsymbol{t}_t \otimes \left[\boldsymbol{F}_M^{-1}\cdot\boldsymbol{\varphi}\right]\, da - \int\limits_{\partial\mathscr{B}_t} \boldsymbol{t}_t \otimes \left[\boldsymbol{F}_M^{-1}\cdot\boldsymbol{\varphi}_M\right]\, da - \int\limits_{\partial\mathscr{B}_t} \boldsymbol{t}_t \otimes \left[\boldsymbol{F}_M^{-1}\cdot\boldsymbol{w}\right]\, da\right] \tag{3.26}$$

for the right-hand side. $\boldsymbol{F}_M^{-1}$ and $\boldsymbol{\varphi}_M$ are constant for each RVE and thus can be extracted from the integrals which results in

$$\left[\mathrm{D}_\delta \boldsymbol{F}_M \cdot \boldsymbol{F}_M^{-1}\right] : \frac{1}{V_t}\left[\int\limits_{\partial\mathscr{B}_t} \boldsymbol{t}_t \otimes \boldsymbol{\varphi}\, \mathrm{d}a - \int\limits_{\partial\mathscr{B}_t} \boldsymbol{t}_t\, \mathrm{d}a \otimes \boldsymbol{\varphi}_M - \int\limits_{\partial\mathscr{B}_t} \boldsymbol{t}_t \otimes \boldsymbol{w}\, \mathrm{d}a\right]. \tag{3.27}$$

Therein, the second integral vanishes due to the antiperiodic tractions and the last integral equals zero due to the periodic fluctuations. Thus, in case of periodic boundary conditions and a geometrically periodic RVE the Hill-Mandel condition can be transformed into the following format

$$\left[\mathrm{D}_\delta \boldsymbol{F}_M \cdot \boldsymbol{F}_M^{-1}\right] : \boldsymbol{\sigma}_M - \mathrm{D}_\delta \boldsymbol{\varphi}_M \cdot \boldsymbol{b}_{tM} \equiv \left[\mathrm{D}_\delta \boldsymbol{F}_M \cdot \boldsymbol{F}_M^{-1}\right] : \frac{1}{V_t}\int\limits_{\partial\mathscr{B}_t} \boldsymbol{t}_t \otimes \boldsymbol{\varphi}\, \mathrm{d}a. \tag{3.28}$$

A comparison of coefficients in this equation yields that the averaged Cauchy stress equals the macroscopic Cauchy stress and that the macroscopic volume forces vanish, i.e.,

$$\boldsymbol{\sigma}_M \equiv \bar{\boldsymbol{\sigma}} \quad \text{and} \quad \boldsymbol{b}_{tM} = \boldsymbol{0}. \tag{3.29}$$

Remark 2 *Due to the fact that it has been shown that for periodic boundary conditions in an arbitrary geometrically periodic RVE the microscopic volume forces need to vanish –see equation* (3.17)*– vanishing microscopic volume forces are also assumed for the displacement boundary conditions. With this assumption relation* (3.29) *can also be shown for displacement boundary conditions as given in* (3.12).

Alternatively, the Hill-Mandel condition may also be expressed in terms of the Piola stress via

$$\mathscr{P}_{0M} = \mathrm{D}_\delta U_{0M} \equiv \mathrm{D}_\delta \bar{U}_0 = \bar{\mathscr{P}}_0 \tag{3.30}$$

$$\mathrm{D}_\delta \boldsymbol{F}_M : \boldsymbol{P}_M - \mathrm{D}_\delta \boldsymbol{\varphi}_M \cdot \boldsymbol{b}_{0M} \equiv \frac{1}{V_0}\int\limits_{\partial\mathscr{B}_0} \mathrm{D}_\delta \boldsymbol{\varphi} \cdot \boldsymbol{t}_0\, \mathrm{d}A. \tag{3.31}$$

Application of the previously assumed displacement or periodic boundary conditions

and the vanishing volume forces in the RVE yields

$$\mathrm{D}_\delta \boldsymbol{F}_M : \boldsymbol{P}_M - \mathrm{D}_\delta \boldsymbol{\varphi}_M \cdot \boldsymbol{b}_{0M} = \mathrm{D}_\delta \boldsymbol{F}_M : \frac{1}{V_0} \int_{\partial \mathscr{B}_0} \boldsymbol{t}_0 \otimes \boldsymbol{X} \, \mathrm{d}A. \tag{3.32}$$

The definition of the averaged Piola stress (3.7) and a comparison of coefficients yields the following relation for the macroscopic variables

$$\boldsymbol{P}_M = \bar{\boldsymbol{P}} \quad \text{and} \quad \boldsymbol{b}_{0M} = \boldsymbol{0}. \tag{3.33}$$

In a next step, the connection between the macroscopic stress measures is elaborated. Therefore, the micro-to-macro transition as given in equation (3.8) is inserted into the definition of the averaged Piola stress. Together with relation (3.33) this yields

$$\boldsymbol{P}_M = \frac{1}{V_0} \left[- \int_{\partial \mathscr{B}_0} \boldsymbol{t}_0 \, \mathrm{d}A \otimes \left[\boldsymbol{F}_M^{-1} \cdot \boldsymbol{\varphi}_M \right] + \int_{\partial \mathscr{B}_0} \boldsymbol{t}_0 \otimes \boldsymbol{\varphi} \, \mathrm{d}A \cdot \boldsymbol{F}_M^{-t} - \int_{\partial \mathscr{B}_0} \boldsymbol{t}_0 \otimes \boldsymbol{w} \, \mathrm{d}A \cdot \boldsymbol{F}_M^{-t} \right]. \tag{3.34}$$

The first integrand on the right-hand side of this equation vanishes due to the self-equilibrated tractions across the boundary, while the last integrand vanishes due to the boundary conditions. Insertion of the relation between the spatial and the material volume of the RVE

$$J_M = \frac{V_t}{V_0}, \tag{3.35}$$

and the definition of the averaged Cauchy stress (3.5) and its relation to the macroscopic Cauchy-stress yields the desired correlation of the macroscopic stress measures

$$\boldsymbol{P}_M = J_M \, \boldsymbol{\sigma}_M \cdot \boldsymbol{F}_M^{-t}. \tag{3.36}$$

Thus, for the spatial motion problem the macroscopic Piola and Cauchy stresses are connected by the standard push-forward operation, compare equation (2.16).

3.2.2 Stress-Based Approach

For the sake of completeness, also a stress-based approach is shortly introduced. In this approach the scale-transition from the macro- to the micro-level is defined in terms of the macroscopic Piola stresses $\boldsymbol{P}_M$ and the stress fluctuations $\boldsymbol{P}^{\mathrm{fluc}}$ via

$$\boldsymbol{P} = \boldsymbol{P}_M + \boldsymbol{P}^{\mathrm{fluc}}(\boldsymbol{X}). \tag{3.37}$$

Within the applied stress-driven approach, the scale-transition is required to be consistent in the stresses, i.e., the average stress theorem which claims the equivalence

of the averaged and the macroscopic Piola stress should hold,

$$\bar{\boldsymbol{P}} \equiv \boldsymbol{P}_M. \tag{3.38}$$

Application of the definition of the averaged Piola stress yields

$$\begin{aligned} \boldsymbol{P}_M &= \frac{1}{V_0} \int_{\partial \mathscr{B}_0} \boldsymbol{t}_0 \otimes \boldsymbol{X} \, \mathrm{d}A \\ &= \frac{1}{V_0} \int_{\partial \mathscr{B}_0} [\boldsymbol{P} \cdot \boldsymbol{N}] \otimes \boldsymbol{X} \, \mathrm{d}A \\ &= \boldsymbol{P}_M \cdot \frac{1}{V_0} \int_{\partial \mathscr{B}_0} \boldsymbol{N} \otimes \boldsymbol{X} \, \mathrm{d}A + \frac{1}{V_0} \int_{\partial \mathscr{B}_0} \left[\boldsymbol{P}^{\mathrm{fluc}} \cdot \boldsymbol{N}\right] \otimes \boldsymbol{X} \, \mathrm{d}A. \end{aligned} \tag{3.39}$$

Therein, the first integral on the right-hand side reduces to the second-order identity tensor $\boldsymbol{I}$ and thus (3.39) yields the following constraint

$$\boldsymbol{P}^{\mathrm{fluc}} = \boldsymbol{0} \quad \text{on} \quad \partial \mathscr{B}_0, \tag{3.40}$$

which is equivalent to constant traction boundary conditions which are given by

$$\boldsymbol{t}_0 = \boldsymbol{P}_M \cdot \boldsymbol{N} \quad \text{on} \quad \partial \mathscr{B}_0. \tag{3.41}$$

In analogy to the deformation-based approach focus is put onto the Hill-Mandel condition, here formulated in terms of the Piola stress –see equations (3.30) and (3.31). Insertion of the traction boundary condition into this consistency condition yields

$$\mathrm{D}_\delta \boldsymbol{F}_M : \boldsymbol{P}_M - \mathrm{D}_\delta \boldsymbol{\varphi}_M \cdot \boldsymbol{b}_{0M} = \left[\frac{1}{V_0} \int_{\partial \mathscr{B}_0} \mathrm{D}_\delta \boldsymbol{\varphi} \otimes \boldsymbol{N} \, \mathrm{d}A \right] : \boldsymbol{P}_M = \mathrm{D}_\delta \bar{\boldsymbol{F}} : \boldsymbol{P}_M, \tag{3.42}$$

and thus a comparison of coefficients gives the following result.

$$\mathrm{D}_\delta \boldsymbol{F}_M = \mathrm{D}_\delta \bar{\boldsymbol{F}} \quad \text{and} \quad \boldsymbol{b}_{0M} = \boldsymbol{0}. \tag{3.43}$$

In contrast to the deformation-based approach, in the stress-driven approach only a relation between the variation of the macroscopic and the averaged deformation gradient can be established.

In order to embed the constant traction boundary conditions into a deformation-driven FE-scheme an ansatz based on a Lagrangian multiplier is adopted which has been proposed by Miehe in [57]. In this approach it is furthermore necessary to assume that the average strain theorem is valid, compare equation (3.10). More details on the implementation of the constant traction boundary conditions into the deformation-driven FE-scheme are given in Section 3.3.3.

3.3 Numerical Implementation of the Spatial Homogenization Scheme

In the following section, the general algorithm of the applied FE^2 scheme and the implementation of the different boundary conditions are outlined. The nested solution scheme for the deformation-driven case which is the framework for the work at hand is displayed in Figure 3.3. After the initialization step, which is necessary to generate a starting point for the simulation, a loop over all macroscopic load steps is performed and then the macroscopic Newton-Raphson iteration, which is required due to the non-linearity of the problem, is started in each load increment. Then, at each macroscopic simulation point the downscaling to the micro-level, captured in the RVE, is carried out and the microscopic boundary value problem is formulated in terms of admissible boundary conditions.

At the micro-level a further Newton-Raphson iteration is required in order to solve the non-linear boundary value problem within a finite element scheme. After solving the micro-problem iteratively, the homogenization process is accomplished. Therefore, the macroscopic stress and the tangent modulus are determined as averages over the microscopic boundary. The discrete formulas for the determination of the averaged quantities are given in the next sections for all three applied boundary conditions. In a next step, these averaged quantities are passed to the corresponding macroscopic simulation point and the macroscopic FE calculation can continue. This down- and upscaling process is performed in the presented nested manner until macroscopic convergence is reached.

3.3.1 Linear Displacement Boundary Conditions

In the following, the numerical implementation of the linear displacement boundary conditions on the micro-level is shortly outlined. Here, the starting point is a discretized micro-structure accordingly to Figure 3.4 and the goal is to determine the macroscopic Piola stress $\boldsymbol{P}_M$ and fourth-order tangent stiffness tensor $\mathbb{C}_M$ which connects the increments of the macroscopic stresses and strains via

$$\Delta \boldsymbol{P}_M = \mathbb{C}_M : \Delta \boldsymbol{F}_M. \tag{3.44}$$

In the work at hand, the numerical implementation is based on a direct condensation of degrees of freedom as proposed in the work of Kouznetsova et al. [49]. Alternatively, the boundary constraints may be imposed by employing a Lagrange multiplier formulation, see, e.g., the work of Miehe and Koch [58] for the small strain formulation and the work of Miehe [57] for the finite strain case.

Firstly, the microscopic node set is divided into n_{bc} boundary nodes occupying the material coordinates $\boldsymbol{X}^{\text{bc}}$ and n_{in} inner nodes initially located at $\boldsymbol{X}^{\text{in}}$, see Figure 3.5.

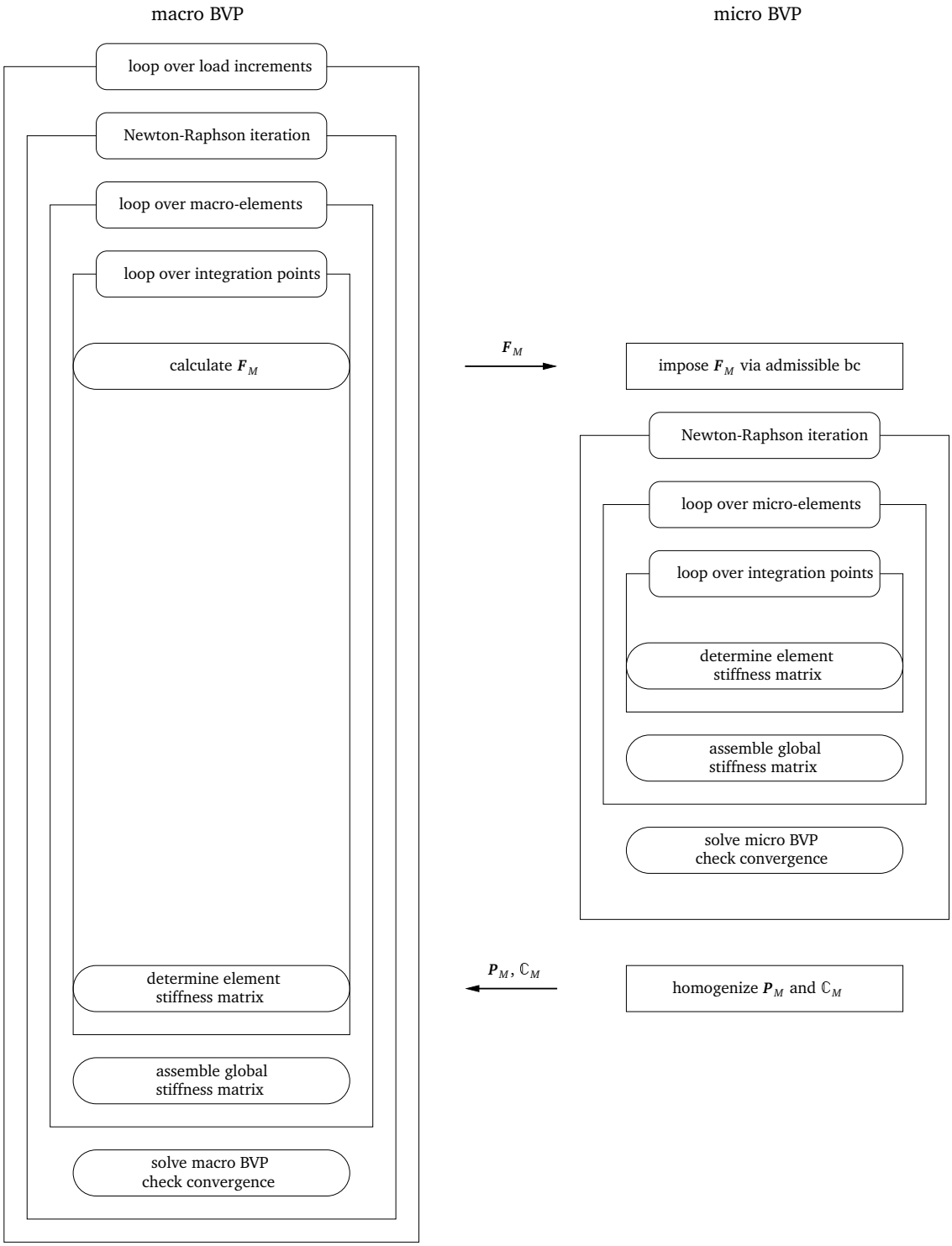

Figure 3.3: Nested FE^2 solution scheme for the deformation-driven scale transition

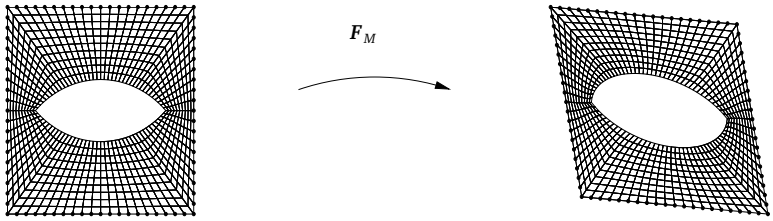

Figure 3.4: Microscopic RVE under displacement boundary conditions

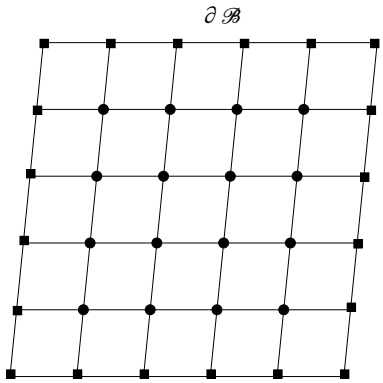

Figure 3.5: Schematic discretization of RVE, boundary nodes represented by ■, inner nodes by ●

Then, the displacement boundary conditions are imposed incrementally (incrementally, due to the applied Newton-Raphson scheme, necessary to solve the non-linear system of equations) in terms of the macroscopic deformation gradient tensor $\boldsymbol{F}_M$, which yields the discretized format of (3.12) applied to (3.8) as

$$\boldsymbol{u}_i^{\mathrm{bc}} = \left[\boldsymbol{F}_M - \boldsymbol{I}\right] \cdot \boldsymbol{X}_i^{\mathrm{bc}} \quad \forall\, i = 1, \cdots, n_{\mathrm{bc}}. \tag{3.45}$$

Thereby, the constant part φ_M contained in equation (3.8) is neglected due to the fact that it only causes a rigid body motion, which does not influence the required homogenized stresses and tangent moduli. Furthermore, the discretized format of the homogenized macroscopic first Piola-Kirchhoff stress –compare equation (3.7)– is given via

$$\bar{\boldsymbol{P}} = \sum_{i=1}^{n_{\mathrm{bc}}} \boldsymbol{f}_i^{\mathrm{bc}} \otimes \boldsymbol{X}_i^{\mathrm{bc}}, \tag{3.46}$$

wherein $\boldsymbol{f}_i^{\mathrm{bc}}$ corresponds to the resulting external forces at the boundary nodes. Within the applied FE scheme at the micro-level, these forces can be obtained through the partition of the global stiffness matrix $\boldsymbol{K}$ into degrees of freedom connected to the boundary and the inner nodes

$$\begin{bmatrix} \boldsymbol{K}^{\mathrm{bc,bc}} & \boldsymbol{K}^{\mathrm{bc,in}} \\ \boldsymbol{K}^{\mathrm{in,bc}} & \boldsymbol{K}^{\mathrm{in,in}} \end{bmatrix} \cdot \begin{bmatrix} \boldsymbol{u}^{\mathrm{bc}} \\ \boldsymbol{u}^{\mathrm{in}} \end{bmatrix} = \begin{bmatrix} \boldsymbol{f}^{\mathrm{bc}} \\ \boldsymbol{0} \end{bmatrix}. \tag{3.47}$$

The direct condensation yields the required force vector as

$$\boldsymbol{f}^{\mathrm{bc}} = \boldsymbol{K}^{R} \cdot \boldsymbol{u}^{\mathrm{bc}}, \tag{3.48}$$

whereby the reduced stiffness matrix is given by

$$\boldsymbol{K}^{R} = \boldsymbol{K}^{\mathrm{bc,bc}} - \boldsymbol{K}^{\mathrm{bc,in}} \cdot \left(\boldsymbol{K}^{\mathrm{in,in}}\right)^{-1} \cdot \boldsymbol{K}^{\mathrm{in,bc}}. \tag{3.49}$$

Thus, the resulting external forces in each boundary node $i = 1, \cdots n_{\mathrm{bc}}$ can be determined via

$$\boldsymbol{f}_{i}^{\mathrm{bc}} = \sum_{j=1}^{n_{\mathrm{bc}}} \boldsymbol{K}_{ij}^{R} \cdot \boldsymbol{u}_{j}^{\mathrm{bc}}. \tag{3.50}$$

Insertion of this nodal forces and application of the displacement boundary conditions (3.45) to equation (3.46) finally yields the desired format to calculate the homogenized Piola stress

$$\bar{\boldsymbol{P}} = \sum_{i=1}^{n_{\mathrm{bc}}} \sum_{j=1}^{n_{\mathrm{bc}}} \left[\boldsymbol{K}_{ij}^{R} \cdot \left[\boldsymbol{F}_{M} \cdot \boldsymbol{X}_{j}^{\mathrm{bc}} \right] \right] \otimes \boldsymbol{X}_{i}^{\mathrm{bc}}. \tag{3.51}$$

In order to derive the macroscopic tangent stiffness such that relation (3.44) is valid the equivalence of $\bar{\boldsymbol{F}}$ and $\boldsymbol{F}_{M}$, see Section 3.2.1, is invoked and thus equations (3.51) and (3.45) yield

$$\mathbb{C}_{M} = \sum_{i=1}^{n_{\mathrm{bc}}} \sum_{j=1}^{n_{\mathrm{bc}}} \boldsymbol{K}_{ij}^{R} \overline{\otimes} \left[\boldsymbol{X}_{i}^{\mathrm{bc}} \otimes \boldsymbol{X}_{j}^{\mathrm{bc}} \right]. \tag{3.52}$$

Thereby, $\overline{\otimes}$ corresponds to the non-standard dyadic product $\mathbb{A} = A_{ijkl} = \boldsymbol{B} \overline{\otimes} \boldsymbol{D} = B_{ik} D_{jl}$, compare equation (2.46).

3.3.2 Periodic Boundary Conditions

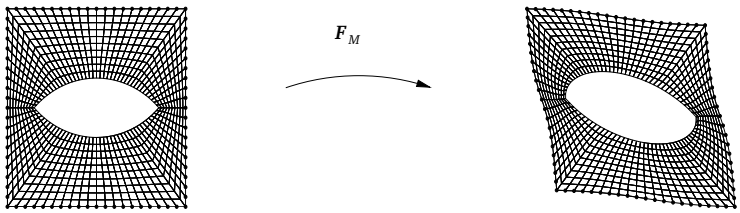

Figure 3.6: Microscopic RVE under periodic boundary conditions

Analogously to the previous section, the macroscopic Piola stress $\boldsymbol{P}_{M}$ and the corresponding tangent operator $\mathbb{C}_{M}$ are elaborated depending on the applied boundary conditions. In case of periodic boundary conditions it is assumed that the underlying RVE is geometrically periodic. Thereby, two different types of periodicities can

be discerned, namely local periodicity where the assigned RVEs are periodic within a certain region, and global periodicity where the same periodic RVEs occur in the whole macroscopic setting, compare Figure 3.7.

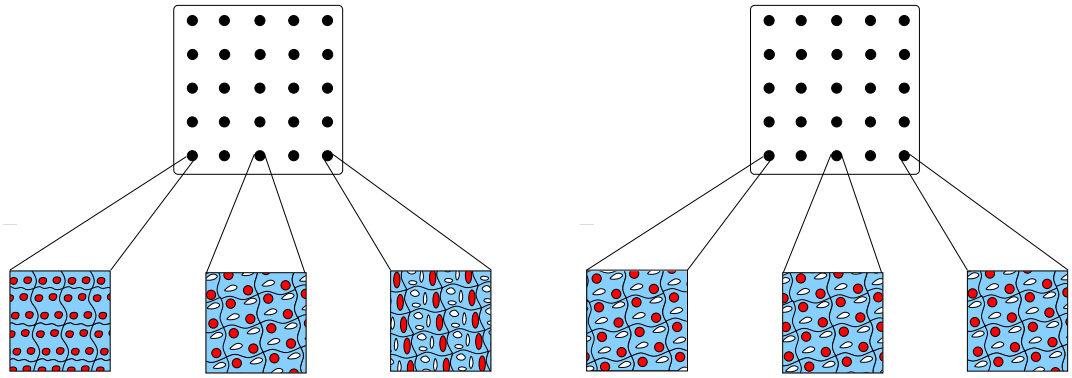

Figure 3.7: Local versus global periodicity

In order to apply the periodic boundary conditions to the RVE, firstly the boundary of the RVE $\partial \mathscr{B}_0$ has to be split up in a positive and a negative part as displayed in Figure 3.8, according to

$$\partial \mathscr{B}_0 = \partial \mathscr{B}_0^+ \cup \partial \mathscr{B}_0^- \quad \text{and} \quad \partial \mathscr{B}_0^+ \cap \partial \mathscr{B}_0^- = \emptyset. \tag{3.53}$$

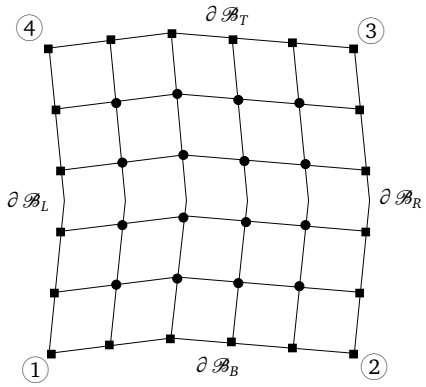

Figure 3.8: Microscopic RVE with partitioned boundary and corner nodes

Within the numerical simulation the increments of the macroscopic deformation gradient $\boldsymbol{F}_M$ should be imposed to the microscopic boundary such that

$$\boldsymbol{w}^+ = \boldsymbol{w}^-, \tag{3.54}$$

is valid. Therefore, the incremental formulation of the scale-transition as given in

(3.8) is considered, which yields the following format for the boundary fluctuations

$$\boldsymbol{w}^+ = \boldsymbol{u}^+ - \boldsymbol{F}_M \cdot \boldsymbol{X}^+ \tag{3.55}$$
$$\boldsymbol{w}^- = \boldsymbol{u}^- - \boldsymbol{F}_M \cdot \boldsymbol{X}^-, \tag{3.56}$$

whereby $\boldsymbol{\varphi}_M$ has been neglected because rigid body motions do not influence the homogenized stresses. The periodicity condition as given in equation (3.54) and subtraction of equations (3.55) and (3.56) yields that the periodicity can also be formulated via

$$\boldsymbol{u}^+ - \boldsymbol{u}^- = \boldsymbol{F}_M \cdot \left[\boldsymbol{X}^+ - \boldsymbol{X}^-\right]. \tag{3.57}$$

The assumed geometrical periodicity of the RVE demands that the distance between opposite node pairs remains constant. Thus, it is only necessary to determine the distance between one pair of left-right and top-bottom node pairs. To capture this numerically, the boundary nodes (or respectively the corresponding degrees of freedom) are divided into the corner nodes 1, 2, 4 and the nodes on the top, bottom, left and right side. This partitioning of the boundary nodes is illustrated in Figure 3.8. Please note, that it has to be taken into account that the corner nodes belong to two node sets, each. Then, it is sufficient to apply the macroscopic deformation gradient only to the corner nodes 1, 2 and 4, i.e.,

$$\boldsymbol{u}_i = \boldsymbol{F}_M \cdot \boldsymbol{X}_i \quad \text{for } i = 1, 2, 4. \tag{3.58}$$

The periodic fluctuations are ensured by the following tying of the top and bottom node pairs and the left and right nodes pairs

$$\boldsymbol{u}_R = \boldsymbol{u}_L + \boldsymbol{u}_2 - \boldsymbol{u}_1 \tag{3.59}$$
$$\boldsymbol{u}_T = \boldsymbol{u}_B + \boldsymbol{u}_4 - \boldsymbol{u}_1. \tag{3.60}$$

These tying conditions also enforce the position of the corner node 3.

In the following, it is not further distinguished between nodes and the corresponding degrees of freedom. For simplicity only nodes and node sets are described.

In order to implement the periodic boundary conditions as outlined above, the nodes in the RVE are divided into the set of dependent nodes, which are given by the nodes on the right and on the top of the boundary, according to the dependency elaborated in equations (3.59)-(3.60), and the independent node set which captures the remaining nodes, i.e., the corner nodes 1, 2, 4, the left and the bottom boundary nodes and the inner nodes. Then, the transformation matrices $\boldsymbol{C}^i$ and $\boldsymbol{C}^d$ are generated, which connect the independent and the dependent node displacements via

$$\begin{bmatrix} \boldsymbol{C}^i & \boldsymbol{C}^d \end{bmatrix} \cdot \begin{bmatrix} \boldsymbol{u}^i \\ \boldsymbol{u}^d \end{bmatrix} = \boldsymbol{0}, \tag{3.61}$$

such that the periodicity conditions (3.59)-(3.60) are valid, see, e.g., Kouznetsova [48] or the textbook by Cook et al. [10] for details. With assistance of

these transformation matrices, the dependency matrix $\boldsymbol{C}$ is defined as

$$\boldsymbol{C} = -(\boldsymbol{C}^d)^{-1} \cdot \boldsymbol{C}^i, \tag{3.62}$$

and thus the relation between the dependent and the independent nodal displacements reads

$$\boldsymbol{u}^d = \boldsymbol{C} \cdot \boldsymbol{u}^i. \tag{3.63}$$

The system of equation to obtain the incremental displacements is rewritten in terms of the independent and the dependent node sets as

$$\begin{bmatrix} \boldsymbol{K}^{ii} & \boldsymbol{K}^{id} \\ \boldsymbol{K}^{di} & \boldsymbol{K}^{dd} \end{bmatrix} \cdot \begin{bmatrix} \boldsymbol{u}^i \\ \boldsymbol{u}^d \end{bmatrix} = \begin{bmatrix} \boldsymbol{f}^i \\ \boldsymbol{f}^d \end{bmatrix}. \tag{3.64}$$

Application of equation (3.63) and multiplication of the second row with $\boldsymbol{C}^t$ from the left yields

$$\begin{aligned} \left[\boldsymbol{K}^{ii} + \boldsymbol{K}^{id} \cdot \boldsymbol{C}\right] \cdot \boldsymbol{u}^i &= \boldsymbol{f}^i & (3.65) \\ \left[\boldsymbol{C}^t \cdot \boldsymbol{K}^{di} + \boldsymbol{C}^t \cdot \boldsymbol{K}^{dd} \cdot \boldsymbol{C}\right] \cdot \boldsymbol{u}^i &= \boldsymbol{C}^t \cdot \boldsymbol{f}^d. & (3.66) \end{aligned}$$

Addition of these two equations yields a system of equations only depending on the increments of the independent displacements, that is

$$\boldsymbol{K}^* \cdot \boldsymbol{u}^i = \boldsymbol{f}^*, \tag{3.67}$$

with

$$\begin{aligned} \boldsymbol{K}^* &= \boldsymbol{K}^{ii} + \boldsymbol{K}^{id} \cdot \boldsymbol{C} + \boldsymbol{C}^t \cdot \boldsymbol{K}^{di} + \boldsymbol{C}^t \cdot \boldsymbol{K}^{dd} \cdot \boldsymbol{C} & (3.68) \\ \boldsymbol{f}^* &= \boldsymbol{f}^i + \boldsymbol{C}^t \cdot \boldsymbol{f}^d. & (3.69) \end{aligned}$$

In a next step, the system of equations is further reduced to a system which only contains the prescribed incremental displacements at the corner nodes 1,2 4. Therefore, the system is condensed into the set c of corner nodes 1, 2, 4 and the set of free independent nodes f which are given by the inner nodes and the nodes at the left and the bottom boundary, which yields the following partition

$$\begin{bmatrix} \boldsymbol{K}^{*cc} & \boldsymbol{K}^{*cf} \\ \boldsymbol{K}^{*fc} & \boldsymbol{K}^{*ff} \end{bmatrix} \cdot \begin{bmatrix} \boldsymbol{u}^c \\ \boldsymbol{u}^f \end{bmatrix} = \begin{bmatrix} \boldsymbol{f}^c \\ \boldsymbol{0} \end{bmatrix}. \tag{3.70}$$

Thus, the resulting forces at the corner nodes with prescribed displacements can be determined via

$$\boldsymbol{f}^c = \boldsymbol{K}^{**} \cdot \boldsymbol{u}^c, \tag{3.71}$$

whereby the condensed stiffness matrix is given as

$$\boldsymbol{K}^{**} = \boldsymbol{K}^{*cc} - \boldsymbol{K}^{*ct} \cdot (\boldsymbol{K}^{*cc})^{-1} \cdot \boldsymbol{K}^{*fc}. \tag{3.72}$$

Therefore, for each of single corner node $i = 1, 2, 4$ the resulting force reads

$$\boldsymbol{f}_i^c = \sum_{j=1,2,4} \boldsymbol{K}_{ij}^{**} \cdot \boldsymbol{u}_j^c. \tag{3.73}$$

Due to the fact that the boundary nodes, except corner nodes 1,2 and 4, are only displaced via the tying forces, which cancel out on opposite nodes due to the antiperiodic tractions, the sum over all boundary nodes in the determination of the homogenized stresses reduces to a sum over the prescribed corner nodes, i.e., it holds

$$\bar{\boldsymbol{P}} = \sum_{i=1,2,4} \sum_{j=1,2,4} \left[\boldsymbol{K}_{ij}^{**} \cdot \left[\boldsymbol{F}_M \cdot \boldsymbol{X}_j^c \right] \right] \otimes \boldsymbol{X}_i^c. \tag{3.74}$$

According to Section 3.3.1, the corresponding macroscopic tangent stiffness matrix can then be determined via

$$\sum_{i=1,2,4} \sum_{j=1,2,4} \boldsymbol{K}_{ij}^{**} \overline{\otimes} \left[\boldsymbol{X}_i^c \otimes \boldsymbol{X}_j^c \right]. \tag{3.75}$$

Alternatively to the presented formulation based on the dependency matrix, the periodicity can also be ensured by a Lagrange parameter, see the work of Miehe [57] for details.

3.3.3 Constant Traction Boundary Conditions

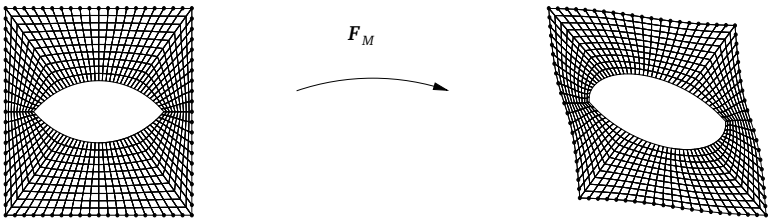

Figure 3.9: Microscopic RVE under traction boundary conditions

In the following section it is outlined in which manner the constant traction boundary conditions can be ensured within the applied deformation driven-process based on the work of Miehe [57]. In this work, the scale-transition based on minimizing the averaged energy is considered. To this end, the basic assumptions are pointed out and the algorithmic implementation is given. In contrast to the publication cited above, in the work at hand, no Lagrange multiplier formulation is applied in the derivation of the averaged stresses and tangent moduli.

In the deformation-driven approach the constant tractions $\boldsymbol{t}_0 = \boldsymbol{P}_M \cdot \boldsymbol{N}$ cannot be applied directly to the boundary of the RVE due to the fact that the macroscopic stress $\boldsymbol{P}_M$ is a-priori not known. Therefore, it is necessary to claim some properties on the a-priori known macroscopic deformation gradient $\boldsymbol{F}_M$. As a consequence

of the Hill-Mandel condition (3.42) the variation of the macroscopic deformation gradient equals the variation of the averaged deformation gradient –see (3.43). In order to enforce constant tractions, it is assumed that this relation does not only hold weakly, but also strongly, i.e.,

$$\boldsymbol{F}_M = \bar{\boldsymbol{F}}, \tag{3.76}$$

is assumed. Therefore, the following equation holds

$$\frac{1}{V_0} \int_{\partial \mathscr{B}_0} \boldsymbol{\varphi} \otimes \boldsymbol{N} \, \mathrm{d}A - \boldsymbol{F}_M = \boldsymbol{0}. \tag{3.77}$$

With regard to the discretized form of this equation, which is required to implement the constant traction boundary conditions, the discretized nodal area vector is introduced for every boundary node q according to the work by Miehe [57] via

$$\boldsymbol{A}_q := \frac{1}{2} \left[\boldsymbol{X}_{q+1} - \boldsymbol{X}_{q-1} \right] \times \boldsymbol{e}_3, \tag{3.78}$$

whereby $\boldsymbol{e}_3$ denotes the out-of-plane cartesian base vector. With assistance of this discrete area vector, the discretized form of equation (3.77) reads

$$\frac{1}{V_0} \mathbb{N} \cdot \boldsymbol{x}^{\mathrm{bc}} - \boldsymbol{F}_M = \boldsymbol{0}, \tag{3.79}$$

whereby the area matrix for all boundary nodes is given by

$$\mathbb{N} := \begin{bmatrix} \mathbb{N}_1 & \mathbb{N}_2 & \dots & \mathbb{N}_{n_{bc}} \end{bmatrix}, \tag{3.80}$$

and for each boundary node q it holds

$$\mathbb{N}_q := \begin{bmatrix} A_1 & 0 \\ 0 & A_2 \\ A_2 & 0 \\ 0 & A_1 \end{bmatrix}_q. \tag{3.81}$$

By application of this area matrix, the demand of constant tractions on the boundary can be rewritten in discretized format via

$$\mathbb{N}^t \cdot \widetilde{\boldsymbol{P}}_M = \boldsymbol{t}_0, \tag{3.82}$$

wherein $\widetilde{\boldsymbol{P}}_M$ corresponds to the vector notation of the Piola stress, i.e.,

$$\widetilde{\boldsymbol{P}}_M = \begin{bmatrix} P_{11} & P_{22} & P_{12} & P_{21} \end{bmatrix}^t. \tag{3.83}$$

Thus, the non-linear set of equations, which has to be solved to calculate the homog-

enized stresses in the context of constant tractions within the deformation-driven scheme can be summarized as

$$\begin{aligned} \boldsymbol{f}^{\mathrm{in}} &= \boldsymbol{0} && (3.84)\\ \boldsymbol{f}^{\mathrm{bc}} - \mathbb{N}^t \cdot \widetilde{\widetilde{\boldsymbol{P}}} &= \boldsymbol{0} && (3.85)\\ \mathbb{N} \cdot \boldsymbol{x}^{\mathrm{bc}} - V_0 \boldsymbol{F}_M &= \boldsymbol{0}. && (3.86) \end{aligned}$$

Thereby, the first equation corresponds to the fact that the nodes in the interior of the RVE are free nodes. The second equation results from the demanded constant tractions at the boundary and the average stress theorem (3.33), which is a consequence of these boundary conditions. Within the applied Newton-Raphson scheme, the set of equations (3.84) – (3.85) is solved iteratively and thus in the iteration step $i+1$ it holds

$$\begin{aligned} {}^{i+1}\boldsymbol{f}^{\mathrm{in}} &= \boldsymbol{0} && (3.87)\\ {}^{i+1}\boldsymbol{f}^{\mathrm{bc}} - \mathbb{N}^t \cdot {}^{i+1}\widetilde{\widetilde{\boldsymbol{P}}} &= \boldsymbol{0} && (3.88)\\ \mathbb{N} \cdot {}^{i+1}\boldsymbol{x}^{\mathrm{bc}} - V_0 \cdot \boldsymbol{F}_M &= \boldsymbol{0}. && (3.89) \end{aligned}$$

The updates in each iteration step are performed via

$$\begin{aligned} {}^{i+1}\boldsymbol{f}^{\mathrm{in}} &= {}^{i}\boldsymbol{f}^{\mathrm{in}} + \Delta\boldsymbol{f}^{\mathrm{in}}\\ {}^{i+1}\boldsymbol{f}^{\mathrm{bc}} &= {}^{i}\boldsymbol{f}^{\mathrm{bc}} + \Delta\boldsymbol{f}^{\mathrm{bc}}\\ {}^{i+1}\boldsymbol{x}^{\mathrm{bc}} &= {}^{i}\boldsymbol{x}^{\mathrm{bc}} + \Delta\boldsymbol{u}^{\mathrm{bc}}\\ {}^{i+1}\widetilde{\widetilde{\boldsymbol{P}}} &= {}^{i}\widetilde{\widetilde{\boldsymbol{P}}} + \Delta\widetilde{\widetilde{\boldsymbol{P}}}. && (3.90) \end{aligned}$$

Please note, that in the deformation-driven process no update for $\boldsymbol{F}_M$ is necessary due to the fact that the macroscopic deformation gradient remains constant within the microscopic iteration. The set of equations is completed by the standard update equation for the resulting forces in terms of the global stiffness matrix

$$\boldsymbol{K} \cdot \Delta\boldsymbol{u} = \Delta\boldsymbol{f}, \tag{3.91}$$

which can be partitioned into the degrees of freedom in the interior of the domain and at the boundary of the domain by

$$\begin{bmatrix} \boldsymbol{K}^{\mathrm{bc,bc}} & \boldsymbol{K}^{\mathrm{bc,in}} \\ \boldsymbol{K}^{\mathrm{in,bc}} & \boldsymbol{K}^{\mathrm{in,in}} \end{bmatrix} \cdot \begin{bmatrix} \Delta\boldsymbol{u}^{\mathrm{bc}} \\ \Delta\boldsymbol{u}^{\mathrm{in}} \end{bmatrix} = \begin{bmatrix} \Delta\boldsymbol{f}^{\mathrm{bc}} \\ \Delta\boldsymbol{f}^{in} \end{bmatrix}. \tag{3.92}$$

Application of the update equation (3.90) to equation (3.87) and insertion of the second part of (3.92) yields the incremental displacements of the microscopic inner nodes as

$$\Delta\boldsymbol{u}^{\mathrm{in}} = -(\boldsymbol{K}^{\mathrm{in,in}})^{-1} \cdot \left[{}^{i}\boldsymbol{f}^{\mathrm{in}} + \boldsymbol{K}^{\mathrm{in,bc}} \cdot \Delta\boldsymbol{u}^{\mathrm{bc}} \right]. \tag{3.93}$$

Therefore, the displacement increments at the boundary nodes can be obtained by

a static condensation of (3.92) adopted to (3.88) which yields

$$\Delta \boldsymbol{u}^{\mathrm{bc}} = -(\boldsymbol{K}^R)^{-1} \cdot \left[\boldsymbol{f}^R - \mathbb{N}^t \cdot {}^i\widetilde{\widetilde{\boldsymbol{P}}} - \mathbb{N}^t \cdot \Delta\widetilde{\widetilde{\boldsymbol{P}}} \right]. \tag{3.94}$$

The condensed stiffness matrix is given by

$$\boldsymbol{K}^R = \boldsymbol{K}^{\mathrm{bc,bc}} - \boldsymbol{K}^{\mathrm{bc,in}} \cdot (\boldsymbol{K}^{\mathrm{in,in}})^{-1} \cdot \boldsymbol{K}^{\mathrm{in,bc}}, \tag{3.95}$$

and the condensed residual vector by

$$\boldsymbol{f}^R = {}^i\boldsymbol{f}^{\mathrm{bc}} - \boldsymbol{K}^{\mathrm{bc,in}} \cdot (\boldsymbol{K}^{\mathrm{in,in}})^{-1} \cdot {}^i\boldsymbol{f}^{\mathrm{in}}. \tag{3.96}$$

Due to the fact that no degrees of freedom at the microscopic boundary are restricted, the stiffness matrix $\boldsymbol{K}^{\mathrm{in,in}}$ needs to be disturbed by a diagonal mass-matrix to ensure regularity. With these results, the desired update of the averaged stress vector can be determined via

$$\Delta\widetilde{\widetilde{\boldsymbol{P}}} = \left[\mathbb{N} \cdot (\boldsymbol{K}^R)^{-1} \cdot \mathbb{N}^t \right]^{-1} \cdot \left[-\mathbb{N} \cdot {}^i\boldsymbol{x}^{\mathrm{bc}} + \mathbb{N} \cdot (\boldsymbol{K}^R)^{-1} \cdot \left[\boldsymbol{f}^R - \mathbb{N}^t \cdot {}^i\widetilde{\widetilde{\boldsymbol{P}}} \right] + V_0 \boldsymbol{F}_M \right], \tag{3.97}$$

and therefore the homogenized tangent modulus in matrix notation reads

$$\widetilde{\mathbb{C}}_M = \left[\mathbb{N} \cdot (\boldsymbol{K}^R)^{-1} \cdot \mathbb{N}^t \right]^{-1} V_0. \tag{3.98}$$

Thus, an incremental solution has been developed which can be applied to guarantee constant tractions at the boundary within a deformation-driven scheme.

3.4 Numerical Examples –Spatial Motion Problem

In the following section, various numerical examples are given to illustrate the influence of boundary conditions and different RVEs onto the spatial homogenization process. Firstly, focus is put onto microscopic problems, i.e., a macroscopic deformation gradient is prescribed, which corresponds to a macroscopic structure consisting only of one simulation point. With assistance of these examples the homogenized stresses are compared for different boundary conditions. In a second step, macro-micro transitions are simulated and thus the impact of different microscopic RVEs onto the macroscopic structures is studied. Furthermore, for reinforced micro-structures represented by a matrix with embedded fibers effective material parameters are calculated and the influence of different fiber concentrations, lengths and orientations is investigated.

3.4.1 Microscopic Examples –Spatial Motion Problem

In a first step, the impact of the previously developed admissible boundary conditions on the averaged stresses is illustrated for different microscopic deformations.

Therefore, different macroscopic deformation gradients $\boldsymbol{F}_M$ are prescribed and applied via different boundary conditions to the same RVE. The considered RVE is represented by a quadratic specimen with a void in the upper left corner. It is assumed that this structure consists of a hyperelastic material, i.e., the stored energy density function of the Neo-Hooke type is applied

$$\Psi_0 = \frac{1}{2}\lambda \ln^2 J + \frac{1}{2}\mu \left[\left[\boldsymbol{F} \cdot \boldsymbol{F}^t \right] : \boldsymbol{I} - 2 - 2\ln J \right], \tag{3.99}$$

see Section 2.3 for details. The Young's modulus and the Poisson's ratio are chosen as $E = 1000\,\mathrm{N/mm^2}$ and $\nu = 0.3$ which result according to (2.32) in $\lambda = 576.92\,\mathrm{N/mm^2}$ and $\mu = 384.61\,\mathrm{N/mm^2}$.

In Figure 3.10 the deformed RVEs under different types of boundary conditions and the corresponding averaged Cauchy stresses are displayed for a prescribed stretch in x-direction.

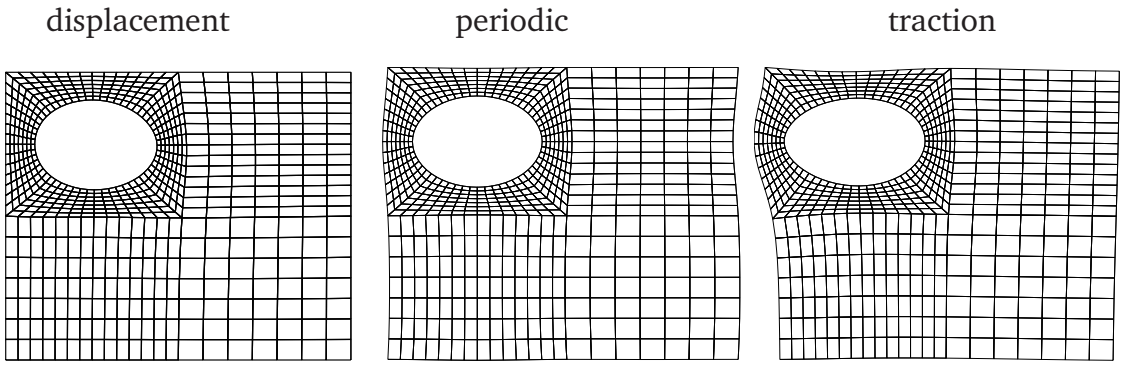

$$\bar{\boldsymbol{\sigma}}^{\mathrm{disp}} = \begin{bmatrix} 399.2 & 1.5 \\ 1.5 & 101.7 \end{bmatrix} \qquad \bar{\boldsymbol{\sigma}}^{\mathrm{peri}} = \begin{bmatrix} 390.0 & 0.0 \\ 0.0 & 99.2 \end{bmatrix} \qquad \bar{\boldsymbol{\sigma}}^{\mathrm{trac}} = \begin{bmatrix} 372.4 & 0.6 \\ 0.6 & 99.9 \end{bmatrix}$$

Figure 3.10: Deformed RVEs and corresponding averaged Cauchy stresses in $[\mathrm{N/mm^2}]$, applied stretch in x-direction, $\boldsymbol{F}_M = [1.2 \quad 0.0;\ 0.0 \quad 1.0]$

These plots reveal that in case of the displacement boundary conditions the boundary of the RVE remains straight while for the traction and for the periodic boundary conditions the boundary gets deformed. For the latter ones the periodicity can be observed in the upper half of the RVE. Furthermore, the Cauchy stresses σ_{xx} point out that the displacement boundary conditions yield the stiffest averaged material response and the traction boundary conditions the softest one.

The same characteristics can be tracked in Figure 3.11 where the RVEs are displayed for an applied stretch in y-direction. It can be realized that in contrast to a stretch in x-direction the σ_{xx} and the σ_{yy} components of the stress tensor are ex-

changed whereas the shear components are the same, which are both consequences of the symmetric shape and the symmetric arrangement of the circular void.

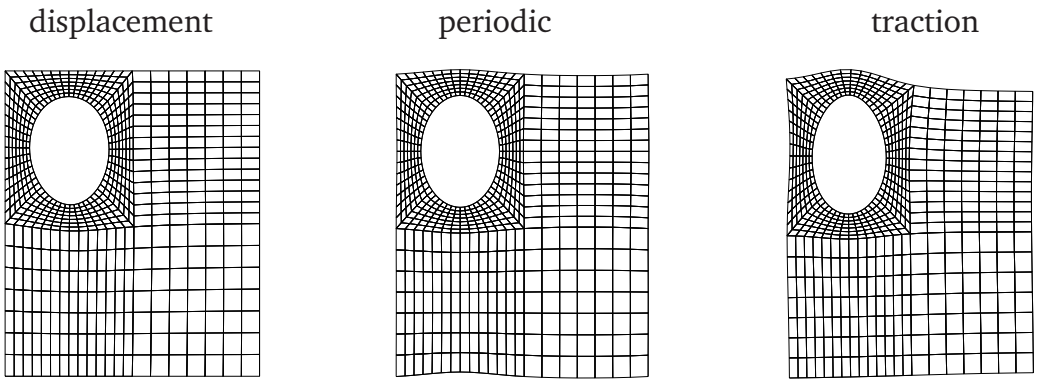

$$\bar{\boldsymbol{\sigma}}^{\text{disp}} = \begin{bmatrix} 101.7 & 1.5 \\ 1.5 & 399.2 \end{bmatrix} \qquad \bar{\boldsymbol{\sigma}}^{\text{peri}} = \begin{bmatrix} 99.2 & 0.0 \\ 0.0 & 390.0 \end{bmatrix} \qquad \bar{\boldsymbol{\sigma}}^{\text{trac}} = \begin{bmatrix} 99.9 & 0.6 \\ 0.6 & 372.4 \end{bmatrix}$$

Figure 3.11: Deformed RVEs and corresponding averaged Cauchy stresses in [N/mm^2], applied stretch in y-direction, $\boldsymbol{F}_M = [1.0 \quad 0.0;\ 0.0 \quad 1.2]$

The different deformations of the RVEs under different boundary conditions for the case of a prescribed simple shear are depicted in Figure 3.12. Again, the stiffer behavior of the linear displacements and the softer material response of the constant tractions can be observed. The softer behavior of the constant traction boundary conditions is further observable by the highly deformed RVE.

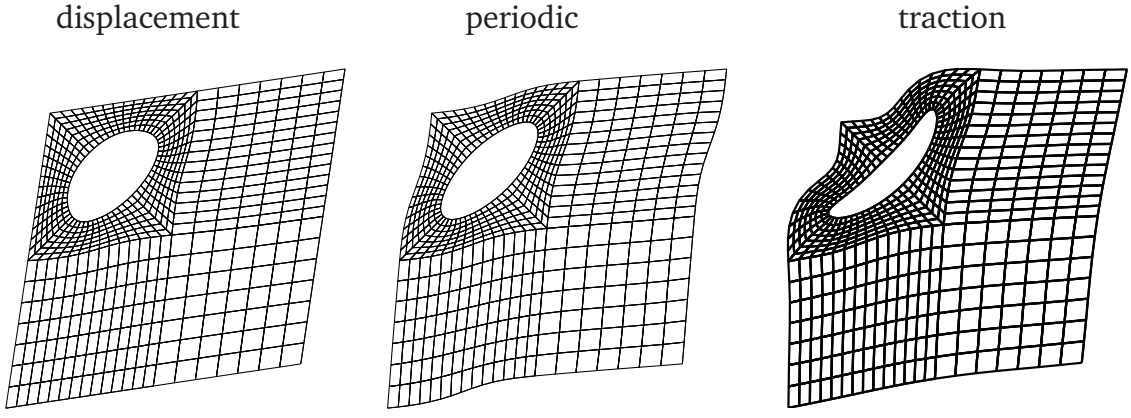

$$\bar{\boldsymbol{\sigma}}^{\text{disp}} = \begin{bmatrix} 6.0 & 162.7 \\ 162.7 & 6.0 \end{bmatrix} \qquad \bar{\boldsymbol{\sigma}}^{\text{peri}} = \begin{bmatrix} 8.7 & 150.8 \\ 150.8 & 8.7 \end{bmatrix} \qquad \bar{\boldsymbol{\sigma}}^{\text{trac}} = \begin{bmatrix} 21.6 & 133.7 \\ 133.7 & 21.6 \end{bmatrix}$$

Figure 3.12: Deformed RVEs and corresponding averaged Cauchy stresses in [N/mm^2] for shear deformation, $\boldsymbol{F}_M = [1.0 \quad 0.15;\ 0.15 \quad 1.0]$

Moreover, in Figure 3.13 a general deformation gradient is prescribed. This example indicates once more the difference in the averaged stresses and illustrates the different shapes of the deformed boundaries, i.e., the straight boundary in the case of linear displacements, the curved boundary for constant tractions, and the periodically curved boundary in the case of periodic fluctuations.

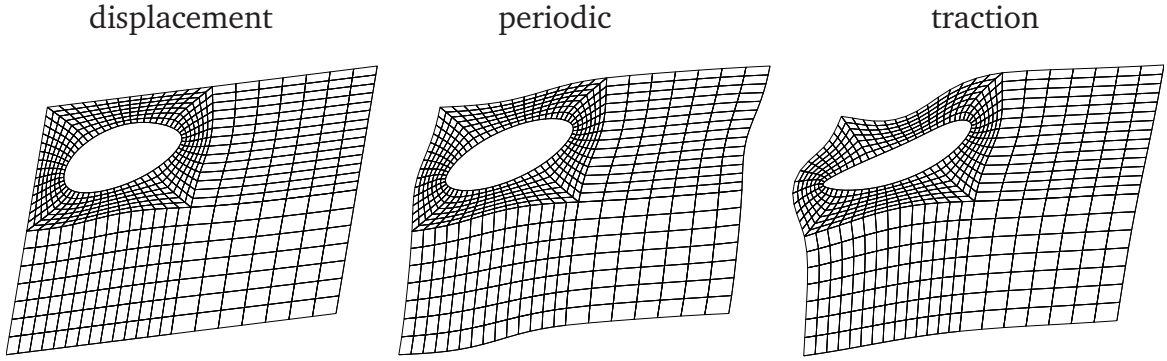

$$\bar{\boldsymbol{\sigma}}^{\text{disp}} = \begin{bmatrix} 307.3 & 186.7 \\ 186.7 & -65.6 \end{bmatrix} \qquad \bar{\boldsymbol{\sigma}}^{\text{peri}} = \begin{bmatrix} 302.2 & 175.4 \\ 175.4 & -59.5 \end{bmatrix} \qquad \bar{\boldsymbol{\sigma}}^{\text{trac}} = \begin{bmatrix} 302.8 & 165.4 \\ 165.4 & -26.5 \end{bmatrix}]$$

Figure 3.13: Deformed RVEs and corresponding averaged Cauchy stresses in [N/mm^2] for a general deformation, $\boldsymbol{F}_M = [1.2 \quad 0.15;\ 0.15 \quad 0.9]$

Consequently, it has been illustrated numerically that for different prescribed macroscopic deformation gradients the displacement boundary conditions yield the largest averaged stresses, the traction boundary conditions the smallest averaged stresses and the periodic boundary conditions are established in between. In the following section, various numerical examples for the coupling of macroscopic and microscopic structures are elaborated and the microscopic influence onto the macroscopic material behavior is studied.

3.4.2 Macro-Micro Transition –Spatial Motion Problem

In the current section examples for a full macro-micro transition are presented. Therefore, in the macro-structures at hand a microscopic RVE is attached to each single simulation point. The given examples are limited to the macro-homogeneous case, i.e., over the whole macro-domain the same RVE is assumed. In each of these simulation points the macro-micro scale-transition is performed according to Section 3.2. After solving the microscopic boundary value problem within the FE scheme, the averaging of the stress and the tangent modulus is carried out which allows the solution of the macroscopic boundary value problem.

In all following examples, a Neo-Hookean type material behavior has been assumed on the micro-level, see equation (3.99) for the stored energy functional and

Section 2.3 for details. On the macroscopic level a rectangular specimen with a centered hole is studied. Within the deformation-driven scheme at hand, displacements in longitudinal directions are prescribed. On this macroscopic level no constitutive assumption is necessary due to the fact that the macroscopic material behavior stems from the analysis of the underlying micro-structure

Influence of Boundary Conditions onto Macroscopic Material Response

In a first example, the influence of the applied boundary conditions onto the macroscopic material response is studied.

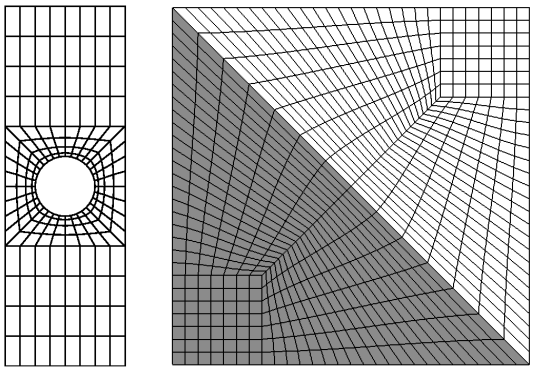

Figure 3.14: Undeformed macroscopic and microscopic structures

Therefore, on the micro-level a quadratic RVE is considered which consists of two materials with different stiffnesses connected by a diagonal interface, see Figure 3.14 for the undeformed microscopic setting. The material parameters are chosen such that one material is five times stiffer than the other one, i.e., it holds $E_1 = 500$ N/mm^2, $E_2 = 2500$ N/mm^2, $\nu_1 = \nu_2 = 0.3$ which results in the following Lamé constants $\lambda_1 = 288.46$ N/mm^2, $\lambda_2 = 1442.31$ N/mm^2, $\mu_1 = 192.31$ N/mm^2 and $\mu_2 = 961.54$ N/mm^2. The macro-micro transition is performed according to linear displacement, periodic and constant traction boundary conditions. In Figure 3.15 the macroscopic Cauchy stresses in longitudinal direction are monitored for the different boundary conditions. In this Figure from the left to the right the stress concentrations near the boundary of the hole becomes smaller which indicates that the displacement boundary conditions yields the stiffest macroscopic material response and the traction boundary conditions the softest one. This observation is approved by the load-displacement diagram, see Figure 3.16. The load-displacement curve of the linear displacements is above the other curves, the load-displacement curve of the constant tractions is the lowest curve, while the periodic boundary conditions yield a result which is in the middle. Due to this mean character only periodic boundary conditions are considered in the following.

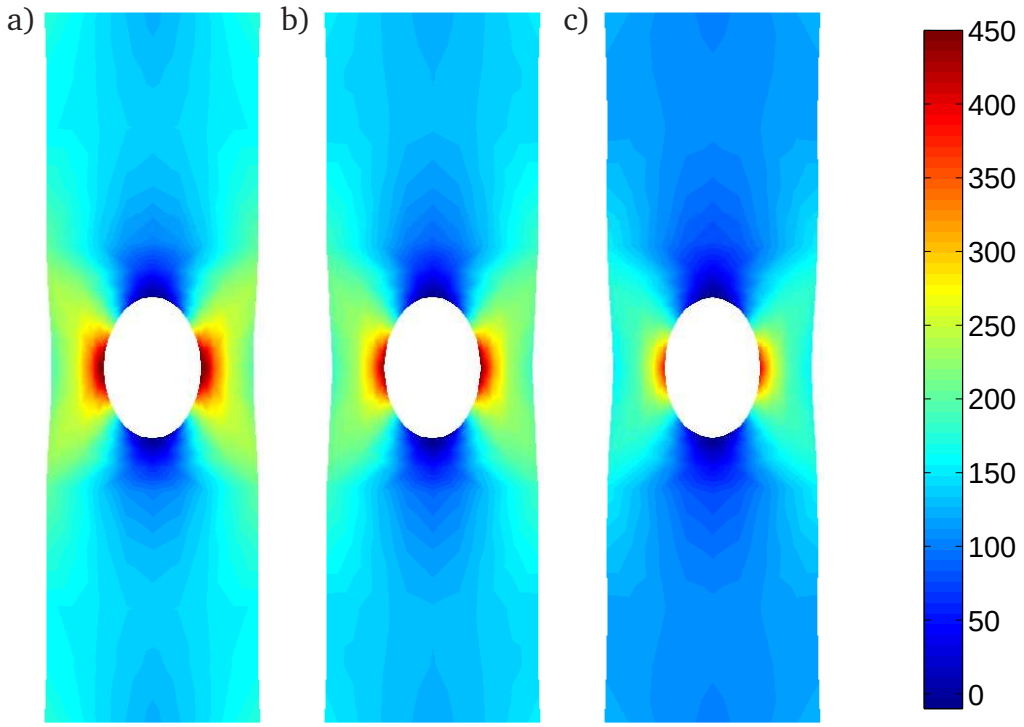

Figure 3.15: Macroscopic longitudinal Cauchy stress in [N/mm^2] for a) displacement, b) periodic and c) traction boundary conditions

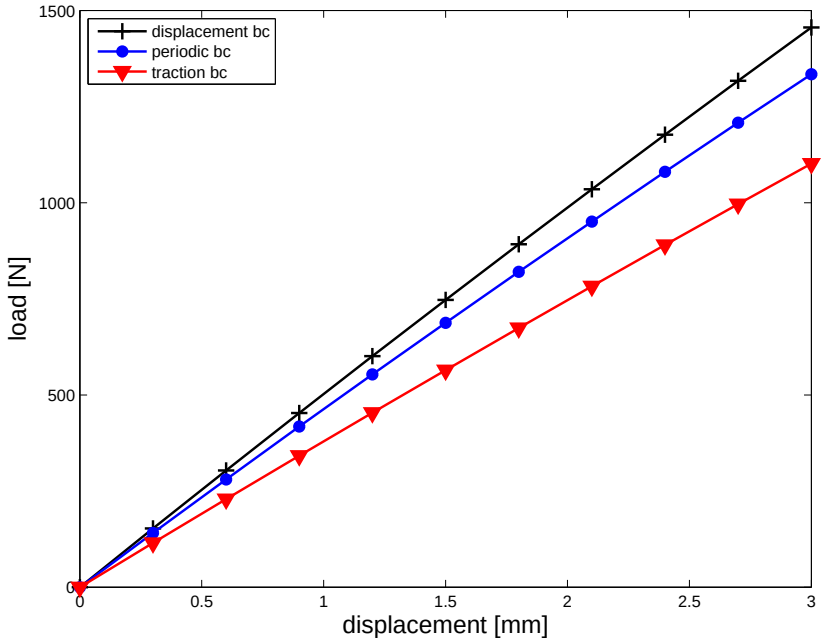

Figure 3.16: Macroscopic load-displacement diagram in longitudinal direction for different boundary conditions

The influence of the different types of boundary conditions also can be detected by zooming into the micro-structures and by analyzing the local strains and stresses. Therefore, in Figure 3.17 deformed RVEs located at a macroscopic simulation point near the boundary of the hole and the corresponding strains and stresses are displayed. Apparently, the displacement boundary conditions yield a straight microscopic boundary, while traction and periodic boundary conditions result in a curved boundary deformation. The differing stiffnesses of the macroscopic material response can substantially be observed by focusing on the σ_{yy} component of the averaged Cauchy stress.

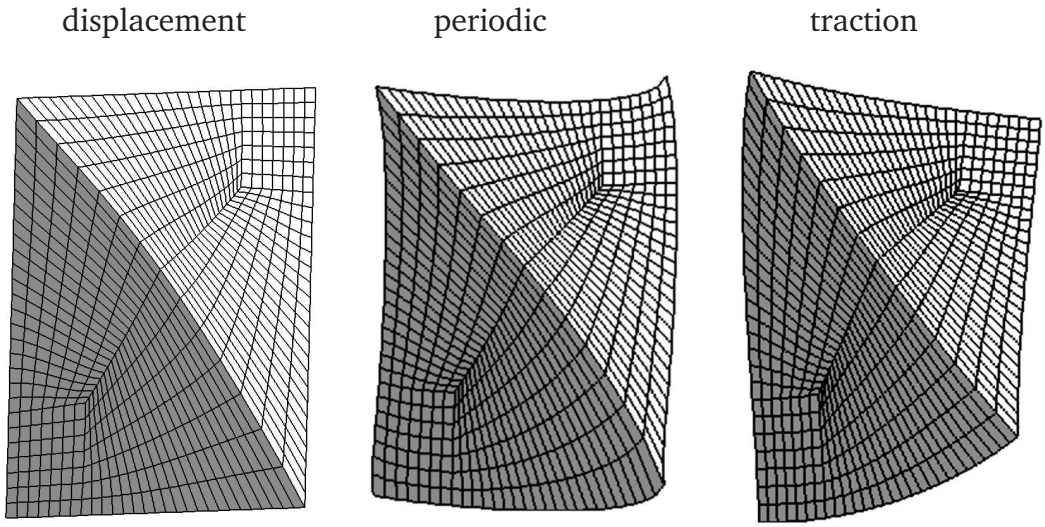

$$\boldsymbol{F}_M = \begin{bmatrix} 0.9364 & 0.0334 \\ 0.0336 & 1.3152 \end{bmatrix}, \quad \begin{bmatrix} 0.9335 & 0.0080 \\ 0.0334 & 1.3128 \end{bmatrix}, \quad \begin{bmatrix} 0.9216 & 0.0116 \\ 0.0294 & 1.3038 \end{bmatrix}$$

$$\bar{\boldsymbol{\sigma}} = \begin{bmatrix} 15.8404 & 3.0688 \\ 3.0688 & 553.7974 \end{bmatrix}, \quad \begin{bmatrix} 13.0806 & 3.9357 \\ 3.9357 & 492.3372 \end{bmatrix}, \quad \begin{bmatrix} 11.5200 & 3.1488 \\ 3.1488 & 404.3247 \end{bmatrix}$$

Figure 3.17: Deformed RVEs under different boundary conditions at a macroscopic simulation point near the boundary of the hole and corresponding macroscopic deformation gradients and homogenized Cauchy stresses in [N/mm^2]

Influence of Micro-Structure onto Macroscopic Material Response –Void Size

In the next example, the influence of the microscopic void size onto the macroscopic material behavior is studied. Therefore, a void free RVE and RVEs containing a circular centered void with 15 and 25 volume percent are compared, see Figure 3.18 for the undeformed meshes. The Young's modulus and the Poisson's ratio have been chosen as $E = 1000$ N/mm^2 and $\nu = 0.3$ which yields $\lambda = 576.92$ N/mm^2 and $\mu = 384.61$ N/mm^2.

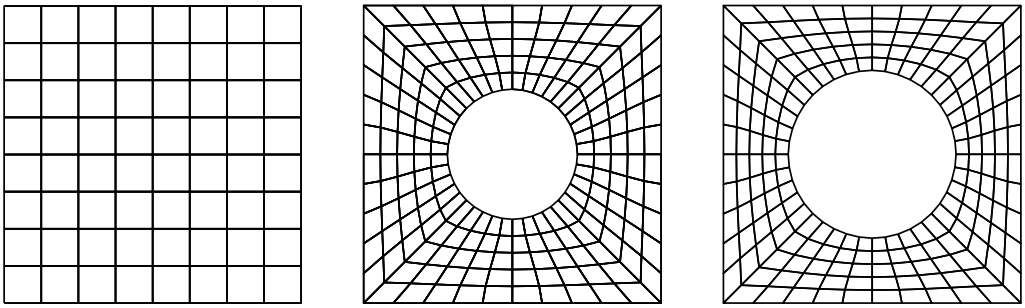

Figure 3.18: Undeformed microscopic structures containing a singular, circular, centered void with 0, 15 and 25 volume percent

Figure 3.19 displays the averaged Cauchy stresses in longitudinal direction for the different underlying micro-structures. From the left to the right, i.e., the direction in which the void becomes larger the stresses become significantly smaller and accordingly the stress peaks at the boundary of the macroscopic hole diminish. Thus, as expected the bigger void at the micro-scale results in a softer material response at the macroscopic level.

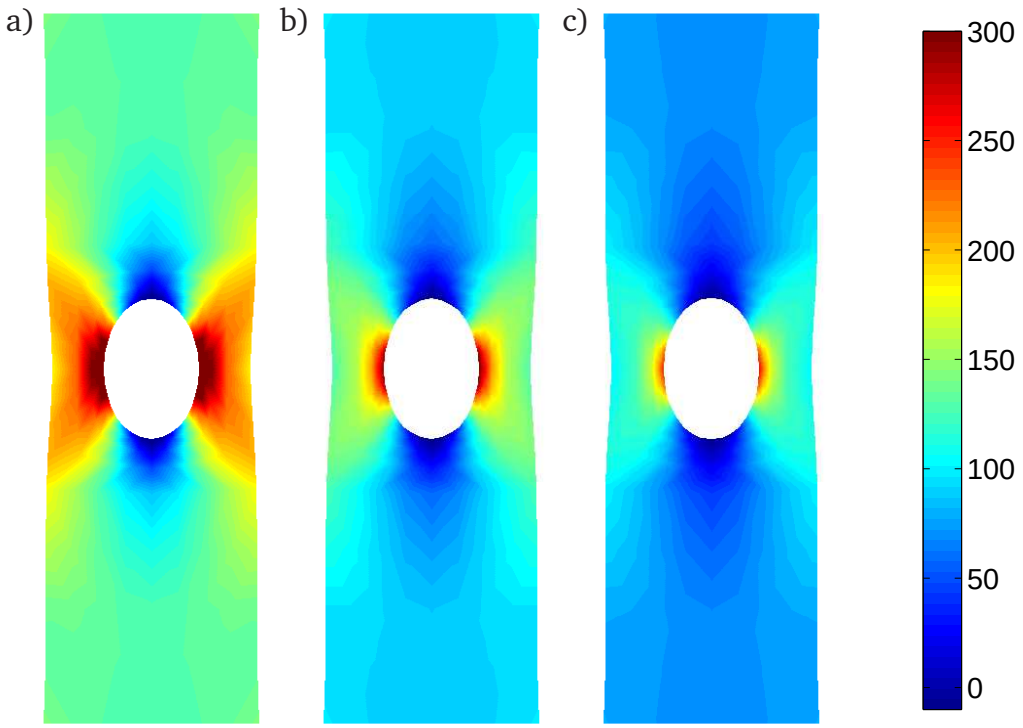

Figure 3.19: Macroscopic longitudinal Cauchy stresses in [N/mm^2] for an underlying micro-structure containing a single void with a) 0, b) 15 and c) 25 volume percent

This decrease in the macroscopic stiffness can also be observed in the macroscopic load-displacement diagrams pictured in Figure 3.20.

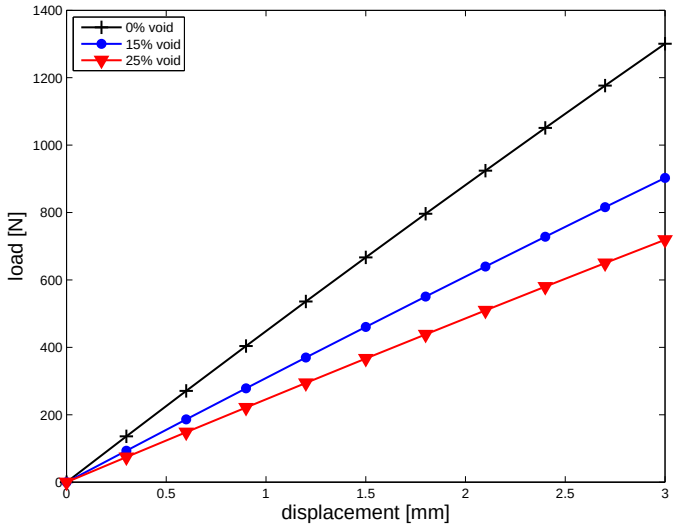

Figure 3.20: Macroscopic load-displacement diagram in longitudinal direction for underlying micro-structures containing differently sized voids

Furthermore, different deformed RVEs at the same macroscopic simulation point located near the boundary of the hole are depicted in Figure 3.21. Apparently, the influence of the void size onto the macroscopic stiffness can be observed in the averaged Cauchy stresses, which decrease with a bigger void fraction in the RVE.

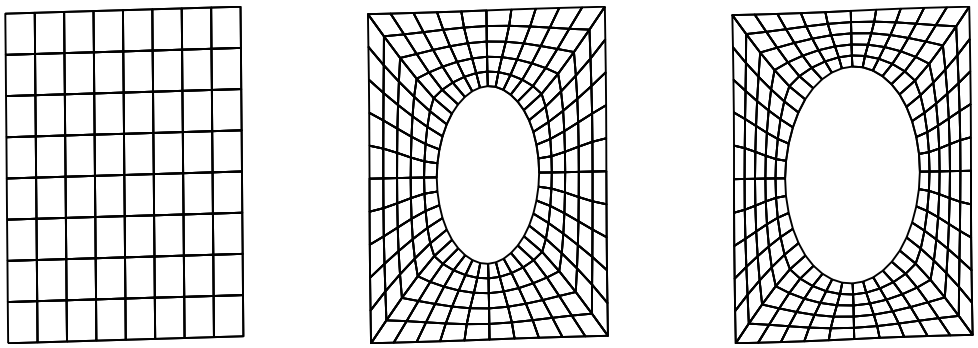

$$\boldsymbol{F}_M = \begin{bmatrix} 0.9267 & -0.0112 \\ 0.0274 & 1.2982 \end{bmatrix}, \begin{bmatrix} 0.9353 & -0.0124 \\ 0.0295 & 1.2999 \end{bmatrix}, \begin{bmatrix} 0.9430 & -0.0137 \\ 0.0334 & 1.3060 \end{bmatrix}$$

$$\bar{\boldsymbol{\sigma}} = \begin{bmatrix} 12.5368 & 5.8267 \\ 5.8267 & 459.3576 \end{bmatrix}, \begin{bmatrix} 8.1558 & 3.6752 \\ 3.6752 & 322.9320 \end{bmatrix}, \begin{bmatrix} 6.2637 & 2.6301 \\ 2.6301 & 261.5757 \end{bmatrix}$$

Figure 3.21: Deformed RVEs at a macroscopic simulation point near the boundary of the hole, macroscopic deformation gradients and homogenized Cauchy stresses in $[\mathrm{N/mm^2}]$

Influence of Micro-Structure onto Macroscopic Material Response –Inclusion Shape

In the next two examples the influence of the morphology of the RVE onto the macroscopic material response is studied. Firstly, two RVEs consisting of two materials are considered, and attached to the simulation points of the macroscopic specimen. One RVE contains a quadratic inclusion, whereas the other one contains a rectangular inclusion of the same size, see Figure 3.22 for the setting. The material parameters of the matrix have been chosen as $\lambda_1 = 576.92\ \mathrm{N/mm^2}$ and $\mu_1 = 384.61\ \mathrm{N/mm^2}$, whereas the material of the inclusions are twice as stiff as the matrix, i.e., $\lambda_2 = 1153.84\ \mathrm{N/mm^2}$ and $\mu_2 = 769.23\ \mathrm{N/mm^2}$.

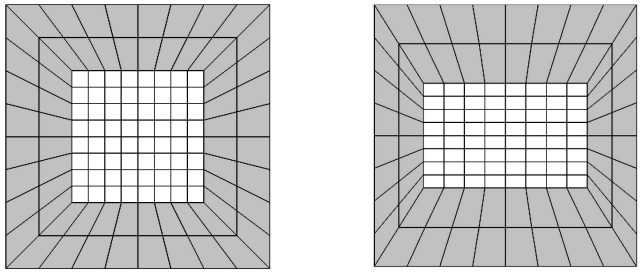

Figure 3.22: Undeformed microscopic structures containing a quadratic and a rectangular inclusion

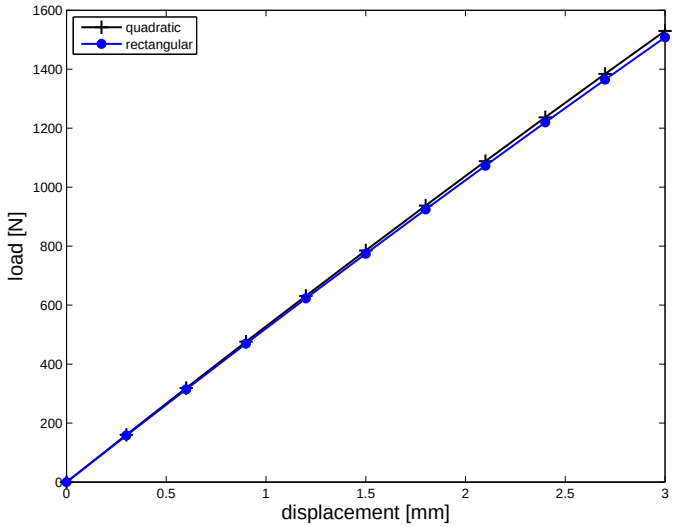

Figure 3.23: Macroscopic load-displacement diagram in longitudinal direction for underlying micro-structures containing differently shaped inclusions

The macroscopic load-displacement diagram in Figure 3.23 displays that the different shape of the microscopic inclusion also influences the macroscopic material response, the quadratic inclusion yields a marginal stiffer macroscopic behavior.

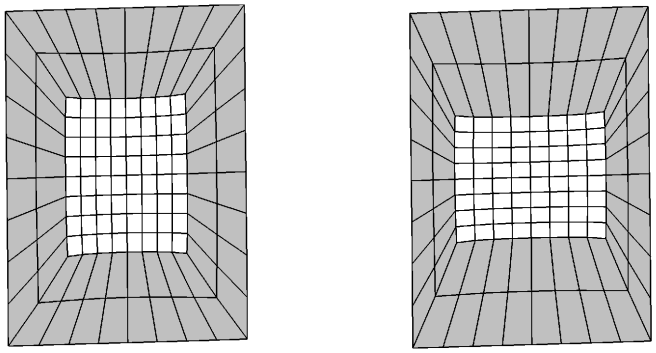

$$\boldsymbol{F}_M = \begin{bmatrix} 0.9286 & -0.0114 \\ 0.0278 & 1.2993 \end{bmatrix}, \quad \begin{bmatrix} 0.9295 & -0.0116 \\ 0.0277 & 1.2991 \end{bmatrix}$$

$$\bar{\boldsymbol{\sigma}} = \begin{bmatrix} 14.5483 & 6.7241 \\ 6.7241 & 540.0147 \end{bmatrix}, \quad \begin{bmatrix} 14.3189 & 6.4988 \\ 6.4988 & 531.0810 \end{bmatrix}$$

Figure 3.24: Deformed RVEs at a macroscopic simulation point near the boundary of the hole, macroscopic deformation gradients and homogenized Cauchy stresses in $[\mathrm{N/mm^2}]$

This tendency is also illustrated in Figure 3.24, where deformed RVEs, which are located at a simulation point near the boundary of the macroscopic hole, and the corresponding deformation gradients and the averaged stresses are depicted. For the RVE with the rectangular inclusion all stress components of $\bar{\boldsymbol{\sigma}}$ are smaller than the stress components for the RVE with the quadratic inclusion, and thus the quadratic inclusion results in a stiffer macroscopic material response.

Influence of Micro-Structure onto Macroscopic Material Response –Void Orientation

In a last example, the influence of the microscopic morphology onto the macroscopic material behavior is studied. Therefore, two RVEs containing a lentil-shaped void which is orientated horizontally and vertically are compared, see Figure 3.25 for the undeformed settings.

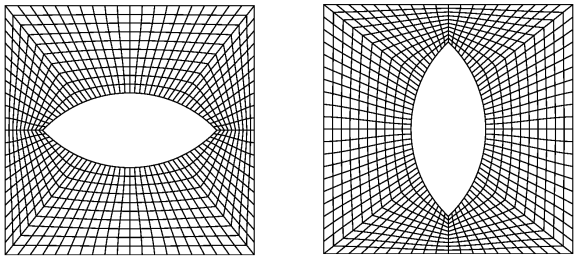

Figure 3.25: Undeformed microscopic structures containing different lens-like voids

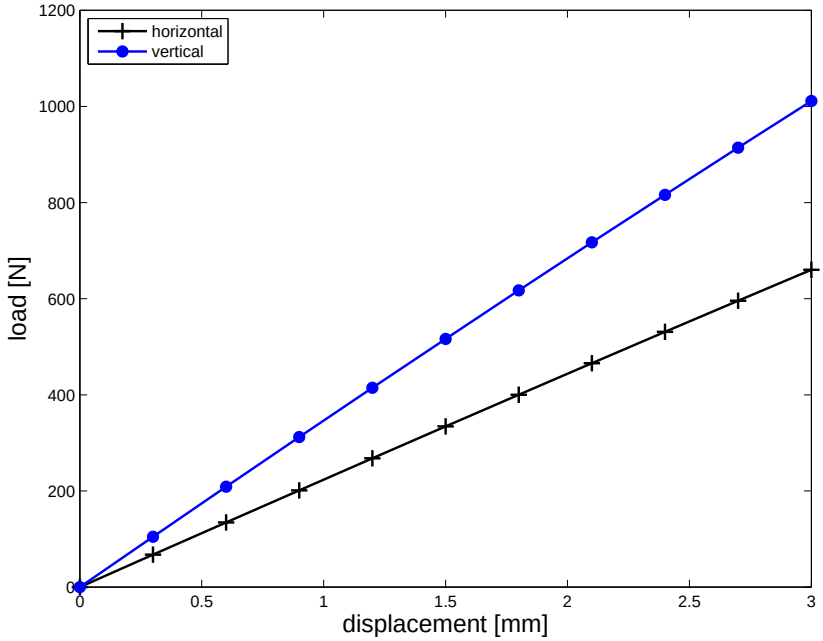

Figure 3.26: Macroscopic load-displacement diagram in longitudinal direction for underlying micro-structures containing differently orientated lens-like voids

The material parameters on the micro-level are given by $\lambda = 576.92$ N/mm^2 and $\mu = 384.61$ N/mm^2. The macroscopic load-displacement diagram in Figure 3.26 reveals that the RVE with the vertically orientated lentil-shaped void yields a significantly stiffer material response than the RVE with the horizontally orientated void. This behavior is due to the fact that the horizontally voided RVE has the largest discontinuity orthogonal to the macroscopic longitudinal direction which corresponds to the main loading direction.

The different stiffnesses in the macroscopic material response can also be observed in the macroscopic Cauchy stresses in longitudinal direction, see Figure 3.27. In the contour plot at the right-hand side of the Figure, which displays the underlying RVE with the vertical lens-like void, significant stress peaks appear near the boundary of the hole and thus in contrast to the horizontal void the material shows a stiffer response.

Concluding, in the last examples it has been shown that different microscopic properties at the RVE level influence the macroscopic material response. First of all, different boundary conditions for the scale-transition between the macro- and the micro-level have been compared. Then, the influence of the void size onto the macroscopic stiffness has been analyzed and finally it has been illustrated that also the microscopic morphology, like the void shape and orientation influence the macroscopic quantities.

In the sequel, further applications of the computational homogenization scheme are elaborated. Therefore, focus is put onto the determination of effective material parameters of randomly generated RVEs, which consist of a matrix material which is reinforced by fibers.

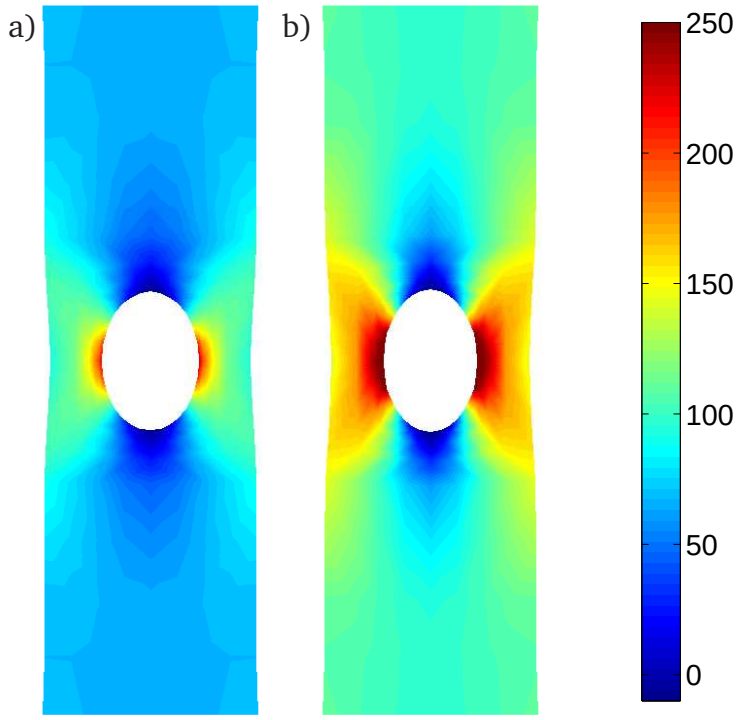

Figure 3.27: Averaged Cauchy stresses in [N/mm^2] in longitudinal direction for underlying RVEs with a) horizontally and b) vertically orientated lens-like void

3.4.3 Embedded Truss Elements

In the current section the homogenization scheme is applied to determine effective material properties instead of performing a macro-micro transition in each simulation point. Therefore, a thermoplastic matrix material reinforced by fiber-glass is considered. In contrast to the previously elaborated examples, here only the small strain case is considered, i.e., no distinction between the material and the spatial coordinates has to be taken into account. For both, the matrix and the fiber material

a linear connection between the stresses and the strains is assumed, and thus the Hooke's law

$$\boldsymbol{\sigma} = \mathbb{C} : \boldsymbol{\epsilon}, \tag{3.100}$$

is valid. Thereby, $\boldsymbol{\epsilon}$ corresponds to the symmetric part of the displacement gradient, i.e.,

$$\boldsymbol{\epsilon} = \nabla \boldsymbol{u}^{\text{sym}} = \frac{1}{2}\left[\nabla \boldsymbol{u} + (\nabla \boldsymbol{u})^t\right]. \tag{3.101}$$

In case of the adopted plane strain case, Hooke's law reduces in Voigt matrix notation to

$$\begin{bmatrix} \sigma_{11} \\ \sigma_{22} \\ \sigma_{12} \end{bmatrix} = \frac{E}{(1+\nu)(1-2\nu)} \begin{bmatrix} 1-\nu & \nu & 0 \\ \nu & 1-\nu & 0 \\ 0 & 0 & \frac{1-2\nu}{2} \end{bmatrix} \cdot \begin{bmatrix} \epsilon_{11} \\ \epsilon_{22} \\ 2\epsilon_{12} \end{bmatrix}. \tag{3.102}$$

The material parameters have been chosen according to the textbooks by Klein [46] and Schürmann [78] as $E = 3294\ \text{N/mm}^2$, $\nu = 0.35$ for the thermoelastic matrix and $E = 72000\ \text{N/mm}^2$, $\nu = 0.2$ for the fiber glass.

In order to perform computationally efficient simulations, the micro-structure is discretized with so-called embedded truss elements. Within this approach, in the fiber phase no standard discretization is carried out which would result in a very fine mesh and thus would need much computation time. Instead, only the matrix material is discretized by standard elements and the fibers are modeled by truss elements, which are inserted into the matrix. In this method, the fibers are not coupled to the nodes of the matrix mesh, they can be distributed arbitrarily. Further details as well as the implementation of this concept into the commercial tool ABAQUS and a wide range of examples can be found in the work of Schmitt [76].

The determination of the effective macroscopic elasticity matrix $\boldsymbol{C}_M^*$ is based on the following relation between the macroscopic stresses and strains

$$\begin{bmatrix} \sigma_{11} \\ \sigma_{22} \\ \sigma_{12} \end{bmatrix}_M = \begin{bmatrix} C_{11}^* & C_{12}^* & 0 \\ C_{21}^* & C_{22}^* & 0 \\ 0 & 0 & C_{33}^* \end{bmatrix}_M \cdot \begin{bmatrix} \epsilon_{11} \\ \epsilon_{22} \\ 2\epsilon_{12} \end{bmatrix}_M. \tag{3.103}$$

Therein, the components of $\boldsymbol{C}_M^*$ are determined by evaluation of the stress-strain relation for three prescribed loading cases, that is uniaxial tension in both directions and shear, i.e., the prescribed strains are given as

$$\boldsymbol{\epsilon}_M^1 = \begin{bmatrix} 0.01 \\ 0 \\ 0 \end{bmatrix}, \ \boldsymbol{\epsilon}_M^2 = \begin{bmatrix} 0 \\ 0.01 \\ 0 \end{bmatrix}, \ \boldsymbol{\epsilon}_M^3 = \begin{bmatrix} 0 \\ 0 \\ 0.02 \end{bmatrix}. \tag{3.104}$$

With assistance of this effective elasticity tensor also the effective Young's modulus

E^* can be determined as

$$E^* = \frac{1}{S^*_{11}}, \tag{3.105}$$

whereby $\boldsymbol{S}^*_M$ corresponds to the Voigt notation of the effective compliance tensor, i.e.,

$$\boldsymbol{S}^*_M = (\boldsymbol{C}^*_M)^{-1}, \tag{3.106}$$

see the book by Gross and Seelig [27] for details. In order to give an illustration of the effective Young's modulus in the following examples, E^* is plotted subjected to the angle of rotation in the RVE. Thus, the stresses and the strains are multiplied by the corresponding two-dimensional rotation matrices $\boldsymbol{T}_\sigma$ and $\boldsymbol{T}_\epsilon$, which depend on the rotation angle φ. Then, the elasticity matrix $\boldsymbol{C}^*_M(\varphi)$ and the compliance matrix $\boldsymbol{S}^*_M(\varphi)$ are established and according to (3.105) the effective Young's modulus with respect to the rotation angle $E^*(\varphi)$ is calculated. A further quantity for the interpretation of the effective properties of the material is the anisotropy ratio Z, see, e.g., the book by Buryachenko [8],

$$Z = \frac{2C^*_{33}}{C^*_{11} - C^*_{12}}, \tag{3.107}$$

which gives a measure of the deviation from an isotropic material, which is characterized by $Z = 1$.

In the following examples, the effective elasticity matrix and the effective Young's modulus of RVEs with different fiber reinforcements are compared. The elasticity matrix of the unreinforced matrix material is given by

$$\boldsymbol{C}^*_{\text{matrix}} = \begin{bmatrix} 5286.67 & 2846.67 & 0 \\ 2846.67 & 5286.67 & 0 \\ 0 & 0 & 1200.00 \end{bmatrix} \left[\,\text{N/mm}^2\right]. \tag{3.108}$$

In a first example this matrix material is reinforced by five vertical fibers. The effective elasticity matrix results in

$$\boldsymbol{C}^*_{\text{vert}} = \begin{bmatrix} 5286.67 & 2846.67 & 0 \\ 2846.67 & 7623.58 & 0 \\ 0 & 0 & 1200.00 \end{bmatrix} \left[\,\text{N/mm}^2\right], \tag{3.109}$$

whereas the anisotropy ratio $Z \approx 1$. A comparison of this stiffness with the pure matrix material yields that only the C^*_{22} differs while the other components are not increasing due to the relatively small fiber diameter in comparison to the fiber length. The anisotropy ratio almost equals 1 although the material is not isotropic because C^*_{22} does not contribute to the anisotropy ratio –compare equation (3.107). If in this equation C^*_{11} is replaced by C^*_{22} the anisotropy is reflected by an anisotropy ratio of $Z = 0.51$. This anisotropy can also be observed in the Young's modulus depending on the rotation angle, see Figure 3.28. The increase of the stiffness in fiber direction

can be proofed by comparison of the Young's modulus at $\varphi = 0°$ and $\varphi = 90°$, which are given by $E^*(0°) = 4223.7$ N/mm^2 and $E^*(90°) = 6090.8$ N/mm^2.

In a second example five horizontally orientated glass fibers are considered in the matrix material. The effective stiffness matrix is then given by

$$\boldsymbol{C}^*_{\text{horiz}} = \begin{bmatrix} 7623.58 & 2846.67 & 0 \\ 2846.67 & 5286.67 & 0 \\ 0 & 0 & 1200.00 \end{bmatrix} \left[\text{ N/mm}^2\right], \tag{3.110}$$

and the anisotropy ratio $Z = 0.51$. A comparison of this elasticity matrix to the elasticity matrix of the pure matrix material (3.108) yields that only the C^*_{11} component increases which corresponds to the fiber direction. Furthermore, it can be observed that if the fibers are rotated 90° also the diagram of the Young's modulus subjected to the rotation angle rotates 90°, compare Figures 3.29 and 3.28.

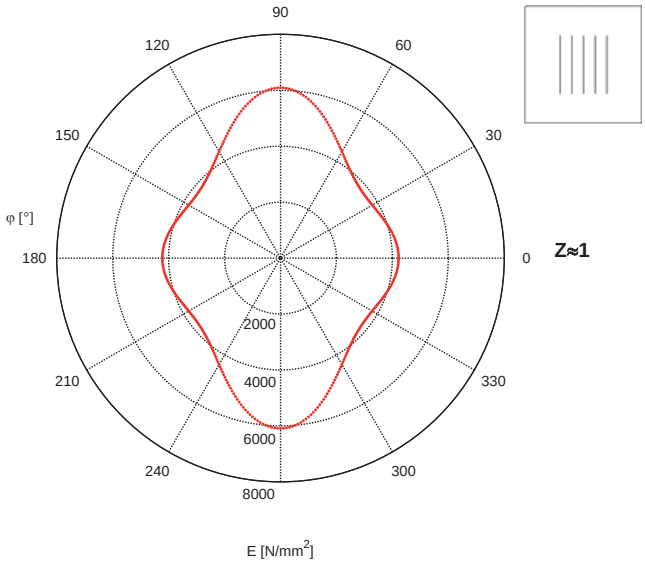

Figure 3.28: $E^*(\varphi)$ for a matrix with five vertically embedded fibers

In the next examples, see Figure 3.30, five diagonally embedded fibers are considered. The effective elasticity matrix for both possible diagonal fiber orientations results in

$$\boldsymbol{C}^*_{\text{diag}} = \begin{bmatrix} 5601.89 & 3161.89 & 0 \\ 3161.89 & 5601.89 & 0 \\ 0 & 0 & 1535.22 \end{bmatrix} \left[\text{ N/mm}^2\right], \tag{3.111}$$

and the anisotropy ratio $Z = 1.26$. A comparison of this elasticity matrix to the elasticity matrix of the unreinforced matrix material yields an increase of stiffness

in all components. The largest increase is observed in the C^*_{33} component, which corresponds to the shear or respectively the fiber direction.

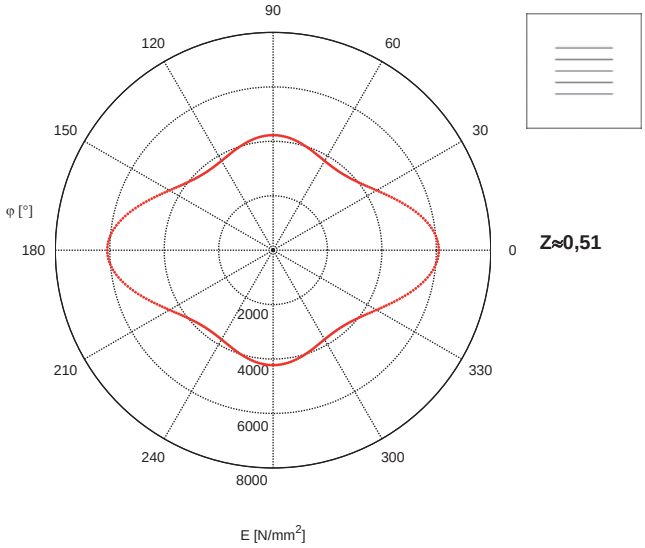

Figure 3.29: $E^*(\varphi)$ for a matrix with five horizontally embedded fibers

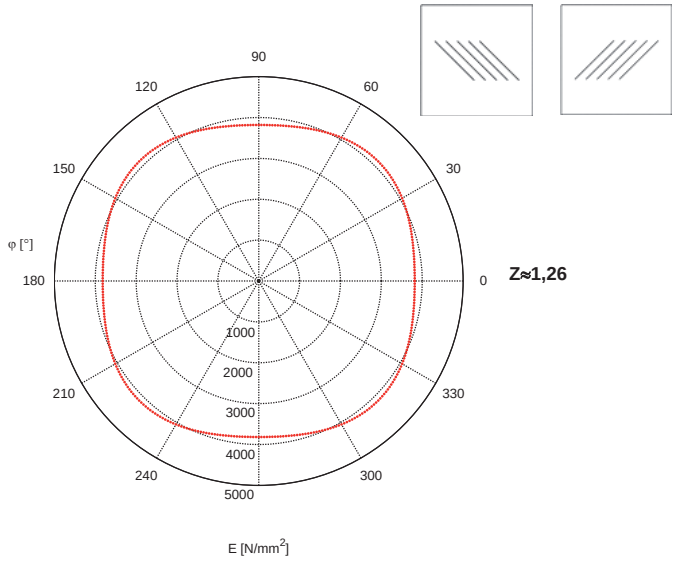

Figure 3.30: $E^*(\varphi)$ for a matrix with five diagonally embedded fibers

Please note, that although the elasticity matrix for both fiber directions given in Figure 3.30 is the same, the stresses result differently. In case of applied uniaxial tension loading, i.e., $\boldsymbol{\epsilon}^1_M$ and $\boldsymbol{\epsilon}^2_M$ are prescribed, the signs of the shear stresses change while in case of applied shear loading $\boldsymbol{\epsilon}^3_M$ the sign of the normal stresses change for

different fiber orientations. Figure 3.30 reveals that the maximal effective Young's modulus is given in diagonal direction, $E^*(45°) = 4135.7$ N/mm^2.

In the following examples the representativeness of RVEs is studied. Therefore, 10 realizations of RVEs with 50 randomly distributed fibers are generated. Also the fiber length is distributed randomly in such a way that the fiber length is between 0.25 and 0.5 of the edge size of the RVE. Figure 3.31 displays the error bars and the averages of the components of the elasticity matrices and the anisotropy ratio for the simulated specimens. The average of the elasticity matrix is given by

$$\boldsymbol{C}^*_{\text{rand1}} = \begin{bmatrix} 9490.66 & 4099.77 & 0 \\ 4099.77 & 9490.08 & 0 \\ 0 & 0 & 2005.33 \end{bmatrix} \left[\text{ N/mm}^2\right]. \tag{3.112}$$

A comparison of this elasticity matrix to the elasticity matrix of the pure matrix material (3.108) yields an increase of stiffness in all directions. The maximal increase is observed in the C^*_{11} and C^*_{22} components, which are almost equal, and also possess the largest deviations, see the error bars in Figure 3.31.

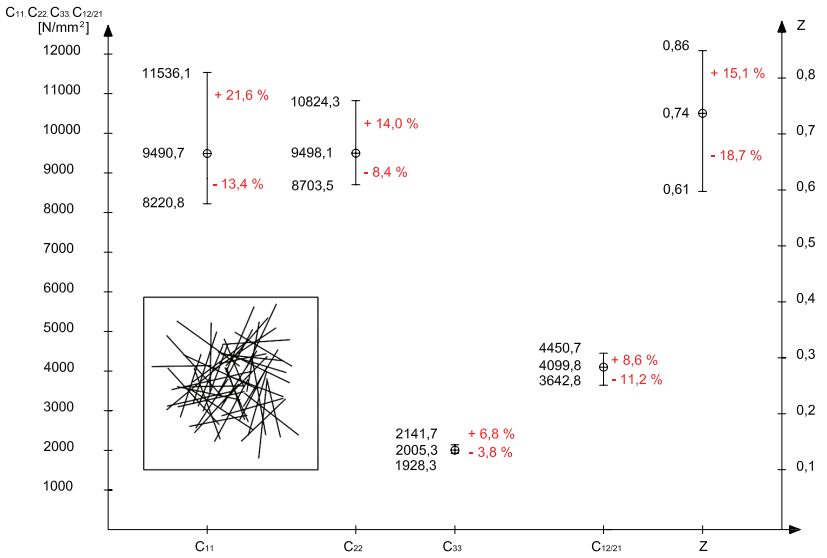

Figure 3.31: Averages and error bars for matrices with 50 randomly distributed fibers

Due to this larger increase of these normal directions, the anisotropy ratio does not equal 1. The anisotropy of the matrices with the randomly distributed fibers is also monitored in the averaged Young's modulus subject to the rotation angle, see Figure 3.32.

In the last example also 50 fibers have been embedded randomly into 10 different RVEs but the fiber direction has been restricted to $\pm 10°$ degrees around the horizontal axis of the RVE. Such a distribution of fibers plays an important role in the

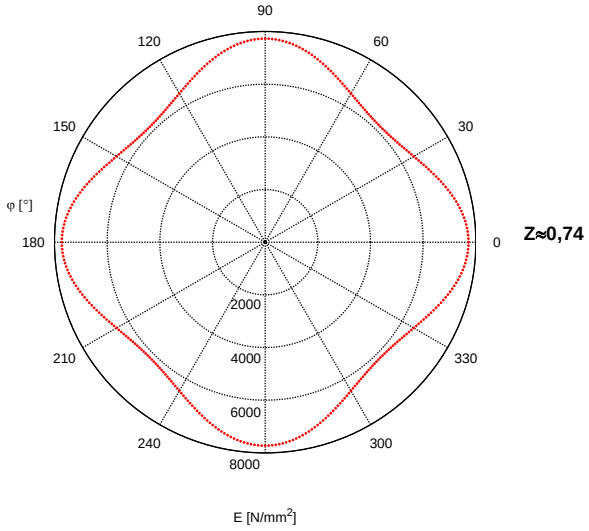

Figure 3.32: Averaged $E^*(\varphi)$ for matrices with 50 randomly distributed fibers

fabrication of devices within a casting process, where the fibers align in the direction of the injector. The fiber length again is generated between 0.25 and 0.5 the edge length of the RVE. Then, the averaged effective elasticity matrix is given by

$$\boldsymbol{C}^*_{\text{rand2}} = \begin{bmatrix} 13264.12 & 2882.18 & 0 \\ 2882.18 & 5289.11 & 0 \\ 0 & 0 & 1359.20 \end{bmatrix} \left[\text{N/mm}^2 \right], \tag{3.113}$$

while the averaged anisotropy ratio results in $Z = 0.26$. In contrast to the previous example with unrestricted fiber orientation, here the C^*_{11} component increases significantly, due to the prescribed fiber orientation, whereas the other components of the elasticity matrix almost equal the components of the matrix of the pure matrix material. The corresponding error bars are displayed in Figure 3.33.

Due to the fact that the fibers are mostly aligned in horizontal direction, only big deviations around the average are observed in the C^*_{11} component. This fiber alignment also is responsible for the rather big anisotropy which is reflected by the small anisotropy ratio and the elongated shape of the Young's modulus with respect to the rotation angle, see Figure 3.34.

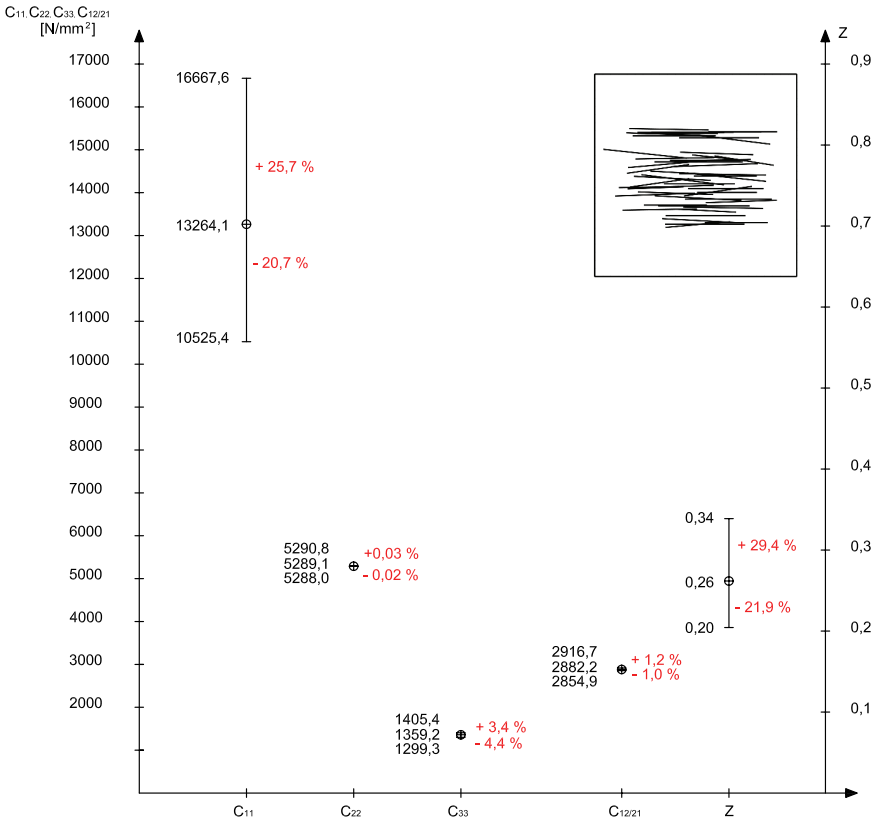

Figure 3.33: Averages and error bars for matrices with 50 distributed fibers in ±10° direction

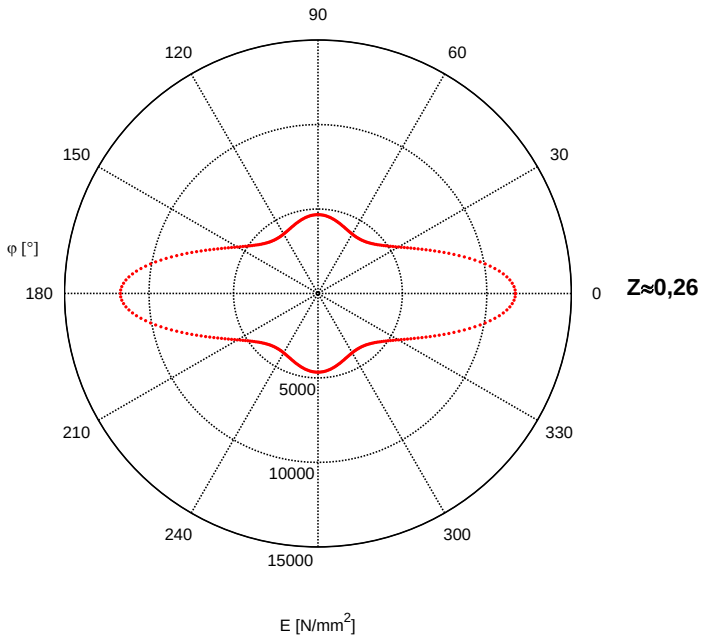

Figure 3.34: Averaged $E^*(\varphi)$ for matrices with 50 distributed fibers in ±10° direction

3.5 Summary

In the section at hand, an overview on the computational homogenization has been given. Averaged quantities have been defined and boundary conditions have been developed for the deformation- and the stress-driven homogenization scheme. Furthermore, the energy consistency of these boundary conditions has been checked in terms of the Hill-Mandel condition which states the equivalence between the macroscopic virtual work and the average of the microscopic virtual work. Additionally, the implementation of the the three types of boundary conditions within the FE^2 framework has been outlined. The concept of the computational homogenization for the spatial motion problems has been illustrated by various numerical examples. It has been studied, in which manner the different boundary conditions influence the macroscopic material response and which changes in the microscopic setting affect the macro-structure. In this context changes of the microscopic characteristics like the size, the shape and the orientation of voids contained in the micro-structure, have been compared. Furthermore, an effective approach for the simulation of fiber-reinforced matrices has been elaborated by application of embedded truss elements. Within this approach effective stiffnesses of RVE have been determined, and the deviation of effective properties has been studied for randomly distributed fibers. By plotting the Young's modulus depending on the direction and defining the anisotropy ratio elucidating depictions of the directional dependence of the stiffness of fiber-reinforced micro-structures have been given. Recapitulary, it has been shown that the computational homogenization scheme provides a powerful tool for the numerical simulation of micro-structured materials.

4 Computational Homogenization of Material Quantities

In this section the computational homogenization scheme is extended towards the homogenization of material variables at finite deformation. Part of this chapter has been previously published in Ricker et al. [72] and Ricker et al. [73]. In analogy to the spatial homogenization the occurrence of volume forces on the micro-level is taken into account. These configurational (or material) volume forces may occur due to inhomogeneities in the material. The main goal of the extension of the computational homogenization scheme towards the homogenization of material variables is the determination of the homogenized Eshelby stress tensor. With the help of the homogenized Eshelby stress tensor it is possible to determine macroscopic configurational node point forces depending on the underlying microscopic structure. These node point forces represent defect driving forces, e.g., the configurational force at a crack tip corresponds to the J-integral introduced by Rice in [70]. Thus, the magnitude of the configurational crack tip force yields a criterion whether a crack propagates depending on the underlying microscopic structure. Furthermore, the path-independence of the J-integral yields conservation laws with practical relevance in the field of asymptotic analysis of geometrically induced singular stress concentrations, see the work of Knowles and Sternberg [47]. More details concerning the material motion problem and its application to fracture mechanics can be found, e.g., in the textbooks by Maugin [55], Gurtin [29] and Kienzler and Herrmann [45]. In the work of Steinmann [82] the application of configurational forces to fracture mechanics in the geometrically non-linear case is elaborated, the algorithmic treatment of this concept is illustrated in Steinmann et al. [83]. Furthermore, an approach towards the implementation of material forces into the finite element method is presented by Müller et al. [63]. A numerical method for the computation of the J-integral based on the material forces method is given by Denzer et al. [12].

4.1 Averaged Material Variables

In analogy to the homogenization of spatial quantities, the homogenized material variables are established as appropriate averages over the micro-domain, see Figure 4.1 for the microscopic setting.
In analogy to the spatial motion problem, the average of the material deformation

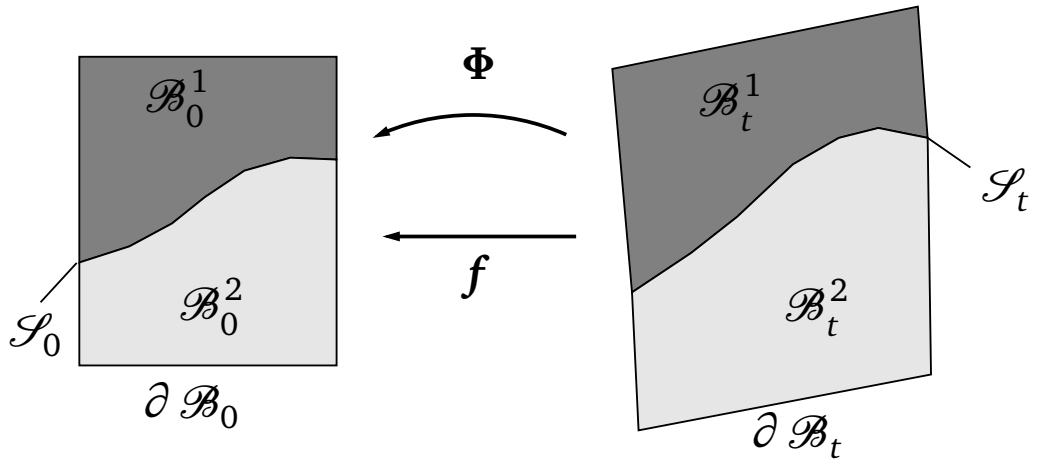

Figure 4.1: Microscopic material motion problem

gradient is defined in terms of the boundary as

$$\bar{\boldsymbol{f}} := \frac{1}{V_t} \int\limits_{\partial\mathscr{B}_t} \boldsymbol{\Phi} \otimes \boldsymbol{n} \, \mathrm{d}a = \frac{1}{V_t} \int\limits_{\mathscr{B}_t} \boldsymbol{f} \, \mathrm{d}v. \tag{4.1}$$

In the case of volume elements which contain discontinuities in the inverse map $\boldsymbol{\Phi}$, like holes or cracks, integrals over the boundary of the discontinuous domain $\partial\mathscr{H}_t$ need to be taken into account, additionally, i.e., it holds

$$\bar{\boldsymbol{f}} := \frac{1}{V_t} \int\limits_{\partial\mathscr{B}_t} \boldsymbol{\Phi} \otimes \boldsymbol{n} \, \mathrm{d}a = \frac{1}{V_t} \int\limits_{\mathscr{B}_t \setminus \mathscr{H}_t} \boldsymbol{f} \, \mathrm{d}v - \frac{1}{V_t} \int\limits_{\partial\mathscr{H}_t} \boldsymbol{\Phi} \otimes \boldsymbol{n} \, \mathrm{d}a. \tag{4.2}$$

In analogy to the averaged Cauchy stress, the averaged Eshelby stress is defined in terms of the dyadic product of the configurational traction vector $\boldsymbol{T}_0$ and the material position vector $\boldsymbol{\Phi}$:

$$\bar{\boldsymbol{\Sigma}} := \frac{1}{V_0} \left[\int\limits_{\partial\mathscr{B}_0} \boldsymbol{T}_0 \otimes \boldsymbol{\Phi} \, \mathrm{d}A + \int\limits_{\mathscr{S}_0} \boldsymbol{T}_0^s \otimes \boldsymbol{\Phi} \, \mathrm{d}A \right] = \frac{1}{V_0} \int\limits_{\mathscr{B}_0} \left[\boldsymbol{\Sigma} - \boldsymbol{B}_0 \otimes \boldsymbol{\Phi} \right] \mathrm{d}V. \tag{4.3}$$

In contrast to the spatial formulation, the interface integral needs to be incorporated in the definition of the averaged Eshelby stress due to the fact that the configurational tractions on opposite sides of the interface are not in equilibrium. Consequently, the Eshelby tractions at the interface are defined as

$$\boldsymbol{T}_0^s = (\boldsymbol{T}_0)_1 + (\boldsymbol{T}_0)_2 = \boldsymbol{\Sigma}_1 \cdot \boldsymbol{N}_1 + \boldsymbol{\Sigma}_2 \cdot \boldsymbol{N}_2 = [\![\boldsymbol{\Sigma}]\!] \cdot \boldsymbol{N}. \tag{4.4}$$

Therein, $\boldsymbol{N}_1$ and $\boldsymbol{N}_2$ denote the outward unit normals at different sides of the interface. Thus, with $\boldsymbol{N}_2 = -\boldsymbol{N}_1 := \boldsymbol{N}$ the jump operator results in $[\![\bullet]\!] := (\bullet)_2 - (\bullet)_1$.

Remark 3 *The incorporation of the interface terms into the calculation of the averaged Eshelby stress is motivated by means of a one-dimensional example. In Figure 4.2 a bar, which consists of two different materials, under uniaxial tension is depicted. Due to the equilibrium ,it holds that* $\sigma_1 = \sigma_2 = \sigma$. *The Eshelby stress is piecewise*

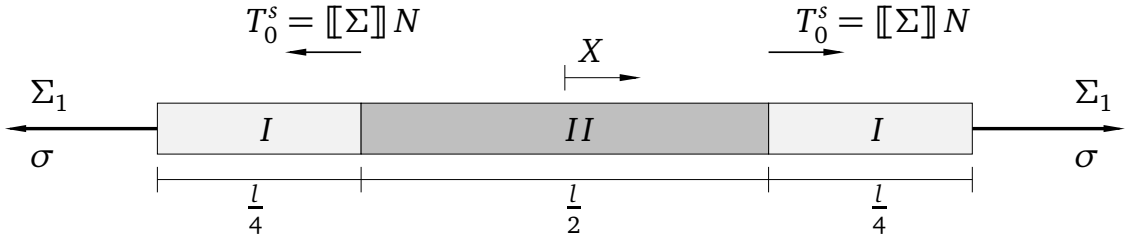

Figure 4.2: One-dimensional bar consisting of two different materials

constant in the three parts of the bar due to the different material properties and shows jumps at the interfaces. The averaged Eshelby tensor reads $\bar{\Sigma} = \frac{1}{2}\left[\Sigma_1 + \Sigma_2\right]$, *which can be easily verified by evaluating the volume integral in (4.3). An evaluation of the boundary integral in this equation should provide the same homogenized Eshelby stress. Obviously, this can only be obtained by considering also the interfacial tractions* T_0^s *and consequently the interfacial integrals within the homogenization*

$$\begin{aligned} \bar{\Sigma} &= \frac{1}{l}\left[[-\Sigma_1]\,[-\frac{l}{2}] + \Sigma_1\,\frac{l}{2} + [\Sigma_1 - \Sigma_2][-\frac{l}{4}] + [\Sigma_2 - \Sigma_1]\,\frac{l}{4}\right] \\ &= \frac{1}{2}\left[\Sigma_1 + \Sigma_2\right]. \end{aligned} \tag{4.5}$$

Thus, it has been demonstrated that the interfaces have to be incorporated into the calculation of the averaged Eshelby stress. Otherwise the way the RVE is cut out from the geometrically periodic micro-structure influences the homogenized Eshelby stress.

The formulation of the averaged Eshelby stress tensor in terms of a volume integral can further be reduced by application of the connection between the spatial and material volume forces

$$\boldsymbol{B}_0 = -\frac{\partial U_0}{\partial \boldsymbol{X}}|_{\text{expl.}} - \boldsymbol{F}^t \cdot \boldsymbol{b}_0, \tag{4.6}$$

see Appendix A for details. Due to the vanishing spatial body forces, which is a consequence of the requested periodicity –compare equation (3.23)–, the averaged Eshelby stress tensor reads

$$\bar{\boldsymbol{\Sigma}} = \frac{1}{V_0}\int_{\mathscr{B}_0}\left[\boldsymbol{\Sigma} + \frac{\partial U_0}{\partial \boldsymbol{X}}|_{\text{expl.}} \otimes \boldsymbol{\Phi}\right] \mathrm{d}V. \tag{4.7}$$

For non-graded materials, i.e., materials, for which the energy density is piecewise constant, the explicit derivative vanishes, and thus the Eshelby stress simplifies to

the volume average over its microscopic counterpart

$$\bar{\boldsymbol{\Sigma}} = \frac{1}{V_0} \int_{\mathscr{B}_0} \boldsymbol{\Sigma} \, \mathrm{d}V. \tag{4.8}$$

Furthermore, the averaged material two-point stress is defined in terms of the spatial boundary integral as

$$\bar{\boldsymbol{p}} = \frac{1}{V_t} \left[\int_{\partial \mathscr{B}_t} \boldsymbol{T}_t \otimes \boldsymbol{x} \, \mathrm{d}a + \int_{\mathscr{S}_t} \boldsymbol{T}_t^s \otimes \boldsymbol{x} \, \mathrm{d}a \right] = \frac{1}{V_t} \int_{\mathscr{B}_t} \left[\boldsymbol{p} - \boldsymbol{B}_t \otimes \boldsymbol{x} \right] \, \mathrm{d}v. \tag{4.9}$$

With the the same arguments as given above for the Eshelby stress, the volume integral formulation of the material two-point stress results in

$$\bar{\boldsymbol{p}} = \frac{1}{V_t} \int_{\mathscr{B}_t} \left[\boldsymbol{p} + \left[\boldsymbol{F}^t \cdot \frac{\partial U_t}{\partial \boldsymbol{x}} |_{\text{expl.}} \right] \otimes \boldsymbol{x} \right] \, \mathrm{d}v, \tag{4.10}$$

which for non-graded materials reduces to

$$\bar{\boldsymbol{p}} = \frac{1}{V_t} \int_{\mathscr{B}_t} \boldsymbol{p} \, \mathrm{d}v. \tag{4.11}$$

4.2 Material Scale-Transition

In the current subsection, the scale-transition for the material motion problem is developed based on its spatial counterpart. Due to the fact that in the spatial motion problem it has been shown that uniform traction boundary conditions yield very soft material responses, focus is only put onto the deformation-driven boundary conditions, i.e., displacement and periodic boundary conditions. The micro- and the macro-level are connected in a consistent manner via the microscopic material deformation map, which is constructed via a pull-back of the microscopic spatial deformation map (3.8) as

$$\boldsymbol{X} = -\boldsymbol{f}_M \cdot \boldsymbol{\varphi}_M + \boldsymbol{f}_M \cdot \boldsymbol{x} - \boldsymbol{f}_M \cdot \boldsymbol{w}(\boldsymbol{\Phi}^{-1}(\boldsymbol{x})), \tag{4.12}$$

whereby the macroscopic material deformation gradient is given as $\boldsymbol{f}_M = \boldsymbol{F}_M^{-1}$. In order to rearrange the material deformation map in a similar format as the spatial deformation map, that is

$$\boldsymbol{X} = \boldsymbol{\Phi}(\boldsymbol{x}) := \boldsymbol{\Phi}_M + \boldsymbol{f}_M \cdot \boldsymbol{x} + \boldsymbol{W}(\boldsymbol{x}), \tag{4.13}$$

the constant macroscopic part and the material fluctuations need to be defined as

$$\boldsymbol{\Phi}_M := -\boldsymbol{f}_M \cdot \boldsymbol{\varphi}_M \quad \text{and} \quad \boldsymbol{W} := -\boldsymbol{f}_M \cdot \boldsymbol{w}. \tag{4.14}$$

The variation of this material deformation map at fixed spatial coordinates $\boldsymbol{x}$ is then given by

$$\mathrm{d}_\delta \boldsymbol{\Phi} = -\mathrm{d}_\delta \boldsymbol{f}_M \cdot \boldsymbol{\varphi}_M + \mathrm{d}_\delta \boldsymbol{f}_M \cdot \boldsymbol{x} - \mathrm{d}_\delta \boldsymbol{f}_M \cdot \boldsymbol{w}, \tag{4.15}$$

which results by application of the spatial scale-transition in

$$\mathrm{d}_\delta \boldsymbol{\Phi} = \mathrm{d}_\delta \boldsymbol{f}_M \cdot \boldsymbol{F}_M \cdot \boldsymbol{X}. \tag{4.16}$$

In a next step, the average strain theorem for the material motion problem is developed based on the boundary conditions applied to the spatial fluctuations. Therefore, the material scale-transition (4.12) is inserted into the definition of the averaged material deformation gradient (4.1), which yields

$$\begin{aligned} \bar{\boldsymbol{f}} &= \frac{1}{V_t} \int_{\partial \mathscr{B}_t} \left[\boldsymbol{f}_M \cdot \left[-\boldsymbol{\varphi}_M + \boldsymbol{x} - \boldsymbol{w} \right] \right] \otimes \boldsymbol{n} \, \mathrm{d}a \\ &= \frac{1}{V_t} \boldsymbol{f}_M \cdot \left[\int_{\partial \mathscr{B}_t} -\boldsymbol{\varphi}_M \otimes \boldsymbol{n} \, \mathrm{d}a + \int_{\partial \mathscr{B}_t} \boldsymbol{x} \otimes \boldsymbol{n} \, \mathrm{d}a - \int_{\partial \mathscr{B}_t} \boldsymbol{w} \otimes \boldsymbol{n} \, \mathrm{d}a \right]. \end{aligned} \tag{4.17}$$

In this equation, the first integrand vanishes due to $\boldsymbol{\varphi}_M = \text{const.}$ and the last integrand vanishes due to the displacement or periodic boundary conditions, i.e., $\boldsymbol{w} = \boldsymbol{0}$ or $\boldsymbol{w}^+ = \boldsymbol{w}^-$. Application of the auxiliary result

$$\int_{\partial \mathscr{B}_t} \boldsymbol{x} \otimes \boldsymbol{n} \, \mathrm{d}a = \int_{\mathscr{B}_t} \mathrm{grad}\boldsymbol{x} \, \mathrm{d}v = \int_{\mathscr{B}_t} \boldsymbol{I} \, \mathrm{d}v = V_t, \tag{4.18}$$

then finally yields the desired result

$$\bar{\boldsymbol{f}} = \frac{1}{V_t} \boldsymbol{f}_M \, V_t = \boldsymbol{f}_M. \tag{4.19}$$

Thus, it has been shown that in case of consistent boundary conditions the average strain theorem is also valid for the material deformation gradient. The proof concerning the uniform traction boundary conditions can be found in the work of Costanzo et al. [11].

After introducing the material scale-transition and the average strain theorem for the inverse deformation gradient tensor in the following different approaches for the determination of the macroscopic stresses are developed based on averaged spatial variables, and the definitions of the averaged Eshelby stress (4.3) and material stress (4.9). For the material homogenization procedure developed here, a

homogeneous macro-continuum is assumed, i.e., a macro-continuum is considered for which the same RVE is attached at all material points. Therefore, the explicit derivative of the macroscopic energy density with respect to the macroscopic material coordinates vanishes, that is

$$\frac{\partial U_{0M}}{\partial \boldsymbol{X}_M}|_{\text{expl.}} = \boldsymbol{0}. \tag{4.20}$$

Furthermore, it is assumed that the spatial Hill-Mandel condition is valid, which together with the assumption of a macro-homogeneous continuum yields that there exists a macroscopic energy density function such that

$$\boldsymbol{P}_M = \frac{\partial U_{0M}}{\partial \boldsymbol{F}_M}, \tag{4.21}$$

is valid, see e.g., the work of Miehe [57].

With assistance of these assumptions, in the next sections different approaches to determine macroscopic material stresses are discussed and compared, based on a material formulation of a Hill-Mandel type condition.

Firstly, the most intuitive approach is discussed, for which the macroscopic material stress is determined by means of macroscopic spatial quantities.

4.2.1 Homogenized Material Stresses based on Macroscopic Spatial Variables

As a first approach to determine the macroscopic material stresses based on the underlying micro-structure, the required macroscopic Eshelby stress is defined in terms of macroscopic spatial quantities according to (2.30) as

$$\boldsymbol{\Sigma}^*_M := U_{0M}\, \boldsymbol{I} - \boldsymbol{F}^t_M \cdot \boldsymbol{P}_M. \tag{4.22}$$

Preliminary, it is assumed that the microscopic material is non-graded, i.e., the stored energy density does not depend explicitly on the material or the spatial coordinates, respectively. The more general case of graded materials is considered later, see Remark 5. The macroscopic configurational volume force per undeformed unit volume is calculated in terms of the macroscopic Eshelby stress via

$$\boldsymbol{B}^*_{0M} = -\text{Div}\boldsymbol{\Sigma}^*_M. \tag{4.23}$$

By application of the definition of $\boldsymbol{\Sigma}$ and the calculation as given in Appendix A this configurational volume force can be connected with the spatial volume force via

$$\boldsymbol{B}^*_{0M} = -\frac{\partial U_{0M}}{\partial \boldsymbol{X}_M}|_{\text{expl.}} - \boldsymbol{F}^t_M \cdot \boldsymbol{b}_{0M}. \tag{4.24}$$

This equation can be further reduced due to the fact that in Section 3.2.1 it already has been shown that the macroscopic spatial body forces b_{0M} are zero, see equation (3.33), and thus the last term of (4.24) vanishes. Furthermore, it already has been claimed that a macro-homogeneous continuum is considered, i.e., $\frac{\partial U_{0M}}{\partial \boldsymbol{X}_M}|_{\text{expl.}} = \boldsymbol{0}$ and thus it holds

$$\boldsymbol{B}^*_{0M} = -\text{Div}\boldsymbol{\Sigma}^*_M = \boldsymbol{0}. \tag{4.25}$$

Next focus is put onto the connection between the macroscopic Eshelby stress tensor $\boldsymbol{\Sigma}^*_M$ as defined in equation (4.22) and its averaged counterpart $\bar{\boldsymbol{\Sigma}}$, see equation (4.3). Therefore, the macroscopic energy density U_{0M} is expressed through microscopic quantities via the volume averaging

$$U_{0M} = \frac{1}{V_0}\int_{\mathscr{B}_0} U_0 \, \mathrm{d}V. \tag{4.26}$$

Application of this formulation of the macroscopic energy to the definition of $\boldsymbol{\Sigma}^*_M$ yields

$$\boldsymbol{\Sigma}^*_M = \frac{1}{V_0}\int_{\mathscr{B}_0} U_0 \boldsymbol{I} \, \mathrm{d}V - \boldsymbol{F}^t_M \cdot \boldsymbol{P}_M. \tag{4.27}$$

In the first instance, the equivalence between the macroscopic and the averaged Piola stress (3.33) is exploited, then $\boldsymbol{F}^t_M$ is substituted by means of the spatial scale-transition (3.9) which yields

$$\begin{aligned}
\boldsymbol{\Sigma}^*_M &= \frac{1}{V_0}\int_{\mathscr{B}_0} \left[U_0 \boldsymbol{I} - \boldsymbol{F}^t_M \cdot \boldsymbol{P}\right] \mathrm{d}V \\
&= \frac{1}{V_0}\left[\int_{\mathscr{B}_0} \left[U_0 \boldsymbol{I} - \boldsymbol{F}^t \cdot \boldsymbol{P} + (\nabla_{\boldsymbol{X}} \boldsymbol{w})^t \cdot \boldsymbol{P}\right] \mathrm{d}V\right] \\
&= \frac{1}{V_0}\int_{\mathscr{B}_0} \boldsymbol{\Sigma} \, \mathrm{d}V + \frac{1}{V_0}\int_{\mathscr{B}_0} (\nabla_{\boldsymbol{X}} \boldsymbol{w})^t \cdot \boldsymbol{P} \, \mathrm{d}V.
\end{aligned} \tag{4.28}$$

Thus, the following relation between the macroscopic and the averaged Eshelby stress holds

$$\boldsymbol{\Sigma}^*_M = \bar{\boldsymbol{\Sigma}} + \frac{1}{V_0}\int_{\mathscr{B}_0} (\nabla_{\boldsymbol{X}} \boldsymbol{w})^t \cdot \boldsymbol{P} \, \mathrm{d}V. \tag{4.29}$$

Remark 4 *By assistance of a numerical example, it is illustrated that the extra term in* (4.29) *is not vanishing in general. Therefore, an inhomogeneous micro-structure*

containing a non-centered void under periodic boundary conditions is considered, see Figure 4.3 for the undeformed and the deformed setting. The RVE is deformed by the following prescribed macroscopic deformation gradient

$$\boldsymbol{F}_M = \begin{bmatrix} 1.00 & 0.15 \\ 0.15 & 1.10 \end{bmatrix}, \tag{4.30}$$

and a Neo-Hookean type material is assumed.

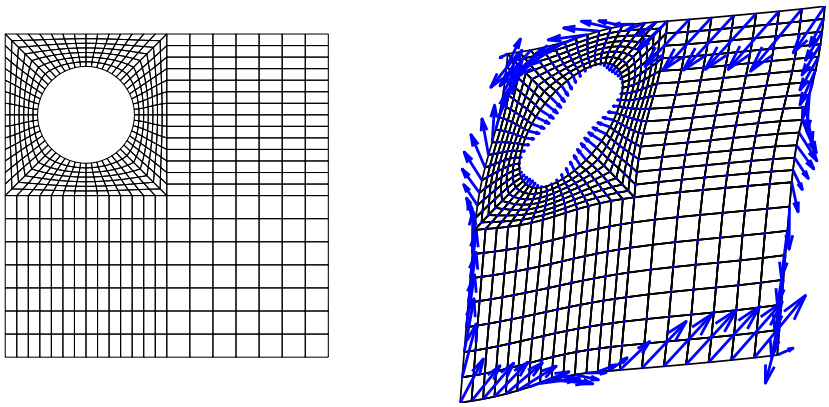

Figure 4.3: Undeformed and deformed microscopic RVE under periodic boundary conditions and resulting material nodal forces

Then, the Eshelby stress tensor determined by means of averaged spatial quantities and the averaged Eshelby stress tensor reads

$$\begin{aligned} \boldsymbol{\Sigma}_M^* &= \begin{bmatrix} -13.58 & -167.11 \\ -166.21 & -127.93 \end{bmatrix} [N/mm^2] \quad \textit{and} \\ \bar{\boldsymbol{\Sigma}} &= \begin{bmatrix} -28.09 & -180.80 \\ -180.80 & -146.48 \end{bmatrix} [N/mm^2], \end{aligned} \tag{4.31}$$

and thus the last term in (4.29) *can be identified as*

$$\frac{1}{V_0} \int_{\mathscr{B}_0} (\nabla_{\boldsymbol{X}} \boldsymbol{w})^t \cdot \boldsymbol{P} \, \mathrm{d}V = \begin{bmatrix} 14.51 & 13.69 \\ 14.60 & 18.55 \end{bmatrix} [N/mm^2]. \tag{4.32}$$

Please note, that in case of an homogeneous micro-structure $\boldsymbol{\Sigma}_M^*$ and $\bar{\boldsymbol{\Sigma}}$ are equivalent.

In a next step, focus is put onto the macroscopic and the averaged virtual work in order to develop a Hill-Mandel type condition in terms of material quantities. Therefore, the macroscopic Eshelby stress calculated by means of (4.22) is inserted into the variation of the macroscopic work (at fixed spatial coordinates $\boldsymbol{x}$)

$$p_{0M}^* = J_M \mathrm{d}_\delta U_{tM} = \left[\mathrm{d}_\delta \boldsymbol{f}_M \cdot \boldsymbol{F}_M \right] : \boldsymbol{\Sigma}_M^*. \tag{4.33}$$

Thereby, according to (2.21) the macroscopic energy density U_{tM} is calculated by

$$U_{tM} = j_M \, U_{0M} = \frac{1}{V_t} \int_{\mathscr{B}_t} U_t \, \mathrm{d}v. \tag{4.34}$$

With assistance of relation (4.29) and the definition of the averaged Eshelby stress (4.3), the variation of work can be recasted to

$$\begin{aligned} p^*_{0M} &= \left[\mathrm{d}_\delta \boldsymbol{f}_M \cdot \boldsymbol{F}_M\right] : \bar{\boldsymbol{\Sigma}} + \left[\mathrm{d}_\delta \boldsymbol{f}_M \cdot \boldsymbol{F}_M\right] : \frac{1}{V_0} \int_{\mathscr{B}_0} (\boldsymbol{\nabla}_{\boldsymbol{X}} \boldsymbol{w})^t \cdot \boldsymbol{P} \, \mathrm{d}V \\ &= \left[\mathrm{d}_\delta \boldsymbol{f}_M \cdot \boldsymbol{F}_M\right] : \frac{1}{V_0} \left[\int_{\partial \mathscr{B}_0} \boldsymbol{T}_0 \otimes \boldsymbol{\Phi} \, \mathrm{d}A + \int_{\mathscr{S}_0} \boldsymbol{T}^s_0 \otimes \boldsymbol{\Phi} \, \mathrm{d}A \right] \\ &+ \left[\mathrm{d}_\delta \boldsymbol{f}_M \cdot \boldsymbol{F}_M\right] : \frac{1}{V_0} \int_{\mathscr{B}_0} (\boldsymbol{\nabla}_{\boldsymbol{X}} \boldsymbol{w})^t \cdot \boldsymbol{P} \, \mathrm{d}V \\ &= \frac{1}{V_0} \left[\int_{\partial \mathscr{B}_0} \left[\mathrm{d}_\delta \boldsymbol{f}_M \cdot \boldsymbol{F}_M \cdot \boldsymbol{\Phi}\right] \cdot \boldsymbol{T}_0 \, \mathrm{d}A + \int_{\mathscr{S}_0} \left[\mathrm{d}_\delta \boldsymbol{f}_M \cdot \boldsymbol{F}_M \cdot \boldsymbol{\Phi}\right] \cdot \boldsymbol{T}^s_0 \, \mathrm{d}A \right] \\ &+ \left[\mathrm{d}_\delta \boldsymbol{f}_M \cdot \boldsymbol{F}_M\right] : \frac{1}{V_0} \int_{\mathscr{B}_0} (\boldsymbol{\nabla}_{\boldsymbol{X}} \boldsymbol{w})^t \cdot \boldsymbol{P} \, \mathrm{d}V. \end{aligned} \tag{4.35}$$

By application of the scale-transition (4.16) this equation is simplified to

$$\begin{aligned} p^*_{0M} &= \frac{1}{V_0} \left[\int_{\partial \mathscr{B}_0} \mathrm{d}_\delta \boldsymbol{\Phi} \otimes \boldsymbol{T}_0 \, \mathrm{d}A + \int_{\mathscr{S}_0} \mathrm{d}_\delta \boldsymbol{\Phi} \otimes \boldsymbol{T}^s_0 \, \mathrm{d}A \right] \\ &+ \left[\mathrm{d}_\delta \boldsymbol{f}_M \cdot \boldsymbol{F}_M\right] : \frac{1}{V_0} \int_{\mathscr{B}_0} (\boldsymbol{\nabla}_{\boldsymbol{X}} \boldsymbol{w})^t \cdot \boldsymbol{P} \, \mathrm{d}V. \end{aligned} \tag{4.36}$$

A comparison with the average of the variation of the microscopic (configurational) work,

$$\bar{p}_0 = \frac{1}{V_0} \left[\int_{\partial \mathscr{B}_0} \mathrm{d}_\delta \boldsymbol{\Phi} \cdot \boldsymbol{T}_0 \, \mathrm{d}A + \int_{\mathscr{S}_0} \mathrm{d}_\delta \boldsymbol{\Phi} \cdot \boldsymbol{T}^s_0 \, \mathrm{d}A \right], \tag{4.37}$$

yields the following format for the Hill-Mandel type condition

$$p^*_{0M} = \bar{p}_0 + \bar{p}^{*\,\mathrm{int}}_0, \tag{4.38}$$

whereby the additional internal contribution to the virtual work is given by

$$\bar{p}_0^{*\,\mathrm{int}} = \left[\mathrm{d}_\delta \boldsymbol{f}_M \cdot \boldsymbol{F}_M\right] : \frac{1}{V_0} \int_{\mathscr{B}_0} (\boldsymbol{\nabla}_{\boldsymbol{X}} \boldsymbol{w})^t \cdot \boldsymbol{P} \, \mathrm{d}V. \tag{4.39}$$

Analogously, the macroscopic material two-point stress can be defined in terms of homogenized macroscopic quantities

$$\boldsymbol{p}_M^* := U_{tM} \, \boldsymbol{F}_M^t - \boldsymbol{F}_M^t \cdot \boldsymbol{\sigma}_M. \tag{4.40}$$

By application of the definition of $\boldsymbol{\Sigma}_M^*$ and relation (3.29), which is a consequence of the spatial Hill-Mandel condition, it follows

$$\boldsymbol{p}_M^* = j_M \, \boldsymbol{\Sigma}_M^* \cdot \boldsymbol{F}_M^t. \tag{4.41}$$

Thus, the standard pull-back operation is valid between the homogenized material stress measures $\boldsymbol{p}_M^*$ and $\boldsymbol{\Sigma}_M^*$. Furthermore, it can be shown that the following relation between the macroscopic and the averaged two-point stress holds in case of a non-graded micro-material

$$\boldsymbol{p}_M^* = \bar{\boldsymbol{p}} - \frac{1}{V_t} \int_{\mathscr{B}_t} \left[\boldsymbol{F}^t \cdot \left(\nabla_{\boldsymbol{x}} \boldsymbol{w}\right)^t \cdot \boldsymbol{f}^t\right] \cdot \boldsymbol{p} \, \mathrm{d}v. \tag{4.42}$$

Based on this formulation of the macroscopic two-point stress, focus is put onto the macroscopic and the averaged virtual work to develop an adequate Hill-Mandel type condition. The macroscopic virtual work in terms of $\boldsymbol{p}_M^*$ is given by

$$p_{tM}^* = \mathrm{d}_\delta U_{tM} = \mathrm{d}_\delta \boldsymbol{f}_M : \boldsymbol{p}_M^* = \mathrm{d}_\delta \boldsymbol{f}_M : \bar{\boldsymbol{p}} - \mathrm{d}_\delta \boldsymbol{f}_M : \frac{1}{V_t} \int_{\mathscr{B}_t} \left[\boldsymbol{F}^t \cdot \left(\nabla_{\boldsymbol{x}} \boldsymbol{w}\right)^t \cdot \boldsymbol{f}^t\right] \cdot \boldsymbol{p} \, \mathrm{d}v. \tag{4.43}$$

Therein, the contribution resulting from the macroscopic volume forces can be neglected due to the fact that it already has been shown in (4.25) that $\boldsymbol{B}_{0M}^* = \boldsymbol{0}$ and thus in case of the assumed macro-homogeneous continuum also $\boldsymbol{B}_{tM}^*$ vanishes. Insertion of the definition of the averaged material deformation gradient (4.9) and the material scale-transition yields the following Hill-Mandel type condition

$$p_{tM}^* = \bar{p}_t + \bar{p}_t^{*\,\mathrm{int}}, \tag{4.44}$$

whereby the averaged virtual work is given by

$$\bar{p}_t = \frac{1}{V_t} \left[\int_{\partial \mathscr{B}_t} \boldsymbol{T}_t \cdot \mathrm{d}_\delta \boldsymbol{\Phi} \, \mathrm{d}a + \int_{\mathscr{S}_t} \boldsymbol{T}_t^s \cdot \mathrm{d}_\delta \boldsymbol{\Phi} \, \mathrm{d}a \right], \tag{4.45}$$

and the additional internal contribution reads

$$\bar{p}_t^{*\,\mathrm{int}} = \mathrm{d}_\delta \boldsymbol{f}_M : \frac{1}{V_t} \int_{\mathscr{B}_t} \left[\boldsymbol{p} \cdot \left(\nabla_{\boldsymbol{x}} \boldsymbol{w} \right)^t - \left[\boldsymbol{F}^t \cdot \left(\nabla_{\boldsymbol{x}} \boldsymbol{w} \right)^t \cdot \boldsymbol{f}^t \right] \cdot \boldsymbol{p} \right] \, \mathrm{d}v. \tag{4.46}$$

Due to these extra contributions, which emerge in the material Hill-Mandel type conditions formulated in $\boldsymbol{\Sigma}_M^*$ and $\boldsymbol{p}_M^*$, it is not adequate to determine homogenized material forces based on material stress measures, which depend exclusively on homogenized spatial quantities. Thus, in the following subsections further approaches for the determination of material stresses are developed, which ensure consistent Hill-Mandel type conditions without the necessity of internal contributions.

Remark 5 *In the case of a graded microscopic material, extra terms, which depend on the explicit derivative of the stored energy density with respect to the material or spatial coordinates, have to be taken into account. The relation between the macroscopic and the averaged Eshelby stress then reads*

$$\boldsymbol{\Sigma}_M^* = \bar{\boldsymbol{\Sigma}} + \frac{1}{V_0} \int_{\mathscr{B}_0} \left[(\nabla_{\boldsymbol{X}} \boldsymbol{w})^t \cdot \boldsymbol{P} - \frac{\partial U_0}{\partial \boldsymbol{X}}|_{expl.} \otimes \boldsymbol{X} \right] \, \mathrm{d}V. \tag{4.47}$$

Likewise, the internal extra contribution in the material Hill-Mandel type condition, compare equation (4.39)*, contains an additional term depending on the explicit derivative of the stored energy and thus for graded materials it holds*

$$\bar{p}_0^{*\,int} = \left[d_\delta \boldsymbol{f}_M : \boldsymbol{F}_M \right] : \frac{1}{V_0} \int_{\mathscr{B}_0} \left[(\nabla_{\boldsymbol{X}} \boldsymbol{w})^t \cdot \boldsymbol{P} - \frac{\partial U_0}{\partial \boldsymbol{X}}|_{expl.} \otimes \boldsymbol{\Phi} \right] \, \mathrm{d}V. \tag{4.48}$$

Furthermore, in analogy to the macroscopic Eshelby stress also the relation between the macroscopic and the averaged material two-point stress –see equation (4.42)*– needs to be updated for graded materials and then reads*

$$\boldsymbol{p}_M^* = \bar{\boldsymbol{p}} - \frac{1}{V_t} \int_{\mathscr{B}_t} \left[\left[\boldsymbol{F}^t \cdot \left(\nabla_{\boldsymbol{x}} \boldsymbol{w} \right)^t \cdot \boldsymbol{f}^t \right] \cdot \boldsymbol{p} + \left[\boldsymbol{F}^t \cdot \frac{\partial U_t}{\partial \boldsymbol{x}}|_{expl.} \right] \otimes \boldsymbol{X} \right] \, \mathrm{d}v. \tag{4.49}$$

Finally, the internal extra contribution to the material Hill-Mandel type condition formulated in terms of the material two-point stress is given by

$$\begin{aligned} \bar{p}_t^{*\,int} = d_\delta \boldsymbol{f}_M : \frac{1}{V_t} \int_{\mathscr{B}_t} & \left[\boldsymbol{p} \cdot (\nabla_{\boldsymbol{x}} \boldsymbol{w})^t - \left[\boldsymbol{F}^t \cdot \left(\nabla_{\boldsymbol{x}} \boldsymbol{w} \right)^t \cdot \boldsymbol{f}^t \right] \cdot \boldsymbol{p} \right. \\ & \left. - \left[\boldsymbol{F}^t \cdot \frac{\partial U_t}{\partial \boldsymbol{x}}|_{expl.} \right] \otimes \left[\boldsymbol{F}_M \cdot \boldsymbol{X} \right] \right] \, \mathrm{d}v. \end{aligned} \tag{4.50}$$

The detailed derivation of this contribution is given in Appendix C.1.

4.2.2 Homogenized Material Stresses based on the Averaged Eshelby Stress Tensor

In the following, another approach for the determination of homogenized material variables is elaborated. Instead of determining the homogenized variables in terms of homogenized spatial quantities, an averaging process is carried out. In the approach at hand, the starting point is the macroscopic Eshelby stress which is defined by means of the averaged Eshelby stress as

$$\boldsymbol{\Sigma}_M := \bar{\boldsymbol{\Sigma}} = \frac{1}{V_0}\left[\int\limits_{\partial\mathscr{B}_0} \boldsymbol{T}_0 \otimes \boldsymbol{\Phi}\,\mathrm{d}A + \int\limits_{\mathscr{S}_0} \boldsymbol{T}_0^s \otimes \boldsymbol{\Phi}\,\mathrm{d}A\right]. \tag{4.51}$$

For the present, only non-graded micro-materials are considered thus the explicit derivatives of the strain energy with respect to the position can be neglected. Later focus is put onto the more general case of graded materials, see Remark 6. Thus, for the non-graded material at hand, the macroscopic Eshelby stress results by application of (4.8) in

$$\boldsymbol{\Sigma}_M = \frac{1}{V_0}\int\limits_{\mathscr{B}_0} \boldsymbol{\Sigma}\,\mathrm{d}V. \tag{4.52}$$

In a next step, focus is put onto the corresponding macroscopic volume forces given as

$$\boldsymbol{B}_{0M} = -\mathrm{Div}\boldsymbol{\Sigma}_M, \tag{4.53}$$

which vanish due to vanishing spatial volume forces and a non-graded material, i.e.,

$$\boldsymbol{B}_{0M} = \boldsymbol{0}. \tag{4.54}$$

The macroscopic virtual work in terms of the regarded Eshelby stress reads

$$p_{0M} = J_M\ \mathrm{d}_\delta U_{tM} = \left[\mathrm{d}_\delta \boldsymbol{f}_M \cdot \boldsymbol{F}_M\right] : \boldsymbol{\Sigma}_M. \tag{4.55}$$

Application of the definition of the macroscopic Eshelby stress (4.51) yields

$$p_{0M} = \frac{1}{V_0}\left[\int\limits_{\partial\mathscr{B}_0} \boldsymbol{T}_0 \cdot \left[\mathrm{d}_\delta \boldsymbol{f}_M \cdot \boldsymbol{F}_M \cdot \boldsymbol{\Phi}\right]\,\mathrm{d}A + \int\limits_{\mathscr{S}_0} \boldsymbol{T}_0^s \cdot \left[\mathrm{d}_\delta \boldsymbol{f}_M \cdot \boldsymbol{F}_M \cdot \boldsymbol{\Phi}\right]\,\mathrm{d}A\right], \tag{4.56}$$

and with equation (4.16) the macroscopic virtual work results in

$$p_{0M} = \frac{1}{V_0}\left[\int\limits_{\partial\mathscr{B}_0} \boldsymbol{T}_0 \cdot \mathrm{d}_\delta \boldsymbol{\Phi}\,\mathrm{d}A + \int\limits_{\mathscr{S}_0} \boldsymbol{T}_0^s \cdot \mathrm{d}_\delta \boldsymbol{\Phi}\,\mathrm{d}A\right]. \tag{4.57}$$

Thus, the Hill-Mandel type condition formulated in $\boldsymbol{\Sigma}_M = \bar{\boldsymbol{\Sigma}}$ is given by

$$p_{0M} = \bar{p}_0. \tag{4.58}$$

Compared to the first approach based on averaged spatial quantities for the approach at hand, no internal extra contributions are necessary to formulate a consistent Hill-Mandel type condition for non-graded materials.

In a next step, the macroscopic two-point stress which corresponds to the macroscopic Eshelby stress as defined in (4.51) is elaborated based on

$$\begin{aligned} \boldsymbol{p}_M &:= j_M \, \boldsymbol{\Sigma}_M \cdot \boldsymbol{F}_M^t \\ &= \frac{V_0}{V_t} \frac{1}{V_0} \left[\int_{\partial \mathscr{B}_0} \boldsymbol{T}_0 \otimes \boldsymbol{\Phi} \, \mathrm{d}A + \int_{\mathscr{S}_0} \boldsymbol{T}_0^s \otimes \boldsymbol{\Phi} \, \mathrm{d}A \right] \cdot \boldsymbol{F}_M^t \\ &= \frac{1}{V_t} \left[\int_{\partial \mathscr{B}_0} \boldsymbol{T}_0 \otimes \left[\boldsymbol{F}_M \cdot \boldsymbol{\Phi} \right] \, \mathrm{d}A + \int_{\mathscr{S}_0} \boldsymbol{T}_0^s \otimes \left[\boldsymbol{F}_M \cdot \boldsymbol{\Phi} \right] \, \mathrm{d}A \right]. \end{aligned} \tag{4.59}$$

Application of the spatial scale-transition to substitute $\boldsymbol{F}_M \cdot \boldsymbol{\Phi}$ yields

$$\begin{aligned} \boldsymbol{p}_M = & \frac{1}{V_t} \left[\int_{\partial \mathscr{B}_0} \boldsymbol{T}_0 \otimes \boldsymbol{x} \, \mathrm{d}A + \int_{\mathscr{S}_0} \boldsymbol{T}_0^s \otimes \boldsymbol{x} \, \mathrm{d}A \right] \\ & - \frac{1}{V_t} \left[\int_{\partial \mathscr{B}_0} \boldsymbol{T}_0 \, \mathrm{d}A + \int_{\mathscr{S}_0} \boldsymbol{T}_0^s \, \mathrm{d}A \right] \otimes \boldsymbol{\varphi}_M \\ & - \frac{1}{V_t} \left[\int_{\partial \mathscr{B}_0} \boldsymbol{T}_0 \otimes \boldsymbol{w} \, \mathrm{d}A + \int_{\mathscr{S}_0} \boldsymbol{T}_0^s \otimes \boldsymbol{w} \, \mathrm{d}A \right]. \end{aligned} \tag{4.60}$$

Therein, the second term at the right-hand side vanishes due to the regarded non-graded material and the vanishing spatial volume forces. The first and the last term of the right-hand side of (4.60) can further be reformulated by integral manipulations, see Appendix B for details, especially equations (B.6) and (B.12). Thus, the macroscopic two-point stress of the approach at hand reads

$$\boldsymbol{p}_M = \bar{\boldsymbol{p}} - \bar{\boldsymbol{p}}^+, \tag{4.61}$$

with

$$\bar{\boldsymbol{p}}^+ = \frac{1}{V_t} \int_{\partial \mathscr{B}_t} \boldsymbol{p} \cdot \left(\nabla_{\boldsymbol{x}} \boldsymbol{w} \right)^t \, \mathrm{d}v. \tag{4.62}$$

The macroscopic volume forces connected to $\boldsymbol{p}_M$ are consequently derived via

$$\boldsymbol{B}_{tM} = -\operatorname{div} \boldsymbol{p}_M = -\operatorname{div} \bar{\boldsymbol{p}} + \operatorname{div} \bar{\boldsymbol{p}}^+. \tag{4.63}$$

In case of a non-graded micro-material $\operatorname{div} \bar{\boldsymbol{p}} = \boldsymbol{0}$ whereas

$$\operatorname{div} \bar{\boldsymbol{p}}^+ = \frac{1}{V_t} \int_{\mathscr{B}_t} \left[\nabla_{\boldsymbol{x}} \boldsymbol{p} : \left(\nabla_{\boldsymbol{x}} \boldsymbol{w} \right)^t + \boldsymbol{p} \cdot \operatorname{div} \left(\nabla_{\boldsymbol{x}} \boldsymbol{w} \right)^t \right] \mathrm{d}v, \tag{4.64}$$

does not vanish generally.

The virtual work in terms of $\boldsymbol{p}_M$ reads

$$p_{tM} = \mathrm{d}_\delta U_{tM} = \mathrm{d}_\delta \boldsymbol{f}_M : \boldsymbol{p}_M - \mathrm{d}_\delta \boldsymbol{\Phi} \cdot \boldsymbol{B}_{tM}, \tag{4.65}$$

which by the definition of the macroscopic material two-point stress (4.59) or (4.61) and the corresponding body forces (4.63) transforms to

$$p_{tM} = \mathrm{d}_\delta \boldsymbol{f}_M : \frac{1}{V_t} \left[\int_{\partial \mathscr{B}_t} \boldsymbol{T}_t \otimes \boldsymbol{x} \, \mathrm{d}a + \int_{\mathscr{S}_t} \boldsymbol{T}_t^s \otimes \boldsymbol{w} \, \mathrm{d}a - \int_{\mathscr{B}_t} \boldsymbol{p} \cdot \left(\nabla_{\boldsymbol{x}} \boldsymbol{w} \right)^t \mathrm{d}v \right] - \mathrm{d}_\delta \boldsymbol{\Phi}_M \cdot \operatorname{div} \bar{\boldsymbol{p}}^+. \tag{4.66}$$

By application of the variational form of the material scale-transition (4.15) and straight-forward calculation the Hill-Mandel type condition formulated in terms of $\boldsymbol{p}_M$ reads

$$p_{tM} = \bar{p}_t + \bar{p}_t^{\mathrm{int}}, \tag{4.67}$$

whereby the internal contribution to the macroscopic virtual work is given by

$$\bar{p}_t^{\mathrm{int}} = -\mathrm{d}_\delta \boldsymbol{\Phi}_M \cdot \operatorname{div} \bar{\boldsymbol{p}}^+. \tag{4.68}$$

The explicit derivation of this Hill-Mandel type condition for the more general case of a graded micro-material is given in Appendix C.2.

Remark 6 *In the case of a graded microscopic material, extra terms which depend on the explicit derivative of the strain energy functional with respect to the spatial or material coordinates, respectively, have to be incorporated additionally. Thus, the macroscopic Eshelby stress in terms of a volume integral reads*

$$\boldsymbol{\Sigma}_M = \frac{1}{V_0} \int_{\mathscr{B}_0} \left[\boldsymbol{\Sigma} + \frac{\partial U_0}{\partial \boldsymbol{X}} |_{expl.} \otimes \boldsymbol{\Phi} \right] \mathrm{d}V, \tag{4.69}$$

which yields the following formulation for the corresponding macroscopic volume forces

$$\boldsymbol{B}_{0M} = -\frac{1}{V_0} \int_{\partial \mathscr{B}_0} \frac{\partial U_0}{\partial \boldsymbol{X}}|_{expl.} \, \mathrm{d}V. \tag{4.70}$$

In contrast to the Hill-Mandel type condition for the non-graded material, compare equation (4.58)*, for the more general case of a graded material an extra contribution needs to be added, i.e., it holds*

$$p_{0M} = \bar{p}_0 + \bar{p}_0^{grad}, \tag{4.71}$$

whereby the term that emerges due to the graded character results in

$$\bar{p}_0^{grad} = d_\delta \boldsymbol{\Phi}_M \cdot \frac{1}{V_0} \int_{\mathscr{B}_0} \frac{\partial U_0}{\partial \boldsymbol{X}}|_{expl.} \, \mathrm{d}V. \tag{4.72}$$

In the same way, the macroscopic two-point stress which is defined by a push-forward operation of the macroscopic Eshelby stress, contains an additional term $\bar{\boldsymbol{p}}^+$, i.e.,

$$\boldsymbol{p}_M = \bar{\boldsymbol{p}} - \bar{\boldsymbol{p}}^+, \tag{4.73}$$

wherein the additional term is given by

$$\bar{\boldsymbol{p}}^+ = \frac{1}{V_t} \int_{\mathscr{B}_t} \left[\boldsymbol{p} \cdot \left(\nabla_{\boldsymbol{x}} \boldsymbol{w} \right)^t + \left[\boldsymbol{F}^t \cdot \frac{\partial U_t}{\partial \boldsymbol{x}}|_{expl.} \right] \otimes \left[\boldsymbol{w} + \boldsymbol{\varphi}_M \right] \right] \, \mathrm{d}v, \tag{4.74}$$

see equation (4.62) *for the non-graded special case. Consequently, the corresponding volume forces result in*

$$\boldsymbol{B}_{t_M} = -\operatorname{div} \boldsymbol{p}_M = -\frac{1}{V_t} \int_{\mathscr{B}_t} \boldsymbol{F}^t \cdot \frac{\partial U_t}{\partial \boldsymbol{x}}|_{expl.} \, \mathrm{d}v + \operatorname{div} \bar{\boldsymbol{p}}^+. \tag{4.75}$$

By means of this macroscopic material two-point stress the Hill-Mandel condition reads

$$p_{tM} = \bar{p}_t + \bar{p}_t^{int}, \tag{4.76}$$

whereby the internal extra contribution is given by

$$\bar{p}_t^{int} = d_\delta \boldsymbol{\Phi}_M : \left[\frac{1}{V_t} \int_{\mathscr{B}_t} \boldsymbol{F}^t \cdot \frac{\partial U_t}{\partial \boldsymbol{x}}|_{expl.} \, \mathrm{d}v - \operatorname{div} \bar{\boldsymbol{p}}^+ \right], \tag{4.77}$$

see Appendix C.2 for a detailed derivation.

In summary, the approach based on the homogenized Eshelby stress tensor yields a consistent formulation of the virtual work balance, i.e., no extra contributions are necessary in the Hill-Mandel type condition by means of $\boldsymbol{\Sigma}_M$, if a non-graded microscopic material is assumed. Nevertheless, if graded materials are considered an extra term depending on the explicit derivative of the strain energy functional needs to be incorporated. Furthermore, these extra terms are inevitable if a push-forward to the material two-point stress is carried out. Due to the existence of these extra terms in the numerical examples in Section 4.3 the macroscopic material forces are determined in terms of the Eshelby stress, which yields consistent material stress measure. For the sake of completeness, in the following subsection a third approach for the homogenization of material quantities is outlined based on the averaged material two-point stress.

4.2.3 Homogenized Material Stresses based on the Averaged Material Two-Point Stress Tensor

A third possibility to determine homogenized material is given by means of the averaged material two-point stress, i.e., the initial point for this approach is given by

$$\boldsymbol{p}_M^p := \bar{\boldsymbol{p}} = \frac{1}{V_t}\left[\int_{\partial\mathscr{B}_t} \boldsymbol{T}_t \otimes \boldsymbol{x}\ \mathrm{d}a + \int_{\mathscr{S}_t} \boldsymbol{T}_t^s \otimes \boldsymbol{x}\ \mathrm{d}a\right]. \tag{4.78}$$

If a non-graded microscopic material is considered, with assistance of equation (4.11), the macroscopic two-point stress may be reformulated by

$$\boldsymbol{p}_M^p = \frac{1}{V_t}\int_{\mathscr{B}_t} \boldsymbol{p}\ \mathrm{d}v. \tag{4.79}$$

The corresponding macroscopic volume forces are determined via

$$\boldsymbol{B}_{tM} = -\operatorname{div} \boldsymbol{p}_M, \tag{4.80}$$

which due to vanishing spatial volume forces and the assumed non-graded material vanish, i.e.,

$$\boldsymbol{B}_{tM} = \boldsymbol{0}. \tag{4.81}$$

The macroscopic virtual work in terms of the defined macroscopic material two-point stress is given by

$$p_{tM}^p = \mathrm{d}_\delta U_{tM} = \mathrm{d}_\delta \boldsymbol{f}_M : \boldsymbol{p}_M^p. \tag{4.82}$$

Application of the definition of $\boldsymbol{p}_M^p$ as in (4.78) yields

$$p_{tM}^p = \mathrm{d}_\delta \boldsymbol{f}_M : \frac{1}{V_t} \left[\int_{\partial \mathscr{B}_t} \boldsymbol{T}_t \otimes \boldsymbol{x} \, \mathrm{d}a + \int_{\mathscr{S}_t} \boldsymbol{T}_t^s \otimes \boldsymbol{x} \, \mathrm{d}a \right]. \tag{4.83}$$

By expansion with assistance of the variation of the material deformation map p_{tM}^p results in

$$\begin{aligned} p_{tM}^p &= \frac{1}{V_t} \left[\int_{\partial \mathscr{B}_t} \boldsymbol{T}_t \cdot \mathrm{d}_\delta \boldsymbol{\Phi} \, \mathrm{d}a + \int_{\mathscr{S}_t} \boldsymbol{T}_t^s \otimes \mathrm{d}_\delta \boldsymbol{\Phi} \, \mathrm{d}a \right] \\ &+ \frac{1}{V_t} \left[\int_{\partial \mathscr{B}_t} \boldsymbol{T}_t \, \mathrm{d}a + \int_{\mathscr{S}_t} \boldsymbol{T}_t^s \, \mathrm{d}a \right] \cdot \left[\mathrm{d}_\delta \boldsymbol{f}_M \cdot \boldsymbol{\varphi}_M \right] \\ &+ \mathrm{d}_\delta \boldsymbol{f}_M : \frac{1}{V_t} \left[\int_{\partial \mathscr{B}_t} \boldsymbol{T}_t \otimes \boldsymbol{w} \, da + \int_{\mathscr{S}_t} \boldsymbol{T}_t^s \otimes \boldsymbol{w} \, \mathrm{d}a \right]. \end{aligned} \tag{4.84}$$

Therein, the first term on the right-hand side is identified with the average of the microscopic virtual work, whereas the second term vanishes for the non-graded material at hand. Thus, by manipulation of the last term on the right-hand side the Hill-Mandel type conditions reads

$$p_{tM}^p = \bar{p}_t + p_t^{p\,\mathrm{int}}, \tag{4.85}$$

wherein the internal extra term is given by

$$p_t^{p\,\mathrm{int}} = \mathrm{d}_\delta \boldsymbol{f}_M : \frac{1}{V_t} \int_{\mathscr{B}_t} \boldsymbol{p} \cdot \left(\nabla_{\boldsymbol{x}} \boldsymbol{w} \right)^t \, \mathrm{d}v. \tag{4.86}$$

Please note, that this internal extra term does not vanish generally. Thus, in contrast to the approach based on the averaged Eshelby stress tensor in the approach at hand, the Hill-Mandel type condition formulated in the primal variable also requires an internal contribution.

In a next step, the corresponding macroscopic Eshelby stress is elaborated based on

$$\begin{aligned}
\boldsymbol{\Sigma}_M^p &:= J_M \, \boldsymbol{p}_M^p \cdot \boldsymbol{f}_M^t \\
&= \frac{V_t}{V_0} \frac{1}{V_t} \left[\int_{\partial \mathscr{B}_t} \boldsymbol{T}_t \otimes \boldsymbol{x} \, \mathrm{d}a + \int_{\mathscr{S}_t} \boldsymbol{T}_t^s \otimes \boldsymbol{x} \, da \right] \cdot \boldsymbol{f}_M^t \\
&= \frac{1}{V_0} \left[\int_{\partial \mathscr{B}_t} \boldsymbol{T}_t \otimes \left[\boldsymbol{f}_M \cdot \boldsymbol{x} \right] \, \mathrm{d}a + \int_{\mathscr{S}_t} \boldsymbol{T}_t^s \otimes \left[\boldsymbol{f}_M \cdot \boldsymbol{x} \right] \, \mathrm{d}a \right] . \qquad (4.87)
\end{aligned}$$

Application of the material scale-transition to substitute $\boldsymbol{f}_M \cdot \boldsymbol{x}$ yields

$$\begin{aligned}
\boldsymbol{\Sigma}_M^p &= \frac{1}{V_0} \left[\int_{\partial \mathscr{B}_t} \boldsymbol{T}_t \otimes \boldsymbol{X} \, \mathrm{d}a + \int_{\mathscr{S}_t} \boldsymbol{T}_t \otimes \boldsymbol{X} \, \mathrm{d}a \right] \\
&+ \frac{1}{V_0} \left[\int_{\partial \mathscr{B}_t} \boldsymbol{T}_t \, \mathrm{d}a + \int_{\mathscr{S}_t} \boldsymbol{T}_t^s \, \mathrm{d}a \right] \otimes \left[\boldsymbol{f}_M \cdot \boldsymbol{\varphi}_M \right] \\
&+ \frac{1}{V_0} \left[\int_{\partial \mathscr{B}_t} \boldsymbol{T}_t \otimes \boldsymbol{w} \, \mathrm{d}a + \int_{\mathscr{S}_t} \boldsymbol{T}_t^s \otimes \boldsymbol{w} \, \mathrm{d}a \right] \cdot \boldsymbol{f}_M^t . \qquad (4.88)
\end{aligned}$$

Therein, for the regarded non-graded micro-material at hand, the second term at the right-hand side vanishes due to the vanishing spatial volume forces. Furthermore, the first and the last integral at the right-hand side of (4.88) are reformulated by integral manipulations, see Appendix B for details, in particular equations (B.7) and (B.13). Thus, the macroscopic Eshelby stress of the approach at hand reads

$$\boldsymbol{\Sigma}_M^p = \bar{\boldsymbol{\Sigma}} + \bar{\boldsymbol{\Sigma}}^+ , \qquad (4.89)$$

whereby

$$\bar{\boldsymbol{\Sigma}}^+ = \frac{1}{V_0} \int_{\mathscr{B}_0} \boldsymbol{\Sigma} \cdot \left(\nabla_{\boldsymbol{X}} \boldsymbol{w} \right) \, \mathrm{d}V . \qquad (4.90)$$

Consequently, the macroscopic volume forces connected to $\boldsymbol{\Sigma}_M^p$ are derived via

$$\boldsymbol{B}_{0M}^p = -\mathrm{Div} \boldsymbol{\Sigma}_M^p = -\mathrm{Div} \bar{\boldsymbol{\Sigma}}^+ . \qquad (4.91)$$

In detail, the volume forces result in

$$\boldsymbol{B}_{0M}^{p} = -\frac{1}{V_0} \int_{\partial \mathscr{B}_0} \left[\nabla_{\boldsymbol{X}} \boldsymbol{\Sigma} : \left(\nabla_{\boldsymbol{X}} \boldsymbol{w} \right)^t + \boldsymbol{\Sigma} \cdot \mathrm{Div} \left(\nabla_{\boldsymbol{X}} \boldsymbol{w} \right)^t \right] \mathrm{d}V. \tag{4.92}$$

Finally, the Hill-Mandel type condition for $\boldsymbol{\Sigma}_M^p$ is elaborated. The macroscopic virtual work formulated in the Eshelby stress tensor reads

$$p_{0M}^{p} = J_M \, \mathrm{d}_\delta U_{tM} = \left[\mathrm{d}_\delta \boldsymbol{f}_M \cdot \boldsymbol{F}_M \right] : \boldsymbol{\Sigma}_M^p - \mathrm{d}_\delta \Phi_M \cdot \boldsymbol{B}_{0M}^p, \tag{4.93}$$

which by definition of the macroscopic Eshelby stress (4.89) and the corresponding body forces transforms to

$$p_{0M}^{p} = \left[\mathrm{d}_\delta \boldsymbol{f}_M \cdot \boldsymbol{F}_M \right] : \bar{\boldsymbol{\Sigma}} + \left[\mathrm{d}_\delta \boldsymbol{f}_M \cdot \boldsymbol{F}_M \right] : \frac{1}{V_0} \int_{\mathscr{B}_0} \boldsymbol{\Sigma} \cdot \left(\nabla_{\boldsymbol{X}} \boldsymbol{w} \right)^t \, \mathrm{d}V - \mathrm{d}_\delta \boldsymbol{\Phi}_M \cdot \mathrm{Div} \bar{\boldsymbol{\Sigma}}^+. \tag{4.94}$$

In equation (4.58) it already has been shown that the first term on the right-hand side of this equation corresponds to the averaged microscopic virtual work $\bar{p}_0$. Thus, the Hill-Mandel type condition for this approach to determine the macroscopic Eshelby stress tensor reads

$$p_{0M}^{p} = \bar{p}_0 + \bar{p}_0^{\mathrm{p\,int}}, \tag{4.95}$$

whereby the internal extra contribution is given by

$$\bar{p}_0^{\mathrm{p\,int}} = \left[\mathrm{d}_\delta \boldsymbol{f}_M \cdot \boldsymbol{F}_M \right] : \bar{\boldsymbol{\Sigma}}^+ + \mathrm{d}_\delta \boldsymbol{\Phi}_M \cdot \mathrm{Div} \bar{\boldsymbol{\Sigma}}^+. \tag{4.96}$$

Due to the fact that the presented approach based on the averaged material two-point stress requires an internal extra contribution in the Hill-Mandel type condition formulated in the primal variable, i.e., $\boldsymbol{p}_M^p$ as well as in the dual variable, i.e., $\boldsymbol{\Sigma}$ even in the special case of a non-graded micro-material, the more general case of a graded material is not considered here. Hence, in the following numerical examples only the first two homogenization approaches are compared and focus is especially put onto the approach based on the averaged Eshelby stress tensor because the material crack tip forces are determined by means of this stress measure which for a non-graded microscopic material yields a virtual work consistent ansatz, i.e., no extra terms depending on the fluctuations are required in the Hill-Mandel type condition.

4.3 Numerical Examples –Material Motion Problem

In the following section, elucidating numerical examples are given for the determination of macroscopic material quantities depending on the underlying microscopic structure. To this end, firstly the spatial homogenization process is carried out in

terms of periodic boundary conditions according to Section 3. Then, in a post-processing step the macroscopic material quantities, i.e., the Eshelby stress and the material node point forces are determined. Here, the two different approaches are compared. Focus is put onto the Eshelby stress $\boldsymbol{\Sigma}_M^*$ (and the corresponding material crack tip forces $\mathfrak{F}_M^*$) determined by means of averaged spatial quantities and onto the Eshelby stress $\boldsymbol{\Sigma}_M$ (and the corresponding forces $\mathfrak{F}_M$) according to Sections 4.2.1 and 4.2.2. Please note, that the direct approach, which yields $\boldsymbol{\Sigma}_M^*$, in contrast to the approach based on averaging the Eshelby stress, is not consistent in terms of the averaged virtual work, i.e., an internal extra contribution to the Hill-Mandel conditions is necessary even for ungraded micro-materials.

4.3.1 Microscopic Examples –Material Motion Problem

In a first example the representativeness of the elaborated material homogenization scheme is studied. Therefore, three different representations of a simple microstructure and their material responses in terms of the averaged Eshelby stress tensor are compared. The considered microscopic structure consists of two materials with different stiffnesses which are connected by a horizontal interface. The Young's modulus of the softer material is chosen as $E_1 = 100\ \mathrm{N/mm^2}$ whereas the other material is assumed to behave 10 times stiffer, i.e., $E_2 = 1000\ \mathrm{N/mm^2}$. For both materials the Poisson's ratio reads $\nu = 0.3$. The simulations are carried out in terms of a Neo-Hookean material law according to Section 2.3.1. The macroscopic deformation gradient is prescribed as

$$\boldsymbol{F}_M = \begin{bmatrix} 1.20 & 0.15 \\ 0.15 & 0.90 \end{bmatrix}. \tag{4.97}$$

The deformed RVEs and the material forces at the interfaces are illustrated in Figure 4.4. This Figure also reveals that the same averaged Eshelby stresses result for all representations.

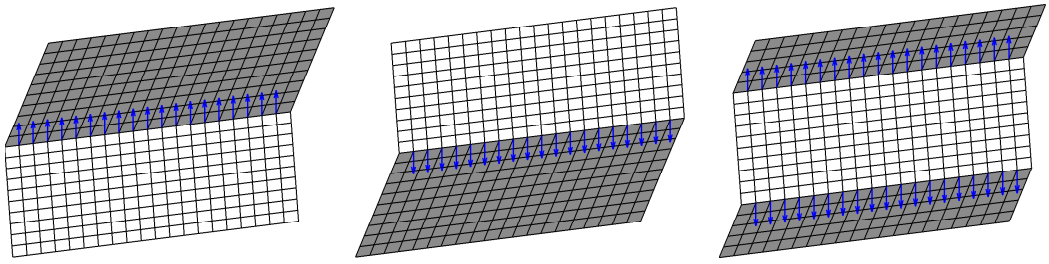

$$\boldsymbol{\Sigma}_M = \begin{bmatrix} -174.81 & -37.22 \\ -37.22 & 38.42 \end{bmatrix}, \begin{bmatrix} -174.81 & -37.22 \\ -37.22 & 38.42 \end{bmatrix}, \begin{bmatrix} -174.81 & -37.22 \\ -37.22 & 38.42 \end{bmatrix}$$

Figure 4.4: Different RVEs representing the same micro-structure and corresponding averaged Eshelby stress tensors in $[\mathrm{N/mm^2}]$

Similarly, the macroscopic Eshelby stress in terms of averaged spatial quantities reads the same for the different representations. It holds

$$\boldsymbol{\Sigma}_M^* = \begin{bmatrix} -174.81 & -37.22 \\ -67.11 & 38.42 \end{bmatrix} \text{[N/mm}^2\text{]}. \tag{4.98}$$

Thus, both represented approaches for the determination of the macroscopic Eshelby stress yield representative solutions, i.e., the macroscopic Eshelby stress is independent from the chosen cutting of the microscopic structure. Please note, that the approach based on averaged spatial variables yields an unsymmetric Eshelby stress tensor and thus captures the anisotropic nature of the microscopic material response which results from the different stiffnesses of the materials. Contrarily, the response based on the averaged Eshelby stress is symmetric due to the isotropy of the single microscopic constituents. The Eshelby stresses resulting from the two approaches only differ in one component due to the simple geometry of the microstructure.

In the next example, the influence of different material behaviors to the macroscopic Eshelby stress tensors is studied. Therefore, an anisotropic St. Venant-Kirchhoff hyperelastictiy is compared to an isotropic St. Venant-Kirchhoff law according to Section 2.3.2. In order to model the anisotropy, the anisotropic elasticity tensor

$$\mathbb{C} = \begin{bmatrix} C_{11} & C_{12} & 0 \\ C_{21} & C_{22} & 0 \\ 0 & 0 & C_{33}, \end{bmatrix}. \tag{4.99}$$

for the plane strain case is applied, instead of the isotropic elasticity tensor as given in (2.44). Thus, in general the anisotropy includes five independent material parameters. The grade of anisotropy is surveyed by the anisotropy ratio

$$Z = \frac{2\,C_{33}}{C_{11} - C_{12}}, \tag{4.100}$$

see the work of Bacon et al. [1] or Buryachenko [8] for details. The material is isotropic, i.e., does not posses preferred orientations, which results in the same stress-strain relation in each direction, if $Z = 1$.

In the current example, a nickel material is assumed at the micro-level. For nickel it holds that $C_{11} = C_{22}$ and $C_{12} = C_{21}$ and therefore only three material parameters are necessary. These constants of the elasticity tensor are given by $C_{11} = C_{22} = 246.5$ kN/mm^2, $C_{12} = 147.3$ kN/mm^2 and $C_{33} = 124.7$ kN/mm^2. Thus, the anisotropy ratio for nickel is $Z = 2.51$.

For the isotropic St. Venant Kirchhoff law only two material parameters are required. These material parameters are given in terms of the Young's modulus and the Poisson's ratio as $E = 200$ kN/mm^2 and $\nu = 0.3$, see the textbook by Ross and Maile [74]. The coefficients of the elasticity tensor $\mathbb{C}$ can be expressed by means of

E and ν via

$$\mathbb{S} = \mathbb{C}^{-1} = \begin{bmatrix} \frac{1}{E} & -\frac{\nu}{E} & 0 \\ \frac{\nu}{E} & \frac{1}{E} & 0 \\ 0 & 0 & \frac{1}{G} \end{bmatrix}, \tag{4.101}$$

wherein G denotes the shear modulus

$$G = \frac{E}{2(1+\nu)}. \tag{4.102}$$

Thus, the components of the elasticity tensor $\mathbb{C}$ read $C_{11} = C_{22} = 219.8\,\mathrm{kN/mm^2}$, $C_{12} = C_{21} = 65.9\,\mathrm{kN/mm^2}$ and $C_{33} = 76.9\,\mathrm{kN/mm^2}$.

In Figure 4.5 the deformed RVEs for the isotropic and the anisotropic St. Venant-Kirchhoff constitutive law are displayed for a prescribed macroscopic deformation gradient

$$\boldsymbol{F}_M = \begin{bmatrix} 0.99 & 0.02 \\ 0.02 & 1.03 \end{bmatrix}. \tag{4.103}$$

On the one hand, for the isotropic material law the anisotropy of the whole RVE, which is due to the asymmetric void, is captured by the approach based on averaged spatial variables, i.e., $\boldsymbol{\Sigma}_M^*$ is non-symmetric, which generally reflects an anisotropic material behavior. On the other hand, the approach based on averaging the microscopic Eshelby stress tensor results in a symmetric macroscopic Eshelby stress $\boldsymbol{\Sigma}_M$ due to the fact that here an isotropic law is considered and thus the averaging process is carried out as an averaging of symmetric tensors.

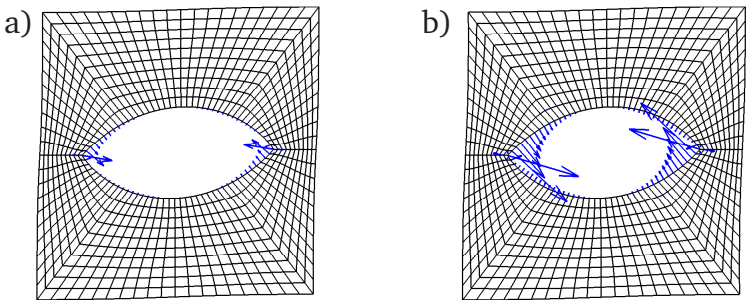

$$\boldsymbol{\Sigma}_M = \begin{bmatrix} 263 & -2352 \\ -2352 & -4126 \end{bmatrix}, \qquad \begin{bmatrix} -981 & -3473 \\ -3579 & -4077 \end{bmatrix}$$

$$\boldsymbol{\Sigma}_M^* = \begin{bmatrix} 590 & -1804 \\ -1802 & -3065 \end{bmatrix}, \qquad \begin{bmatrix} -454 & -2641 \\ -2753 & -3025 \end{bmatrix}$$

Figure 4.5: Deformed microscopic RVEs for a) isotropic and b) anisotropic St. Venant-Kirchhoff material law with material forces and corresponding macroscopic Eshelby stress tensors in $[\mathrm{N/mm^2}]$

For the anisotropic St. Venant-Kirchhoff constitutive law both approaches reflect the anisotropic behavior by non-symmetric macroscopic Eshelby stress tensors. For the approach based on averaging the Eshelby stress tensor this asymmetry is due to the asymmetric microscopic Eshelby stresses, which result from the material law. The exact stress tensors are given in Figure 4.5.

4.3.2 Micro-Macro Transition –Material Motion Problem

In the sequel, the influence of different RVEs onto homogenized macroscopic material quantities is studied by carrying out a full micro-macro transition. In all examples a Neo-Hookean hyperelastic micro-material is assumed. At the macro-scale a rectangular structure with a prescribed horizontal crack is considered.

Influence of Micro-Structure onto Macroscopic Material Response –Void Orientation

In the first example, the influence of the microscopic void orientation in an RVE onto the macroscopic material response is highlighted. Therefore, RVEs containing a horizontally and a vertically orientated lens-like void are compared, see Figure 4.6 for the undeformed settings.

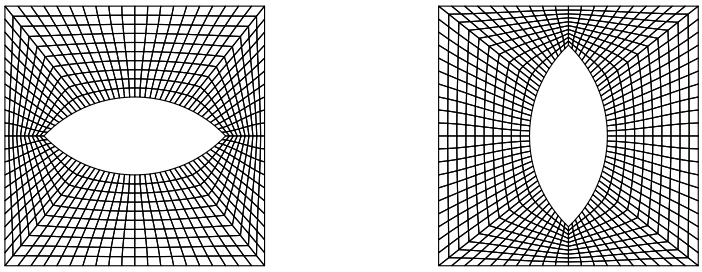

Figure 4.6: Undeformed microscopic structures containing different lens-like voids

For the simulation the microscopic Young's modulus is given by $E = 1000\ \mathrm{N/mm^2}$ and the Poisson's ratio by $\nu = 0.3$. Firstly, at the macro-level displacements in longitudinal direction are prescribed. The deformed macroscopic structures and the corresponding material forces as well as the data for the material crack tip forces for the compared approaches are given in Figure 4.7. Both approaches yield material crack tip forces in horizontal direction, but the values of the resulting material crack tip forces differ. Although, the different approaches yield quantitatively different values, the same macroscopic behavior is observed. The structure with the underlying horizontally orientated lentil-shaped void yields a smaller material crack tip force than the structure with the underlying vertically orientated void. This results in the following interpretation: The structure with the underlying horizontal void yields a softer material response and thus also the crack tip force results smaller.

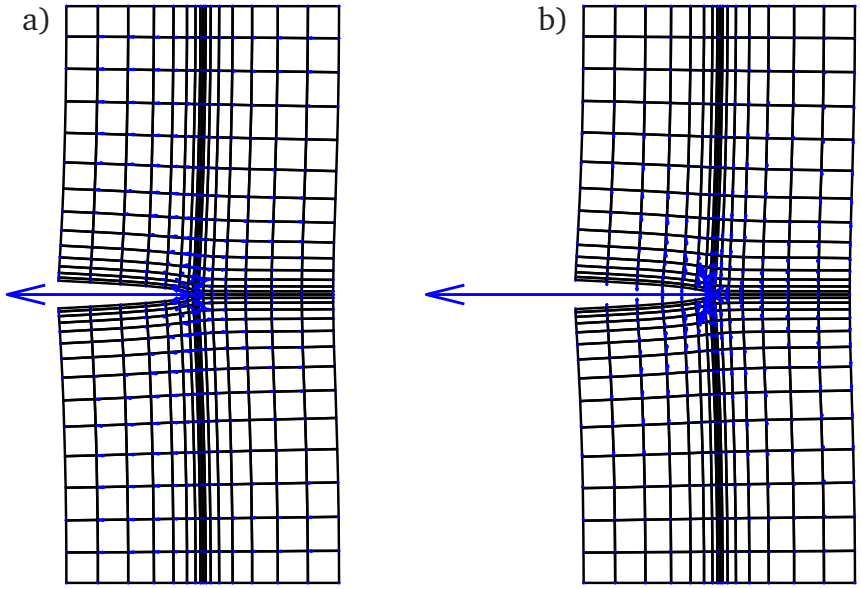

$$\mathfrak{F}_M = \begin{bmatrix} -4.5543 \\ 0 \end{bmatrix}, \qquad \begin{bmatrix} -6.9201 \\ 0 \end{bmatrix}$$

$$\mathfrak{F}^*_M = \begin{bmatrix} -4.0048 \\ 0 \end{bmatrix}, \qquad \begin{bmatrix} -5.6459 \\ 0 \end{bmatrix}$$

Figure 4.7: Deformed macroscopic structures with underlying RVE with a) horizontally and b) vertically orientated void and corresponding material crack tip force in [N]

The observation that the vertical void yields a stiffer macroscopic material response is confirmed by the macroscopic Cauchy stresses in longitudinal direction, see Figure 4.8. Therein, the stiffer material response is tracked by the greater stresses around the crack tip for the structure at the right-hand side.

The growth of the material crack tip forces with increasing displacements is illustrated in Figure 4.9. It is observed that the greater the loading is the greater results the difference between the macroscopic forces. Please note, that in all figures the displayed macroscopic material forces $\mathfrak{F}_M$, resulting from the approach based on the averaged Eshelby stress, are plotted.

Finally, focus is put onto the microscopic structure. Therefore, RVEs in the vicinity of the crack tip are compared, see Figure 4.10 for the deformed settings and the microscopic material forces. For both RVEs the different approaches yield different macroscopic Eshelby stresses. The Eshelby stress tensor Σ^*_M of the direct approach yields in both cases smaller stresses, which is a consequence of the extra contribution depending on the gradient of the microscopic fluctuations –compare (4.29). Furthermore, it is observed that in both approaches the vertically orientated lens-like void yields greater Eshelby stresses than the horizontally orientated void. This leads to the smaller material crack tip force for the underlying horizontal void, which has already been discussed above.

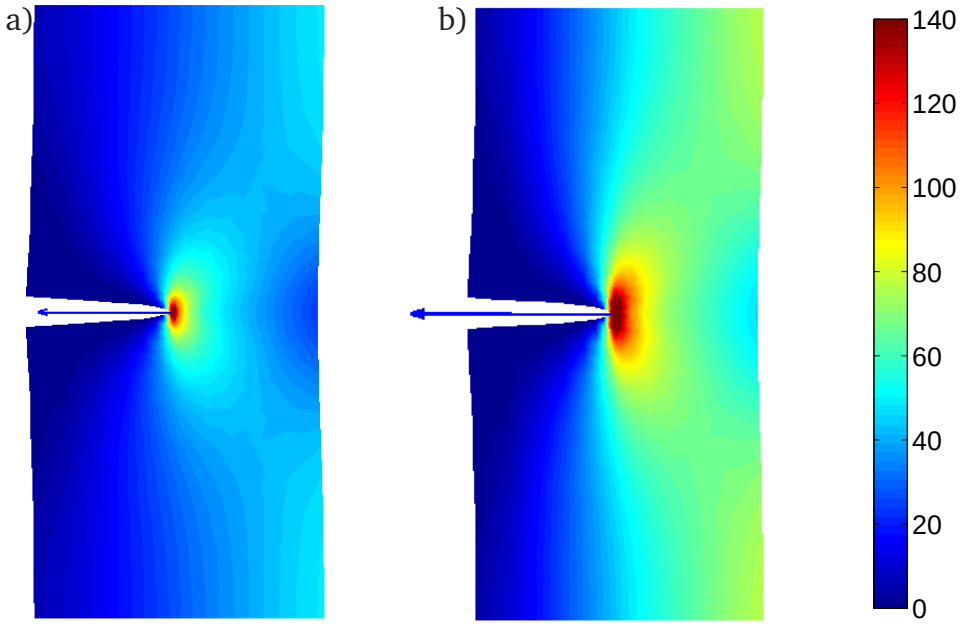

Figure 4.8: Macroscopic longitudinal Cauchy stressses in [N/mm^2] for structures with underlying RVE with a) horizontally and b) vertically orientated lens-like void

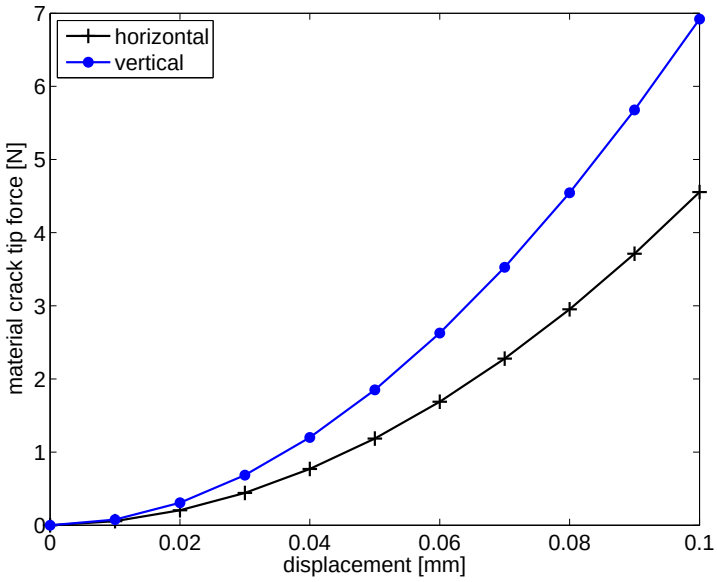

Figure 4.9: Comparison of absolute value of macroscopic crack tip forces due to applied displacement for underlying RVEs containing different lentil-shaped voids

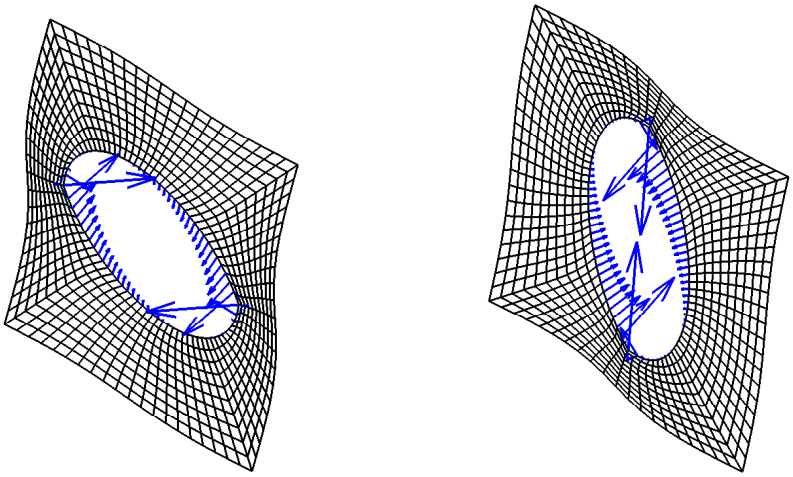

$$\boldsymbol{\Sigma}_M = \begin{bmatrix} -250.5550 & 256.0042 \\ 256.0042 & -286.1621 \end{bmatrix}, \begin{bmatrix} -288.9162 & 312.4671 \\ 312.4671 & -339.4131 \end{bmatrix}$$

$$\boldsymbol{\Sigma}^*_M = \begin{bmatrix} -180.4740 & 211.1613 \\ 246.5094 & -175.5219 \end{bmatrix}, \begin{bmatrix} -162.4087 & 311.0454 \\ 259.5310 & -253.4164 \end{bmatrix}$$

Figure 4.10: Deformed microscopic RVEs with material forces and corresponding macroscopic Eshelby stress tensors in [N/mm^2]

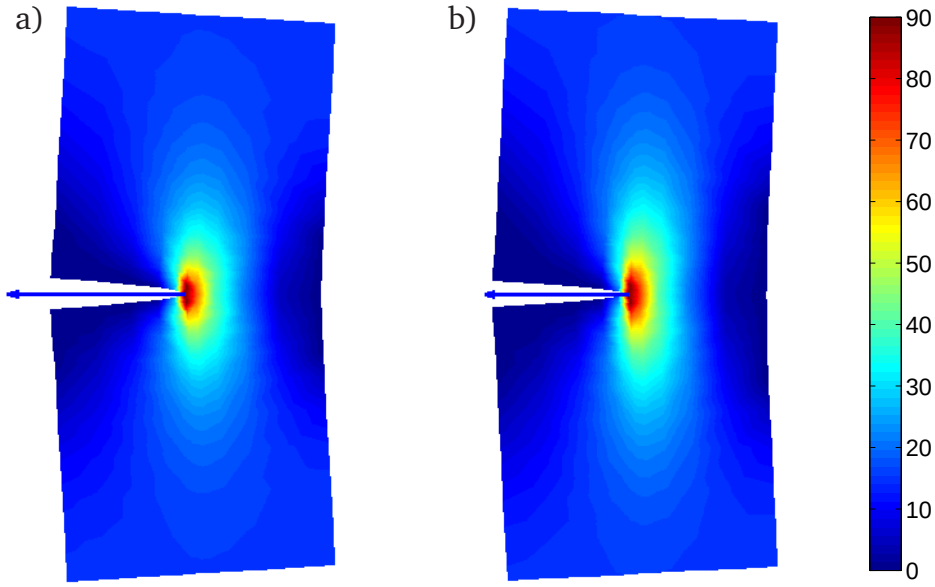

$$\mathfrak{F}_M = \begin{bmatrix} -3.2986 \\ 0 \end{bmatrix}, \begin{bmatrix} -2.6482 \\ 0 \end{bmatrix}$$

$$\mathfrak{F}^*_M = \begin{bmatrix} -3.3853 \\ 0 \end{bmatrix}, \begin{bmatrix} -2.8511 \\ 0 \end{bmatrix}$$

Figure 4.11: Macroscopic longitudinal Cauchy stressses in [N/mm^2] and and corresponding material crack tip force in [N] for structures with underlying RVE with a) horizontally and b) vertically orientated lens-like void

Secondly, for the same underlying micro-structures the resulting macroscopic crack tip forces are compared for applied tractions at the macroscopic boundary in longitudinal direction. This loading yields a similar macroscopic stress distributions for both underlying RVEs as illustrated in Figure 4.11. Therein, it also can be observed that the macroscopic crack tip forces differ for both approaches. The absolute values of $\mathfrak{F}_M$ and $\mathfrak{F}_M^*$ vary, but in both cases the RVE with the horizontally orientated void results in a bigger crack tip force. Thus, for the same macroscopic stress in the macro-structure with the underlying horizontal void the crack tends to propagate more than in the macro-structure with the underlying vertical void. This result is due to the fact that the orientation of the horizontal lens-like void coincides with the direction of the prescribed crack and therewith the influence of the microscopic setting onto the microscopic crack tip force has been illustrated.

Influence of Micro-Structure onto Macroscopic Material Response –Orientation of Interface

In the next example the influence of the orientation of a microscopic interface to the macroscopic material crack tip forces is elaborated. Therefore, two RVEs containing straight interfaces between materials with different stiffnesses are considered. In one RVE the materials are connected by a horizontal interface, for the other one the structure is rotated via 90 degrees and thus the interface is orientated vertically, see Figure 4.12 for the undeformed meshes.

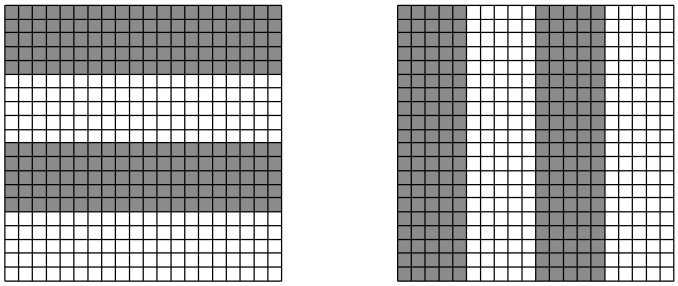

Figure 4.12: Undeformed microscopic structures with horizontal and vertical interface

The material parameters at the micro-level are chosen such that one material is two times stiffer than the other material, i.e., it holds $E_1 = 500\ \mathrm{N/mm^2}$, $E_2 = 2\,E_1 = 1000\ \mathrm{N/mm^2}$ and $\nu_1 = \nu_2 = 0.3$. At the macro-level displacements in longitudinal direction are prescribed. Figure 4.13 illustrates the deformed macroscopic structures with Cauchy stresses in longitudinal direction and the corresponding macroscopic crack tip forces. Therein, the higher stress peaks around the crack tip at the left-hand side of the Figure indicate that the RVE with the vertical interface yields a stiffer material response than the RVE with the horizontal interface. This observation is confirmed by the crack tip forces. Once more, for the vertical interface the different approaches yield different values for the crack tip forces. For

the horizontal interface $\mathfrak{F}_M$ and $\mathfrak{F}_M^*$ are the same which is due to the simple shape of the interface geometry. Furthermore, for both approaches the macroscopic crack tip force for the underlying vertical interface is greater than for the horizontal interface which represents an indicator for a softer material response of the latter one.

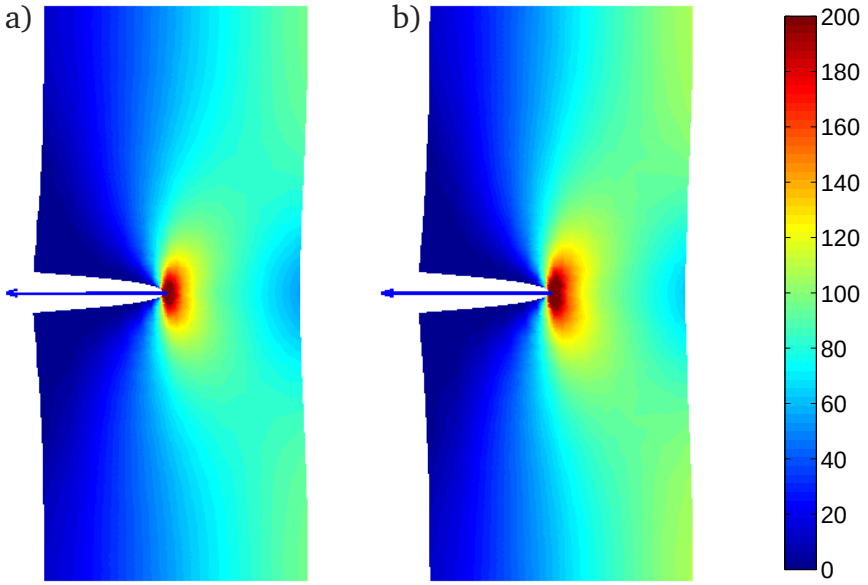

$$\mathfrak{F}_M = \begin{bmatrix} -11.9060 \\ 0 \end{bmatrix}, \qquad \begin{bmatrix} -12.6947 \\ 0 \end{bmatrix}$$

$$\mathfrak{F}_M^* = \begin{bmatrix} -11.9060 \\ 0 \end{bmatrix}, \qquad \begin{bmatrix} -13.1941 \\ 0 \end{bmatrix}$$

Figure 4.13: Macroscopic longitudinal Cauchy stresses in [N/mm^2] and corresponding material crack tip forces in [N] for structures with underlying RVE with a) horizontally and b) vertically orientated interfaces

The different material responses of the considered approaches is also observed by focusing on the different Eshelby stresses in a single simulation point. Therefore, two RVEs at the same macroscopic point and the corresponding Eshelby stresses are displayed in Figure 4.14. For the RVE with the horizontal interface Eshelby stress tensor only differs in 2-1 component although the applied macroscopic deformation gradient yields a rather inhomogeneous deformation. In detail in the considered macroscopic simulation point it holds

$$\boldsymbol{F}_M = \begin{bmatrix} 1.0258 & 0.2319 \\ -0.9585 & 1.3815 \end{bmatrix}. \tag{4.104}$$

Thus, the integral that connects $\boldsymbol{\Sigma}_M$ and $\boldsymbol{\Sigma}_M^*$, compare (4.29), only possess one non-vanishing component, which is due to the chosen simple interface geometry. Similar observations are obtained from a comparison of the Eshelby stresses resulting from the RVE with the vertical interface. In this case only the 1-2 component differs.

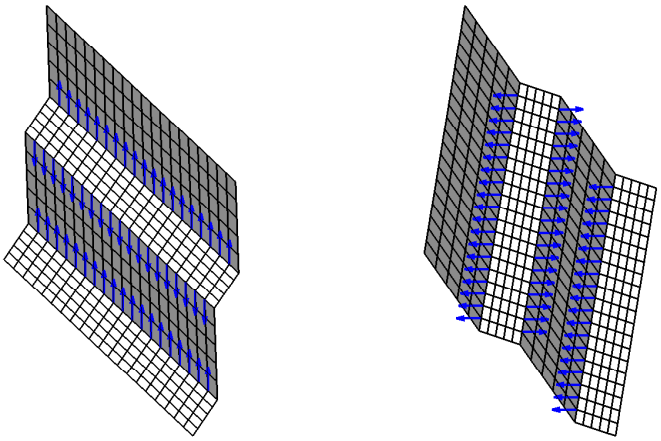

$$\boldsymbol{\Sigma}_M = \begin{bmatrix} -411.2119 & 470.7256 \\ 470.7256 & -339.2192 \end{bmatrix}, \begin{bmatrix} -397.4095 & 495.8422 \\ 495.8422 & -375.1100 \end{bmatrix}$$

$$\boldsymbol{\Sigma}^*_M = \begin{bmatrix} -411.2119 & 470.7256 \\ 503.3228 & -339.2192 \end{bmatrix}, \begin{bmatrix} -397.4095 & 535.3143 \\ 495.8422 & -375.1100 \end{bmatrix}$$

Figure 4.14: Deformed microscopic RVEs with material forces and corresponding macroscopic Eshelby stress tensors in [N/mm^2]

In a next step, the influence of RVEs is studied which result in inclined macroscopic crack tip forces. To this end, two RVEs containing a diagonal interface are studied, see Figure 4.15 for the setting.

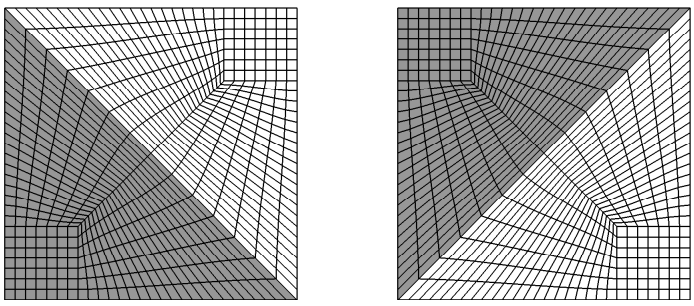

Figure 4.15: Undeformed microscopic structures with diagonal interfaces

In order to obtain a significant vertical contribution in the macroscopic crack tip force the stiffness ratio of the microscopic materials is increased to five, i.e., one material is five times stiffer than the other one. In detail the material parameters are chosen as $E_1 = 500$ N/mm^2, $E_2 = 2500$ N/mm^2 and $\nu_1 = \nu_2 = 0.3$. The deformed macroscopic structures under prescribed displacements in longitudinal direction and the values of the crack tip forces are depicted in Figure 4.16. A comparison of the crack tip forces which result from the different orientation of the microscopic interface yields that for both approaches the absolute value of the crack tip force has the same value for the original and the rotated RVE.

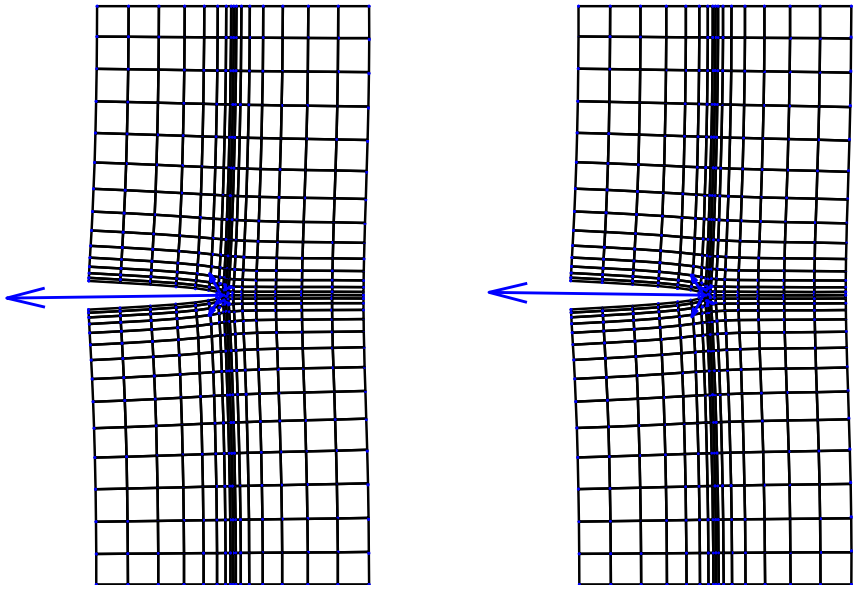

$$\mathfrak{F}_M = \begin{bmatrix} -7.9277 \\ -0.1047 \end{bmatrix}, \quad \begin{bmatrix} -7.9277 \\ 0.1047 \end{bmatrix}$$

$$\mathfrak{F}^*_M = \begin{bmatrix} -8.4775 \\ -0.2493 \end{bmatrix}, \quad \begin{bmatrix} -8.4775 \\ 0.2493 \end{bmatrix}$$

Figure 4.16: Deformed macroscopic structures with underlying RVEs with diagonal interfaces and corresponding material crack tip force in [N]

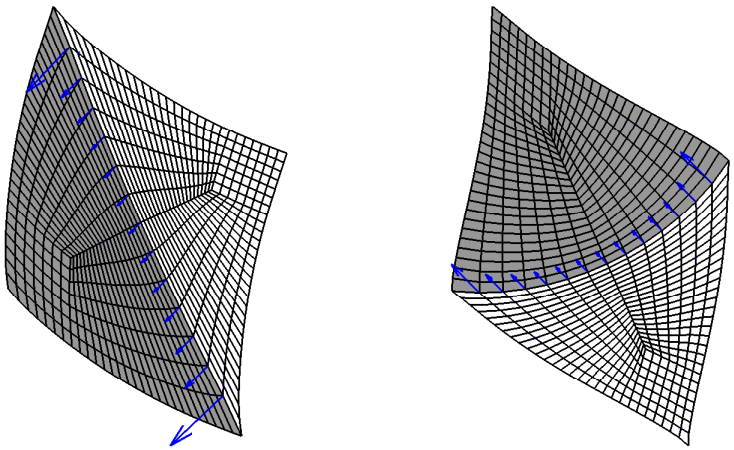

$$\Sigma_M = \begin{bmatrix} -372.2337 & 403.6889 \\ 403.6889 & -443.0810 \end{bmatrix}, \quad \begin{bmatrix} -352.2525 & 360.1769 \\ 360.1769 & -390.4695 \end{bmatrix}$$

$$\Sigma^*_M = \begin{bmatrix} -378.6228 & 436.0026 \\ 437.4691 & -454.0842 \end{bmatrix}, \quad \begin{bmatrix} -360.4196 & 396.9264 \\ 394.5981 & -399.5203 \end{bmatrix}$$

Figure 4.17: Deformed microscopic RVEs with material forces and corresponding macroscopic Eshelby stress tensors in [N/mm^2]

In both approaches the rotation of the RVE leads to a change of sign in the vertical part of the crack tip force. The approach based on averaged spatial quantities results in a greater material force, especially the influence of the vertical contribution of the material force is considerable. Finally, the Eshelby stresses at a macroscopic simulation point near the crack tip are compared, see Figure 4.17 Although the macroscopic crack tip forces have the same absolute value for both RVEs the corresponding Eshelby stresses differ. For the diagonal interface as displayed on the right-hand side, the Eshelby stresses of both approaches are smaller than for the other RVE. Furthermore, it is observed that the direct approach yields bigger macroscopic Eshelby stresses than the approach based on the average Eshelby stress. This fact also leads to the bigger material crack tip forces within the direct approach.

Influence of Micro-Structure onto Macroscopic Material Response –Stiffness Ratio

In a last example the influence of the microscopic stiffness ratio onto the macroscopic crack tip forces is studied. Therefore, different RVEs with a horizontal interface, as displayed in the left-hand side of Figure 4.12, are studied. In all contemplated RVEs the averaged Young's modulus $\bar{E} := \frac{E_1+E_2}{2} = 300$ N/mm^2 is the same, but the stiffness ratio between the materials, which is given by $R = \dfrac{E_1}{E_2}$ differs. For both materials the Poisson's ratio is chosen as $\nu_1 = \nu_2 = 0.3$. Firstly displacements in longitudinal direction are prescribed at the macro-scale. In Figure 4.18 the macroscopic longitudinal Cauchy stresses and the crack tip forces are displayed for underlying RVEs with different stiffness ratios.
In this Figure it is observed that for an increasing stiffness ratio the Cauchy stresses in longitudinal direction decrease, i.e., the macroscopic material yields a softer response. This response also influences the material crack tip force, which also decreases with an increasing difference in the microscopic stiffnesses. Thus, the softer macroscopic material response yields a smaller crack tip force. This tendency is also depicted at the left-hand side of Figure 4.20 which monitors the relation between the macroscopic crack tip force and the microscopic stiffness ratio for the approach based on the averaged Eshelby stress tensor. The material crack tip force reveals a steeper descent in the beginning of an increasing stiffness ratio than at the end of the displayed diagram.

In a second step the influence of the microscopic stiffness ratio onto the macroscopic crack tip forces is studied for applied traction on the macroscopic boundary. Figure 4.19 reveals that for this loading case the macroscopic Cauchy stresses in longitudinal direction have a similar dimension for the different underlying RVEs. However, the resulting macroscopic crack tip forces differ remarkably. This observation is also illustrated at the right-hand side of Figure 4.20 wherein the macroscopic crack tip forces and the stiffness ratio of the RVE are confronted.

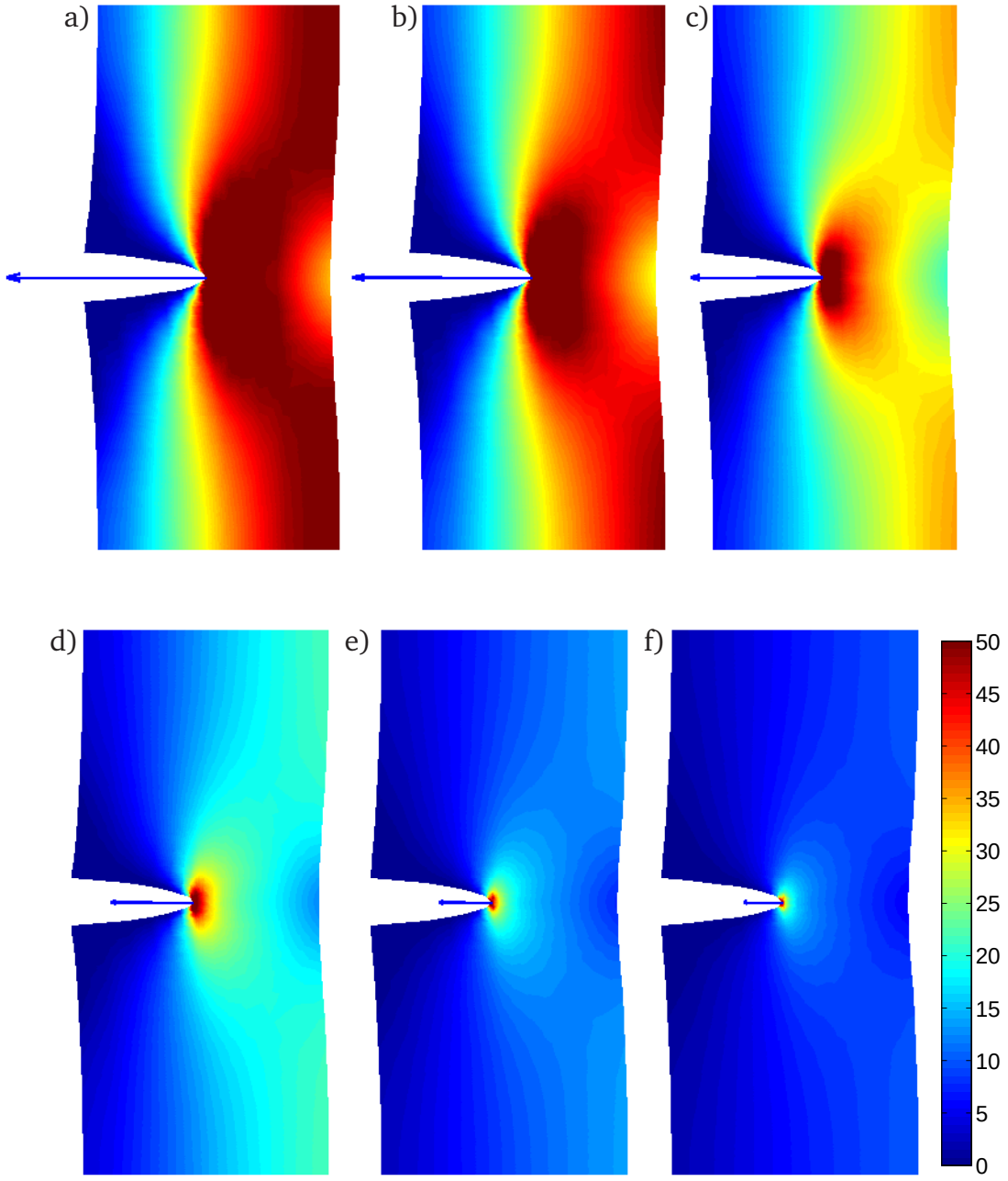

Figure 4.18: Macroscopic longitudinal Cauchy stresses in [N/mm^2] and material crack tip forces for underlying RVE with a horizontal interface and stiffness ratios a) $R = 1$, b) $R = 2$, c) $R = 4$, d) $R = 8$, e) $R = 14$, f) $R = 20$

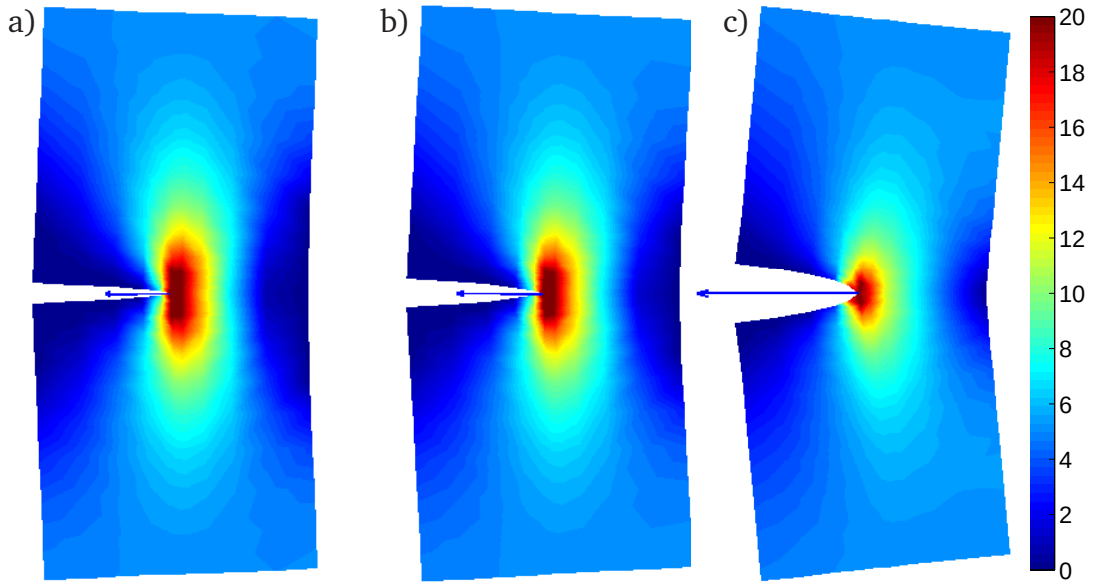

Figure 4.19: Macroscopic longitudinal Cauchy stresses in [N/mm^2] and material crack tip forces for underlying RVE with a horizontal interface and stiffness ratios a) $R = 1$, b) $R = 4$, c) $R = 20$

For the applied traction loading the macroscopic crack tip forces increase for an increasing stiffness ratio at the macro-scale. This increase shows that in case of a more heterogeneous micro-structure a prescribed macroscopic crack shows a tendency to propagate prior than in case of a more homogeneous structure. Thus, it is illustrated that also the grade of the microscopic heterogeneity influences the macroscopic crack tip force.

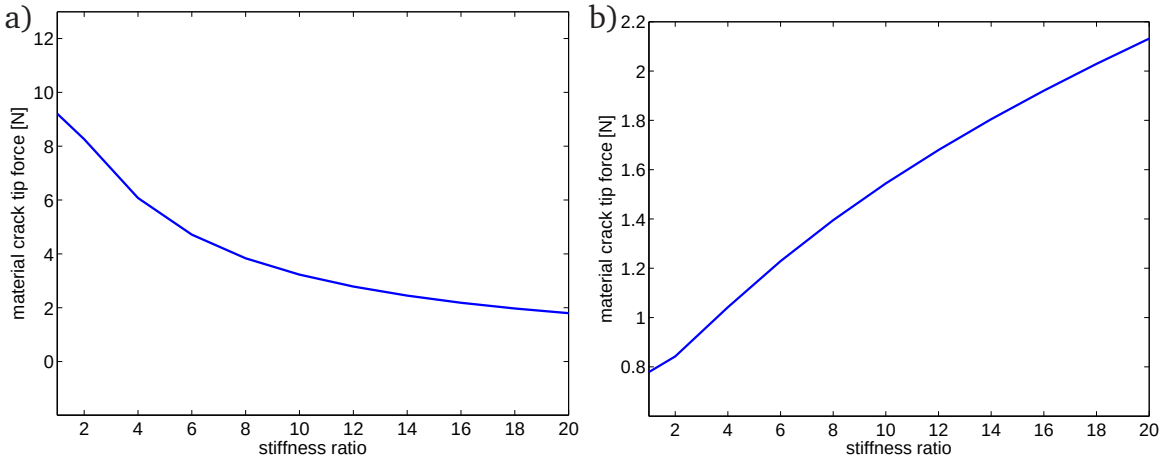

Figure 4.20: Connection between the macroscopic crack tip force and the microscopic stiffness ratio for a) applied macroscopic displacements and b) applied macroscopic tractions

4.4 Summary

In the previous section, an extension of the computational homogenization scheme towards the homogenization of material quantities, like the Eshelby stress and material node point forces, has been developed. Therefore, the averaged material quantities have been defined as appropriate averages over the boundary of the RVE. In contrast to the homogenization of spatial quantities here also interface integrals have to be incorporated even if the RVE does not contain discontinuities like cracks. These interface terms originate due to the discontinuous properties of material tractions. In a next step, the material scale-transition has been developed based on its spatial counterpart. Therefore, the validity of the Hill-Mandel condition and vanishing spatial volume force have been postulated. Although the spatial volume forces vanish, material volume forces may occur due to graded micro-materials. These also have been incorporated in the formulation of the material homogenization procedure. Based on the material and the spatial scale-transition, three different approaches for the homogenization have been compared.

Firstly, the most intuitive approach has been highlighted which is based on the direct calculation of the Eshelby stress in terms of homogenized material quantities. In the elaboration of the material Hill-Mandel type condition internal extra contributions were necessary for the special case of non-graded micro-materials as well as for graded materials, for both representations formulated in the Eshelby stress and in the material two-point stress. Therefore, further approaches have been discussed. In the second approach the macroscopic Eshelby stress tensor is defined as the averaged Eshelby stress tensor. This definition yields for the special case of a non-graded microscopic material in the formulation based on the primal variable, i.e., the Eshelby stress tensor, a consistent Hill-Madel type condition without the necessity of any internal contributions. However, if the Hill-Mandel type condition is regarded in terms of the dual variable, i.e., the material two-point stress, also internal extra terms are required. Nevertheless, this approach is favored due to the fact that the material forces are determined in terms of the (consistent) Eshelby stress and not in terms of the (inconsistent) two-point stress.

For the sake of completeness, also an approach based on the material two-point stress has been given. In this approach the material two-point stress represents the primal variable, i.e., the macroscopic two-point stress is defined as the averaged two-point stress. The dual variable which then corresponds to the Eshelby stress tensor is determined by means of a pull-back of the macroscopic two-point stress. Focusing on the Hill-Mandel type conditions for this approach showed that in all formulations extra terms are necessary also for the special case of a non-graded material. Thus, this approach does not yield a consistent manner to determine macroscopic material quantities and is not regarded in the numerical considerations.

In a next step, the material homogenization procedures has been illustrated by elucidating numerical examples. The resulting homogenized material quantities have been compared for the direct approach and the approach based on the av-

eraged Eshelby tensor. For all examples periodic boundary conditions have been applied. Firstly, a single RVE has been considered with a prescribed macroscopic deformation gradient. The representativeness of the material homogenization has been studied by considering different RVEs which represent the same microscopic structure with horizontal interfaces between different materials. In a next step, the two approaches have been compared with respect to their reflection of anisotropy. Therefore, for an RVE an isotropic St. Venant-Kirchhoff hyperelasticity has been compared to an anisotropic St. Venant-Kirchhoff law. In these considerations, it turned out that for the first one the averaged Eshelby stress tensor is symmetric, although the RVE yields an anisotropic response due to the asymmetric void. In contrast, for the anisotropic material law both approaches yield non-symmetric material responses.

Furthermore, full micro-macro transitions have been carried out to study the influence of different microscopic factors onto the macroscopic crack tip force. It has been shown that the orientation of voids as well as the orientation of interfaces yield different macroscopic crack tip forces. Within an example for a micro-structure which contains a diagonal interface it turned out that the rotation of the interface yields a change in the direction of the material crack tip force, whereby the magnitude of the horizontal and the vertical component remains the same. The only change is the switch in sign of the horizontal contribution. Focus has also been put onto the stiffness ratio between microscopic materials in the RVE which as well influences the macroscopic material response significantly.

Summing up, a novel extension of the computational homogenization scheme has been developed which allows the determination of macroscopic material quantities of interest for micro-structured materials. Thus, considerations like criteria for propagation of an existing crack can also be made for micro-heterogeneous materials within the material force method. Numerically, the presented scheme is very efficient because it can be carried out as a post-processing step of the standard FE^2 scheme.

However, the choice of the correct approach for the determination of the macroscopic Eshelby stress tensor is a rather delicate task. On the one hand, the approach based on homogenized spatial quantities is able to reflect anisotropic effects which are emerging from the microscopic geometry as well as effects stemming from anisotropic constitutive laws. In contrast, the approach based on the averaged Eshelby stress tensor only captures anisotropic material responses if the microscopic material law is anisotropic. For an isotropic material law the averaging process is carried out in terms of a symmetric microscopic Eshelby stress tensor and thus the macroscopic Eshelby stress also renders symmetric, which is an indicator for an isotropic behavior. Thus, anisotropic effects stemming from the microscopic setting cannot be observed within this approach. On the other hand, the approach based on the average of the Eshelby tensor fulfills the Hill-Mandel type condition in the special case of a non-graded microscopic material and thus is consistent with respect to the virtual work. In contrast, the direct approach does not satisfy the standard

Hill-Mandel type condition. Even for non-graded materials extra contributions need to be incorporated which depend on the gradient of the microscopic fluctuations. Numerical studies of these two approaches have shown that the obtained macroscopic material quantities differ quantitatively. However, both approaches reflected the same tendencies in the behavior of the material response. Thus, further studies on the different approaches are necessary in the future work.

5 On Variational Issues in the Homogenization of Particle Systems

In the sequel the (spatial) homogenization concept is formulated for discrete particle systems as, e.g,. represented by atomistic systems. Therefore, firstly the discrete kinematics are introduced and the principle of stationary potential energy is derived for unconstrained and Cauchy-Born constrained system. In contrast to the continuous homogenization, within the Cauchy-Born constraint not only the displacements of the boundary particles are prescribed but the actual position of the particles in the whole domain is fixed. For unconstrained and the constrained systems the averaging of variables is derived and within the concept of continuization, i.e., considerations of systems with an infinite number of particles, compared to the continuous homogenization. Furthermore, these concepts are illustrated by various numerical studies on the micro-level and within the macro-micro transition.

The current chapter is mainly based on the publications by Ricker et al. [71] and Steinmann et al. [84].

5.1 Unconstrained Particle Systems

5.1.1 Kinematics of Unconstrained Systems

In the following, particle systems consisting of a finite number N of particles α are considered. The particles are listed in the closed set $I_{\bar{\mathscr{C}}}$ which is partitioned into an open set $I_{\mathscr{C}}$ containing the list of particles α within the domain and the list $I_{\partial\mathscr{C}}$ of particles α situated at the boundary, such that $I_{\bar{\mathscr{C}}} = I_{\mathscr{C}} \cup I_{\partial\mathscr{C}}$ and $\emptyset = I_{\mathscr{C}} \cap I_{\partial\mathscr{C}}$. For each particle α the neighboring particles are captured in a neighbor list $I_{\mathscr{N}_\alpha}$. The number of interacting particles in the neighbor list depends on the assumed cut-off radius, which accounts, e.g., for next-neighbor or second-next neighbor interactions. The particles α listed in $I_{\bar{\mathscr{C}}}$ occupy the spatial and material positions $\mathbb{x}_\alpha$ and $\mathbb{X}_\alpha$. The spatial and material positions of all particles α listed in $I_{\bar{\mathscr{C}}}$ are assembled in the sets $\{\mathbb{x}_\gamma\}$ and $\{\mathbb{X}_\gamma\}$. They define the discrete spatial and material configurations $\bar{\mathscr{C}}_t$ and $\bar{\mathscr{C}}_0$ of the discrete system, respectively. To characterize the geometry of the discrete spatial and material configurations $\bar{\mathscr{C}}_t$ and $\bar{\mathscr{C}}_0$, additionally to the particle positions, the spatial and the material bond vectors are defined. They yield the

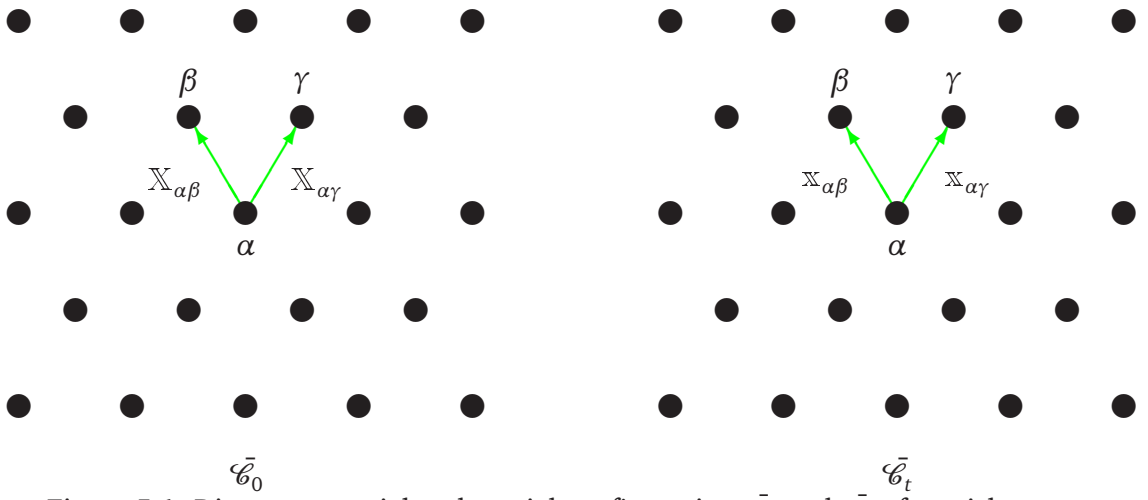

Figure 5.1: Discrete material and spatial configuration $\bar{\mathscr{C}}_0$ and $\bar{\mathscr{C}}_t$ of particle system

relative positions between two neighboring particles α and β via

$$\mathbb{x}_{\alpha\beta} = \mathbb{x}_\beta - \mathbb{x}_\alpha \quad \text{and} \quad \mathbb{X}_{\alpha\beta} = \mathbb{X}_\beta - \mathbb{X}_\alpha, \tag{5.1}$$

see Figure 5.1 for a schematic illustration. Since, in fact, it is the distance between two particles α and β that determines the contribution to the total potential energy of the system and, thus to the interaction force between the particles, it is convenient to introduce the corresponding spatial and material bond lengths

$$x_{\alpha\beta} = |\mathbb{x}_\beta - \mathbb{x}_\alpha| \quad \text{and} \quad X_{\alpha\beta} = |\mathbb{X}_\beta - \mathbb{X}_\alpha|. \tag{5.2}$$

With assistance of this bond length the spatial and material bond stretch can be defined as the corresponding ratios

$$\lambda_{\alpha\beta} = \frac{x_{\alpha\beta}}{X_{\alpha\beta}} \quad \text{and} \quad \Lambda_{\alpha\beta} = \frac{X_{\alpha\beta}}{x_{\alpha\beta}}. \tag{5.3}$$

Finally, the spatial and material bond directions are defined as unit vectors either from the gradient of the bond length with respect to the corresponding bond vector or simply by normalizing the bond vectors

$$\mathbb{n}_{\alpha\beta} = \frac{\partial x_{\alpha\beta}}{\partial \mathbb{x}_{\alpha\beta}} = \frac{\mathbb{x}_{\alpha\beta}}{x_{\alpha\beta}} \quad \text{and} \quad \mathbb{N}_{\alpha\beta} = \frac{\partial X_{\alpha\beta}}{\partial \mathbb{X}_{\alpha\beta}} = \frac{\mathbb{X}_{\alpha\beta}}{X_{\alpha\beta}}. \tag{5.4}$$

5.1.2 Principle of Stationary Potential Energy for Unconstrained Systems

In a next step, the principle of stationary potential energy is developed for the considered unconstrained particle systems. The potential energy E of such a particle system is given as a function of the set of spatial and material particle positions $\{\mathbb{x}_\gamma\}$

and $\{\mathbb{X}_\gamma\}$ as

$$E(\{\mathbb{x}_\gamma\};\{\mathbb{X}_\gamma\}) = \frac{1}{2}\sum_{\alpha\in I_{\mathscr{C}}}\sum_{\beta\in I_{\mathcal{N}_\alpha}} W^0_{\alpha\beta}(\lambda_{\alpha\beta})\,\mathbb{X}_{\alpha\beta} + \sum_{\alpha\in I_{\mathscr{C}}} V^{\mathscr{C}}_\alpha(\mathbb{x}_\alpha) + \sum_{\alpha\in I_{\partial\mathscr{C}}} V^{\partial\mathscr{C}}_\alpha(\mathbb{x}_\alpha). \tag{5.5}$$

Therein, $W^0_{\alpha\beta}$ corresponds to the internal bond (interaction) potential between two neighboring particles α and β per unit length of the material bond vector, whereas $V^{\mathscr{C}}_\alpha$ and $V^{\partial\mathscr{C}}_\alpha$ denote the external potential energies associated with particles in the interior or at the boundary of the domain, respectively. In analogy to the variational principles for continuous systems, the stationary condition for the total potential energy under spatial variations reads

$$\mathrm{D}_\delta E = 0 \quad \forall\ \mathrm{D}_\delta \mathbb{x}_\gamma, \tag{5.6}$$

wherein $\mathrm{D}_\delta(\bullet)$ denotes the spatial variation at fixed material particle positions $\mathbb{X}$. In more detail the variation of the total potential energy results in

$$\mathrm{D}_\delta E = \frac{1}{2}\sum_{\alpha\in I_{\mathscr{C}}}\sum_{\beta\in I_{\mathcal{N}_\alpha}} \mathrm{D}_\delta \mathbb{x}_{\alpha\beta}\cdot\frac{\partial W^0_{\alpha\beta}}{\partial\lambda_{\alpha\beta}}\,\mathbb{n}_{\alpha\beta} + \sum_{\alpha\in I_{\mathscr{C}}} \mathrm{D}_\delta \mathbb{x}_\alpha\cdot\frac{\partial V^{\mathscr{C}}_\alpha}{\partial \mathbb{x}_\alpha} + \sum_{\alpha\in I_{\partial\mathscr{C}}} \mathrm{D}_\delta \mathbb{x}_\alpha\cdot\frac{\partial V^{\partial\mathscr{C}}_\alpha}{\partial \mathbb{x}_\alpha} = 0\ \forall\ \mathrm{D}_\delta\mathbb{x}_\gamma. \tag{5.7}$$

In this equation the spatial interaction forces $\mathbb{k}_{\alpha\beta}$ and the external forces $\mathbb{k}^{\mathscr{C}}_\alpha$ and $\mathbb{k}^{\partial\mathscr{C}}_\alpha$ in the domain and the boundary can be identified as

$$\mathbb{k}_{\alpha\beta} := \frac{\partial W^0_{\alpha\beta}}{\partial\lambda_{\alpha\beta}}\,\mathbb{n}_{\alpha\beta} \quad \text{and} \quad \mathbb{k}^{\mathscr{C}}_\alpha := -\frac{\partial V^{\mathscr{C}}_\alpha}{\partial \mathbb{x}_\alpha} \quad \text{and} \quad \mathbb{k}^{\partial\mathscr{C}}_\alpha := -\frac{\partial V^{\partial\mathscr{C}}_\alpha}{\partial \mathbb{x}_\alpha}. \tag{5.8}$$

Thus, the stationary condition for the total potential energy E is equivalent to the local, i.e. particle-wise, deformational equilibrium conditions. That is in the interior of the domain

$$\mathbb{k}^{\mathscr{C}}_\alpha - \sum_{\beta\in I_{\mathcal{N}_\alpha}} \mathbb{k}_{\alpha\beta} \doteq \mathbb{0} \tag{5.9}$$

has to hold for all particles $\alpha\in I_{\mathscr{C}}$, whereas for all boundary particles $\alpha\in I_{\partial\mathscr{C}}$

$$\mathbb{k}^{\partial\mathscr{C}}_\alpha - \sum_{\beta\in I_{\mathcal{N}_\alpha}} \mathbb{k}_{\alpha\beta} \doteq \mathbb{0} \tag{5.10}$$

has to be fulfilled. Recapitulary, equations (5.9) and (5.10) state that all external and internal interaction forces at a particle α form an equilibrated force system.

Remark 7 *Example: Lennard Jones Potential*

As an example for an internal bond (interaction) potential, the Lennard Jones potential is mentioned. Here it is given in terms of the spatial bond length $x_{\alpha\beta}$ and two material parameters σ and ϵ as

$$\phi_{\alpha\beta}(x_{\alpha\beta}) = 4\epsilon \left[[\sigma/x_{\alpha\beta}]^{12} - [\sigma/x_{\alpha\beta}]^{6} \right]. \tag{5.11}$$

This potential can be applied to model the interaction between uncharged and not chemically connected atoms, and therefore contains a repulsion and an attraction term according to the interatomic distance. The material parameter ϵ characterizes the

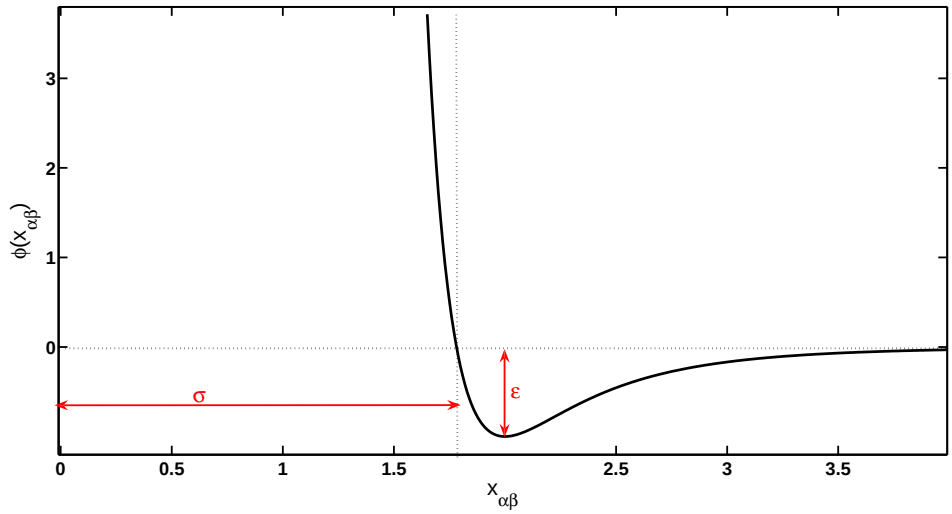

Figure 5.2: Lennard Jones Potential

potential depth and σ the spatial bond length, as illustrated in Figure 5.2. According to the notation used in the work at hand, the Lennard Jones potential is reformulated as an energy density per unit length of the material bond vector (that is $W^0_{\alpha\beta} = \phi_{\alpha\beta}/X_{\alpha\beta}$) and re-parametrized in terms of the spatial bond stretches, i.e.

$$W^0_{\alpha\beta}(\lambda_{\alpha\beta}) = 4\epsilon_0 \left[[\sigma_0/\lambda_{\alpha\beta}]^{12} - [\sigma_0/\lambda_{\alpha\beta}]^{6} \right]. \tag{5.12}$$

Thus, the material parameters per unit length are obtained via $\epsilon_0 := \epsilon/X_{\alpha\beta}$, $\sigma_0 := \sigma/X_{\alpha\beta}$. Consequently, the spatial interaction forces $\mathbb{k}_{\alpha\beta}$ result in

$$\mathbb{k}_{\alpha\beta} = -4\frac{\epsilon_0}{\lambda_{\alpha\beta}} \left[12[\sigma_0/\lambda_{\alpha\beta}]^{12} - 6[\sigma_0/\lambda_{\alpha\beta}]^{6} \right] \mathbb{n}_{\alpha\beta}. \tag{5.13}$$

Obviously, the equilibrium distance and stretch between isolated atoms α and β is given by $[x_{\alpha\beta}/\sigma]^6 = [\lambda_{\alpha\beta}/\sigma_0]^6 = 2$.

5.2 Cauchy-Born Constrained Particle Systems

In the following section Cauchy-Born restricted particle systems are considered. Thereby, discrete analogues to continuous stress measures are elaborated and a discrete averaging is defined. Furthermore, a continuization is carried out, i.e., discrete variables in systems with an infinite number of particles are contemplated and compared to their continuous counterparts.

5.2.1 Kinematics of Cauchy-Born Constrained Systems

In Cauchy-Born restricted systems it holds, at least in a local neighborhood containing the cut-off radius of particle α, that the spatial bond vectors $\mathbb{x}_{\alpha\beta}$ follow from a linear spatial map of the corresponding material bond vectors $\mathbb{X}_{\alpha\beta}$, i.e., it holds

$$\mathbb{x}_{\alpha\beta} = \mathbb{F}_\alpha \cdot \mathbb{X}_{\alpha\beta}. \tag{5.14}$$

Details on the Cauchy-Born rule can be found, e.g., in the textbook by Born and Huang [7], or in the publications by Ericksen [14], Zanzotto [96], Friesecke and Theil [22] and Sunyk and Steinmann [88]. An extension of the first order Cauchy-Born rule to the second order Cauchy-Born rule, which additionally incorporates a quadratic map in terms of the material bond vectors can be found in the work of Sunyk and Steinmann [87].

By assuming that the linear spatial map $\mathbb{F}_\alpha$ (which in the continuous case corresponds to the deformation gradient $\boldsymbol{F}$) is invertible, also the inverse relation of (5.14) can be obtained in terms of $\mathbb{f}_\alpha := \mathbb{F}_\alpha^{-1}$ (which in the continuous case corresponds to the inverse deformation gradient $\boldsymbol{f}$) as

$$\mathbb{X}_{\alpha\beta} = \mathbb{f}_\alpha \cdot \mathbb{x}_{\alpha\beta}. \tag{5.15}$$

With assistance of $\mathbb{I}_\alpha^\delta := \mathrm{D}_\delta \mathbb{F}_\alpha \cdot \mathbb{f}_\alpha$ (which corresponds in continuous problems to the spatial gradient of the variation of deformation, i.e., $\boldsymbol{l}^\delta := \operatorname{grad} \mathrm{D}_\delta \boldsymbol{\varphi}$) the variation of the spatial bond vectors $\mathbb{x}_{\alpha\beta}$ at fixed material positions are obtained via

$$\mathrm{D}_\delta \mathbb{x}_{\alpha\beta} =: \mathbb{I}_\alpha^\delta \cdot \mathbb{F}_\alpha \cdot \mathbb{X}_{\alpha\beta} = \mathbb{I}_\alpha^\delta \cdot \mathbb{x}_{\alpha\beta}. \tag{5.16}$$

In an analogous manner, by definition of $\mathbb{L}_\alpha^\delta := \mathrm{d}_\delta \mathbb{f}_\alpha \cdot \mathbb{F}_\alpha$ the variation of the material bond vectors $\mathbb{X}_{\alpha\beta}$ at fixed spatial positions are given by

$$\mathrm{d}_\delta \mathbb{X}_{\alpha\beta} =: \mathbb{L}_\alpha^\delta \cdot \mathbb{f}_\alpha \cdot \mathbb{x}_{\alpha\beta} = \mathbb{L}_\alpha^\delta \cdot \mathbb{X}_{\alpha\beta}. \tag{5.17}$$

Based on the linear spatial map $\mathbb{F}_\alpha$ the spatial bond map $\mathbb{F}_{\alpha\beta}$ is defined as

$$\mathbb{F}_{\alpha\beta} := \lambda_{\alpha\beta} \mathbb{n}_{\alpha\beta} \otimes \mathbb{N}_{\alpha\beta} = \mathbb{F}_\alpha \cdot [\mathbb{N}_{\alpha\beta} \otimes \mathbb{N}_{\alpha\beta}] = \mathbb{F}_\alpha \cdot \mathbb{I}_{\alpha\beta}, \tag{5.18}$$

and thus

$$\mathbb{x}_{\alpha\beta} = \mathbb{F}_{\alpha\beta} \cdot \mathbb{X}_{\alpha\beta}, \tag{5.19}$$

is valid between the spatial and the material bond vectors. Thereby, in the definition given above $\mathbb{I}_{\alpha\beta} := \mathbb{N}_{\alpha\beta} \otimes \mathbb{N}_{\alpha\beta}$ denotes the material bond unit tensor. Please note, that the spatial bond map $\mathbb{F}_{\alpha\beta}$ as well as the material bond unit tensor $\mathbb{I}_{\alpha\beta}$ are singular.

5.2.2 Principle of Stationary Potential Energy for Cauchy-Born Constrained Systems

In a next step, the stationary condition for the total potential energy is stated for first order Cauchy-Born constrained systems. Furthermore, the continuum limit of such systems is considered, i.e., systems with a number of particles tending to infinity are regarded. The application of the Cauchy-Born rule (5.14) to the stationary condition for the total potential energy (5.7) yields

$$\frac{1}{2} \sum_{\alpha \in I_{\bar{\mathscr{C}}}} \sum_{\beta \in I_{\mathcal{N}_\alpha}} [\mathrm{D}_\delta \mathbb{F}_\alpha \cdot \mathbb{X}_{\alpha\beta}] \cdot \mathbb{k}_{\alpha\beta} = \sum_{\alpha \in I_{\mathscr{C}}} \mathrm{D}_\delta \mathbb{x}_\alpha \cdot \mathbb{k}_\alpha^{\mathscr{C}} + \sum_{\alpha \in I_{\partial\mathscr{C}}} \mathrm{D}_\delta \mathbb{x}_\alpha \cdot \mathbb{k}_\alpha^{\partial\mathscr{C}} \quad \forall\, \mathrm{D}_\delta \mathbb{x}_\gamma. \tag{5.20}$$

Then, the discrete analogues to continuous stress measures are defined. Firstly, the

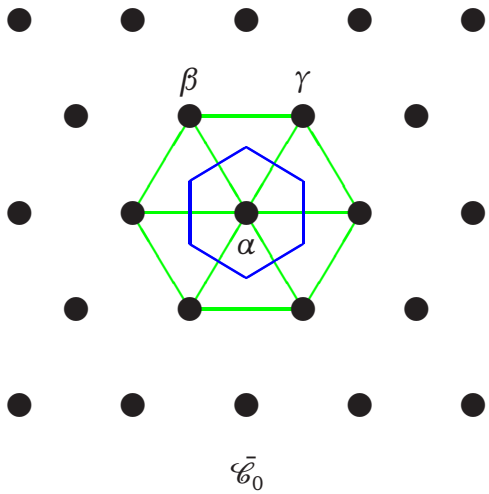

Figure 5.3: Material Delaunay tessellation and corresponding Voronoï polytope associated with the particle α

discrete Piola stress $\mathbb{P}_\alpha$ is defined in the Cauchy-Born format as

$$\mathbb{P}_\alpha := \frac{1}{V_\alpha} \sum_{\beta \in I_{\mathcal{N}_\alpha}} \mathbb{P}_{\alpha\beta} \quad \text{with} \quad \mathbb{P}_{\alpha\beta} = \frac{1}{2} \mathbb{k}_{\alpha\beta} \otimes \mathbb{X}_{\alpha\beta}. \tag{5.21}$$

Therein, V_α denotes the volume of the material Voronoï polytope associated with the particle α, as illustrated in Figure 5.3. Secondly, the discrete Cauchy stress in

Cauchy-Born format is given as

$$\mathbb{s}_\alpha := \frac{1}{v_\alpha} \sum_{\beta \in I_{\mathcal{N}_\alpha}} \mathbb{s}_{\alpha\beta} \quad \text{with} \quad \mathbb{s}_{\alpha\beta} = \frac{1}{2} \mathbb{k}_{\alpha\beta} \otimes \mathbb{x}_{\alpha\beta}, \tag{5.22}$$

where v_α denotes the volume of the spatial Voronoï polytope associated with the particle α. With this definition, the stationary condition for the total potential energy can be reformulated as

$$\sum_{\alpha \in I_{\mathscr{C}}} \mathrm{D}_\delta \mathbb{F}_\alpha : \mathbb{P}_\alpha V_\alpha = \sum_{\alpha \in I_{\mathscr{C}}} \mathrm{D}_\delta \mathbb{x}_\alpha \cdot \left[\frac{\mathbb{k}_\alpha^{\mathscr{C}}}{V_\alpha} \right] V_\alpha + \sum_{\alpha \in I_{\partial \mathscr{C}}} \mathrm{D}_\delta \mathbb{x}_\alpha \cdot \left[\frac{\mathbb{k}_\alpha^{\partial \mathscr{C}}}{A_\alpha} \right] A_\alpha \quad \forall\, \mathrm{D}_\delta \mathbb{x}_\gamma. \tag{5.23}$$

Thereby, A_α corresponds to the surface area of the material Voronoï polytope associated with the particle α as illustrated in Figure 5.3 by the blue line. Furthermore, the relation between the discrete Cauchy and Piola stress in Cauchy-Born format is given by

$$\mathbb{s}_\alpha = \frac{V_\alpha}{v_\alpha} \mathbb{P}_\alpha \cdot \mathbb{F}_\alpha^t. \tag{5.24}$$

By application of $\mathrm{D}_\delta F = \mathbb{I}_\alpha^\delta \cdot \mathbb{F}_\alpha$ and the relation between the discrete stress measures, the spatial virtual work equivalence

$$\mathrm{D}_\delta \mathbb{F}_\alpha : \mathbb{P}_\alpha V_\alpha \equiv \mathbb{I}_\alpha^\delta : \mathbb{s}_\alpha v_\alpha, \tag{5.25}$$

can be shown. Finally, insertion of the definition of the interaction forces into the definition of the discrete Cauchy stress yields

$$\begin{aligned} \mathbb{s}_\alpha &= \frac{1}{v_\alpha} \sum_{\beta \in I_{\mathcal{N}_\alpha}} \frac{1}{2} \mathbb{k}_{\alpha\beta} \otimes \mathbb{x}_{\alpha\beta} \\ &= \frac{1}{v_\alpha} \sum_{\beta \in I_{\mathcal{N}_\alpha}} \frac{1}{2} \frac{\partial W_{\alpha\beta}}{\partial \lambda_{\alpha\beta}} \mathbb{n}_{\alpha\beta} \otimes \mathbb{x}_{\alpha\beta} \\ &= \frac{1}{v_\alpha} \sum_{\beta \in I_{\mathcal{N}_\alpha}} \frac{1}{2x_{\alpha\beta}} \frac{\partial W_{\alpha\beta}}{\partial \lambda_{\alpha\beta}} \mathbb{x}_{\alpha\beta} \otimes \mathbb{x}_{\alpha\beta}, \end{aligned} \tag{5.26}$$

which results in the symmetry $\mathbb{s}_\alpha = \mathbb{s}_\alpha^t$.

5.2.3 Continuization for Cauchy-Born Constrained Systems

The continuum limit or continuization of the considered particle systems is obtained by letting the cardinality of the set I_α tend to infinity, i.e., $\#I_{\mathscr{C}} \to \infty$, while V_α and A_α tend to zero. This leads to an exchange of the sums over the particles α to integrals over the continuous configuration $\bar{\mathscr{B}}_0$, or $\mathscr{B}_0$ and the boundary $\partial \mathscr{B}_0$, respectively. Then, the variation of the spatial positions of a particle $\mathrm{D}_\delta \mathbb{x}_\alpha$ results in the variation of the spatial deformation map $\mathrm{D}_\delta \boldsymbol{\varphi}$ whereas the discrete external forces $\mathbb{k}_\alpha^{\mathscr{C}}$ per

volume V_α in the interior of the domain tend to the continuous volume forces $\boldsymbol{b}_0$. Thus, the first sum on the right-hand side of the discrete stationary condition for the total potential energy (5.23) results in

$$\lim_{\#I_{\mathscr{C}}\to\infty}\left(\sum_{\alpha\in I_{\mathscr{C}}} \mathrm{D}_\delta \mathbb{x}_\alpha \cdot \left[\frac{\mathbb{k}_\alpha^{\mathscr{C}}}{V_\alpha}\right] V_\alpha\right) = \int_{\mathscr{B}_0} \mathrm{D}_\delta \boldsymbol{\varphi} \cdot \boldsymbol{b}_0 \,\mathrm{d}V. \tag{5.27}$$

The discrete external forces at the boundary $\mathbb{k}_\alpha^{\partial\mathscr{C}}$ per area A_α tend to the boundary tractions $\boldsymbol{t}_0$ and therefore the continuum limits of the second sum on the right-hand side of (5.23) reads

$$\lim_{\#I_{\mathscr{C}}\to\infty}\left(\sum_{\alpha\in I_{\partial\mathscr{C}}} \mathrm{D}_\delta \mathbb{x}_\alpha \cdot \left[\frac{\mathbb{k}_\alpha^{\partial\mathscr{C}}}{A_\alpha}\right] A_\alpha\right) = \int_{\partial\mathscr{B}_0} \mathrm{D}_\delta \boldsymbol{\varphi} \cdot \boldsymbol{t}_0 \,\mathrm{d}A. \tag{5.28}$$

Finally, the discrete Piola stress tends to the continuous Piola stress and thus the continuous version of the right-hand side of (5.23) results in

$$\lim_{\#I_{\mathscr{C}}\to\infty}\left(\sum_{\alpha\in I_{\mathscr{C}}} \mathrm{D}_\delta \mathbb{F}_\alpha : \mathbb{P}_\alpha\right) = \int_{\tilde{\mathscr{B}}_0} \mathrm{D}_\delta \boldsymbol{F} : \boldsymbol{P} \,\mathrm{d}V. \tag{5.29}$$

Summarizing the continuum limit of the stationary condition of the total potential energy results in

$$\int_{\tilde{\mathscr{B}}_0} \mathrm{D}_\delta \boldsymbol{F} : \boldsymbol{P} \,\mathrm{d}V = \int_{\mathscr{B}_0} \mathrm{D}_\delta \boldsymbol{\varphi} \cdot \boldsymbol{b}_0 \,\mathrm{d}V + \int_{\partial\mathscr{B}_0} \mathrm{D}_\delta \boldsymbol{\varphi} \cdot \boldsymbol{t}_0 \,\mathrm{d}A \quad \forall\ \mathrm{D}_\delta \boldsymbol{\varphi}, \tag{5.30}$$

which corresponds to the standard formulation in continuum mechanics, compare (2.62).

5.3 Homogenization of Discrete Particle Systems

The averaging or homogenization process of discrete systems is carried out in analogy to the homogenization of spatial continuous systems, compare Section 3.1. Therefore, in the work at hand only the differences which appear due to the discrete character of the particles and the Cauchy-Born constraint are pointed out explicitly. No further focus is pointed onto virtual work consistency which is represented by the Hill-Mandel condition.

Firstly, the unconstrained particle systems are considered. For these systems the scale-transition from the macro- to the micro-level can be performed by admissible boundary conditions as, e.g., displacement or periodic boundary conditions, which have already been elaborated in Section 3.2. For the transition from the micro- to the

macro-level in the discrete homogenization the boundary integrals are substituted by sums over the associated boundaries. Thus, the averaging concepts remain the same and therefore only the average of the discrete Piola stress is explicitly given as

$$\bar{\mathbb{P}} := \frac{1}{V_0} \sum_{\alpha \in I_{\partial \mathscr{C}}} \mathbb{k}_\alpha^{\partial \mathscr{C}} \otimes \mathbb{X}_\alpha. \tag{5.31}$$

The continuum limit of this discrete averaged Piola stress results in

$$\lim_{\#I_{\mathscr{C}} \to \infty} \left(\frac{1}{V_0} \sum_{\alpha \in I_{\partial \mathscr{C}}} \mathbb{k}_\alpha^{\partial \mathscr{C}} \otimes \mathbb{X}_\alpha \right) = \frac{1}{V_0} \int_{\partial \mathscr{B}_0} \boldsymbol{t}_0 \otimes \boldsymbol{X} \, \mathrm{d}A, \tag{5.32}$$

compare (3.7). Due to this analogy in the formulation of the averaging of discrete and continuous quantities the required backgrounds as the average strain theorems and the virtual work equivalence as given in the Hill-Mandel condition are not stated in detail, here. These concepts have been already given in Section 3.1.

For the Cauchy-Born constraint systems the averaging in terms of the boundary is not appropriate due to the fact that the enforcement of all degrees of freedom results in internal forces. Therefore, the averaged Piola stress is defined by means of the discrete Piola stress at each particle as given in equation (5.21) and thus it holds

$$\bar{\mathbb{P}} := \frac{1}{V_0} \sum_{\alpha \in I_{\mathscr{C}}} \mathbb{P}_\alpha. \tag{5.33}$$

It can be shown that this definition of the averaged Cauchy stress fulfills the consistency criterion given by the Hill-Mandel condition. Further details to these considerations can be found in the thesis by Sunyk [86].

5.4 Numerical Examples -Particle Systems

In the following section the two approaches based on unconstrained particle systems and Cauchy-Born constrained systems are compared. To this end, basic particle systems are considered, which are characterized by next-neighbor interactions modeled as truss elements. Within the discrete homogenization concepts also atomistic simulations are possible, e.g., in term of the Lennard-Jones potential but these considerations extend the scope of the work at hand.

In all examples for the unconstrained systems the scale-transition from the macro- to the micro-level is performed according to periodic boundary conditions.

5.4.1 Microscopic Examples –Particle Systems

Firstly, only focus is put onto the averaged stresses which result from a single RVE. Therefore, a macroscopic deformation gradient is prescribed and applied to the RVE

in terms of periodic boundary conditions and the Cauchy-Born rule. In detail the applied deformation gradient reads

$$\boldsymbol{F}_M = \begin{bmatrix} 1.0 & 0.0 \\ 0.0 & 1.1 \end{bmatrix}. \tag{5.34}$$

This deformation gradient is applied to two different RVEs. An RVE consisting of a regular arrangement of particles is compared to an RVE with a point defect as illustrated in Figure 5.4.

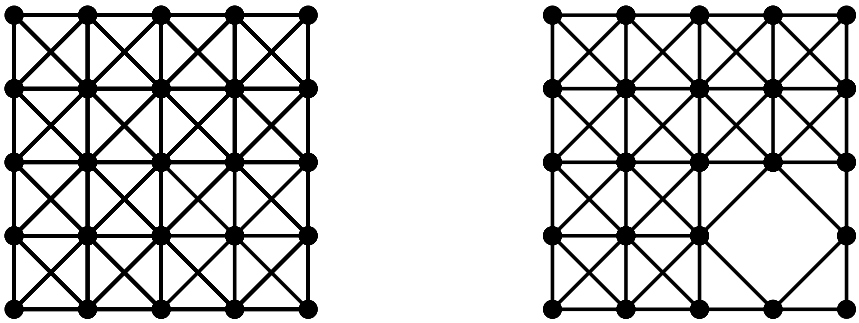

Figure 5.4: Undeformed setting of a regular particle system and a particle system disturbed by a point defect

In these simulations, the advantage of the Cauchy-Born constrained systems is that no microscopic iterations steps need to be carried out within the Newton-Raphson scheme due to the fact that all particle positions are determined a-priori. Thus, the averaged stresses can be determined directly. The resulting stresses of these procedure are compared to the stresses resulting from the periodic boundary conditions.

Firstly, a Neo-Hookean material according to Section 2.3.1 is assumed for the connecting truss elements. The corresponding Young's modulus is chosen as $E = 500$ [N/mm^2]. Then, for the regular structure the averaged Piola stresses result in

$$\bar{\mathbb{P}}^{\text{CB}} = \begin{bmatrix} 33.596 & 0 \\ 0 & 96.6142 \end{bmatrix} [\text{N/mm}^2]; \quad \bar{\mathbb{P}}^{\text{peri}} = \begin{bmatrix} 33.596 & 0 \\ 0 & 96.6142 \end{bmatrix} [\text{N/mm}^2]. \tag{5.35}$$

For the RVE containing the point defect the averaged stresses read

$$\bar{\mathbb{P}}^{\text{CB}} = \begin{bmatrix} 29.3961 & 0 \\ 0 & 86.0289 \end{bmatrix} [\text{N/mm}^2]; \quad \bar{\mathbb{P}}^{\text{peri}} = \begin{bmatrix} 29.3080 & 0.0085 \\ 0.0094 & 82.7194 \end{bmatrix} [\text{N/mm}^2]. \tag{5.36}$$

A comparison of these stress values yields that in case of a regular micro-structure the Cauchy-Born constrained approach and the periodic boundary conditions yields the same stresses. In the case of the RVE with the point defect both approaches yield smaller stresses which corresponds to a softer material response. In contrast to the Cauchy-Born approach, the periodic conditions yield a smaller stress response. Due to the remaining degrees of freedom also shear stresses occur for this approach. These observations are summarized in the stress-stretch relation in longitudinal direction as displayed in Figure 5.5.

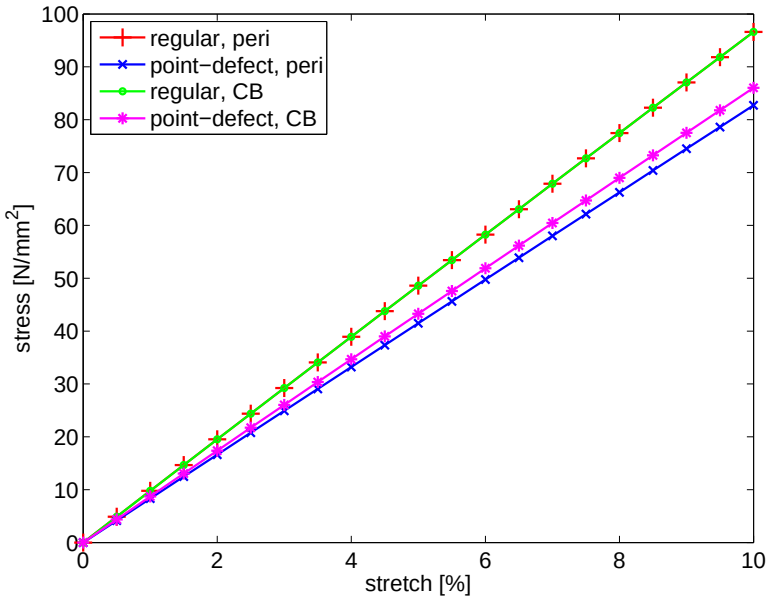

Figure 5.5: Stress-stretch relation in longitudinal direction for Neo-Hookean material

In a second example the same RVEs are considered but additionally a damage formulation is coupled to the Neo-Hookean material behavior according to Section 2.3.3. The material parameter which influences the damage is given as $H = 0.1675$ whereas the threshold of energy for the initiation of damage $U = 0.01$. Similar to the pure Neo-Hooke hyperelasticity for the regular structure both approaches yield the same averaged stresses and also the maximal damage parameter in the micro-trusses reads the same

$$\bar{\mathbb{P}}^{\mathrm{CB}} = \bar{\mathbb{P}}^{\mathrm{peri}} = \begin{bmatrix} 30.2091 & 0 \\ 0 & 73.0576 \end{bmatrix} \ [\mathrm{N/mm^2}] \text{ and } \max(d^{\mathrm{CB}}) = \max(d^{\mathrm{peri}}) = 0.3324. \tag{5.37}$$

For the RVE with the point defect the stresses result differently, i.e., it holds

$$\bar{\mathbb{P}}^{\mathrm{CB}} = \begin{bmatrix} 26.4330 & 0 \\ 0 & 64.9211 \end{bmatrix} \ [\mathrm{N/mm^2}] \quad \text{and} \quad \max(d^{\mathrm{CB}}) = 0.3324, \tag{5.38}$$

and

$$\bar{\mathbb{P}}^{\text{peri}} = \begin{bmatrix} 20.8432 & 1.3614 \\ 1.4975 & 41.1295 \end{bmatrix} \text{[N/mm}^2\text{]} \quad \text{and} \quad \max(d^{\text{peri}}) = 0.9998. \tag{5.39}$$

A comparison of these averaged stress values to the stress values (5.35), (5.36) of the pure Neo-Hookean material yields that due to the damage the stresses are smaller, i.e., the material becomes softer. For the point defect both approaches also yield a softer response as for the regular RVE and once more the Cauchy-Born rule yields a stiffer response than the periodic boundary condition.

The comparison of the different stresses in longitudinal direction is illustrated in Figure 5.6.

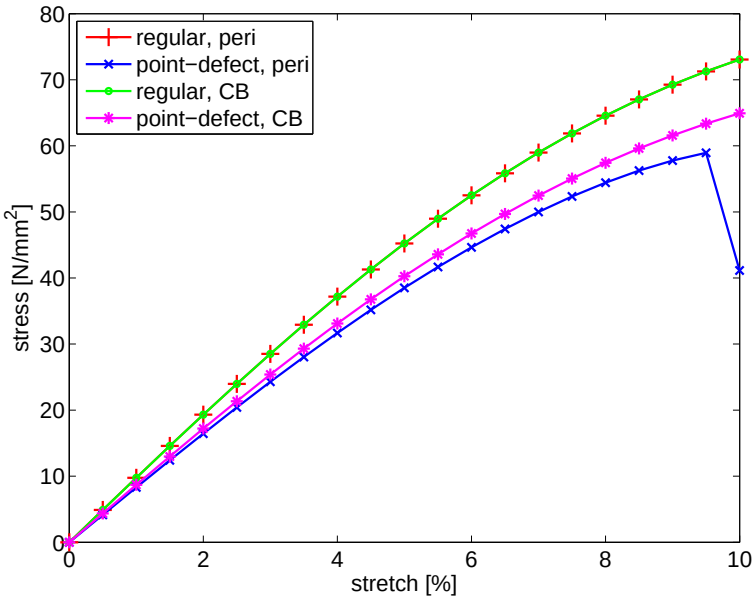

Figure 5.6: Stress-stretch relation in longitudinal direction for Neo-Hookean material coupled to damage

Furthermore, a comparison of the maximal damage parameters yields that the Cauchy-Born rule results for both structures in $\max(d^{\text{CB}}) = 0.3324$ whereas for the periodic boundary conditions almost rupture ($\max(d^{\text{peri}}) = 0.9998$) is obtained. This large damage parameter is also observed by the kink in the corresponding curve in Figure 5.6. The distribution of damage in the different structures is given in Figure 5.7. On the one hand it is observed that the Cauchy-Born rule leads to a homogeneous distribution of damage for the regular structure as well as for the RVE containing a point defect. On the other hand an inhomogeneous damage distribution is observed in case of an inhomogeneous RVE under periodic boundary conditions.

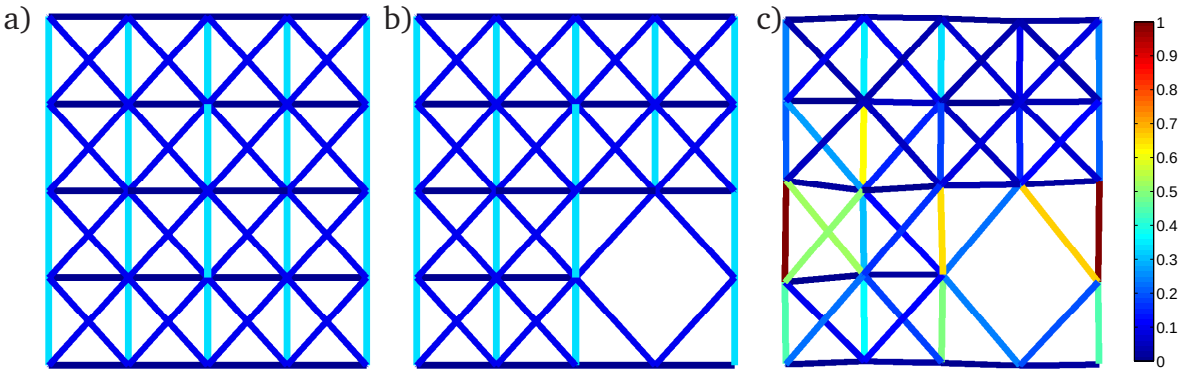

Figure 5.7: Distribution of damage parameter for a) Cauchy-Born rule as well as periodic boundary conditions, b) Cauchy-Born rule and c) periodic boundary conditions

5.4.2 Macro-Micro Transition –Particle Systems

In a next example the influence of different RVE and the different approaches for the scale-transition onto a macroscopic structure is studied. At the macro-level a rectangular specimen with a centered hole is studied. For this structure displacements in longitudinal direction are applied. At the micro-scale the regular RVE and the RVE with point defect as already illustrated in Figure 5.4 are compared. A Neo-Hooke type material is assumed in the RVE and the Young's modulus is chosen as $E = 100$ [N/mm^2]. In Figure 5.8 the longitudinal Cauchy stresses are displayed for different scale-transitions and different RVEs.

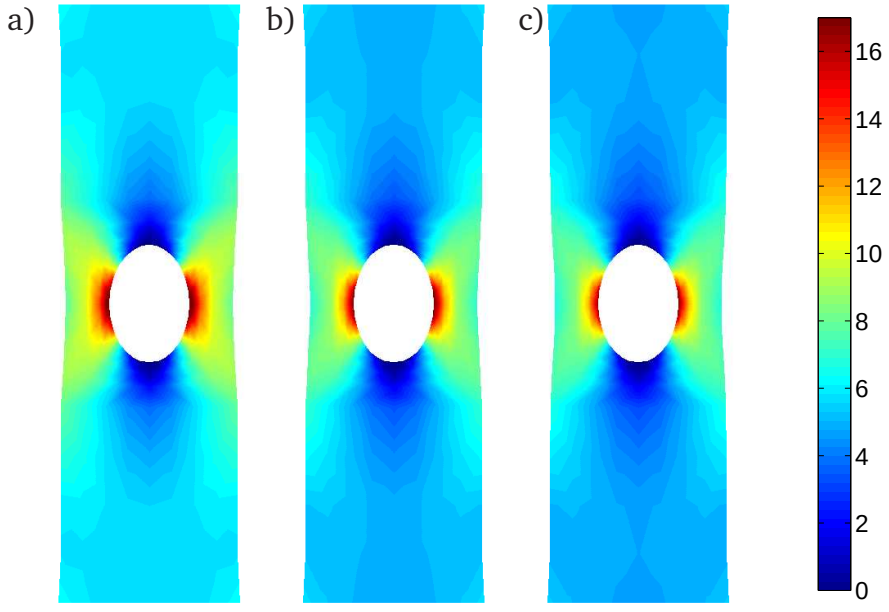

Figure 5.8: Macroscopic longitudinal Cauchy stresses in [N/mm^2] for underlying a) regular RVE, b) RVE with point defect constrained by Cauchy-Born rule and c) RVE with point defect under periodic boundary conditions

For the underlying regular RVE only one stress plot is given due to the fact that the Cauchy-Born restricted systems result in the same material response as the systems under periodic boundary conditions. Furthermore, in analogy to the microscopic considerations, these stress plots reveal that both approaches yield softer results for the RVE containing a point defect. In this case, again the response of the Cauchy-Born constrained systems yields a slightly stiffer material behavior than the periodic boundary conditions.

5.5 Summary

In the previous section the computational homogenization of particle systems has been elaborated. Therefore, two concepts for the transition from the macro- to the micro-scale have been compared. On the one hand unconstrained systems have been introduced for which standard boundary conditions may be applied. On the other hand the systems have been constrained by the first-order Cauchy-Born rule, which basically prescribes the actual position of all particles. For both concepts, the averaging of variables has been introduced and illustrated numerically. For homogeneous micro-structures both approaches yield the same material response whereas for inhomogeneous structures as, e.g., RVE with defects, the Cauchy-Born response is stiffer. Due to the fact the Cauchy-Born rule does not require an iterative solution procedure within the Newton-Raphson scheme, it yields a numerically effective method to determine averaged quantities for homogeneous micro-structures. The Cauchy-Born constrained systems also provide a method to approximate average quantities efficiently. Further details on the Cauchy-Born formulation as, e.g., the configurational framework and second-order formulations are given in the work of Steinmann et al. [84].

6 Conclusion and Future Work

In the work at hand, extensions of the standard computational homogenization scheme have been developed. Firstly, the concept of the computational homogenization scheme has been introduced and illustrated by various numerical examples. Secondly, focus has been put onto the homogenization of material quantities like the Eshelby stress tensor, which can be applied to calculate material node point forces. These node point forces are of great interest, as it can be shown that the material force at a crack tip corresponds to the J-integral and thus yields a criterion for crack propagation.

To this end, different approaches for the determination of the macroscopic Eshelby stress tensor have been compared. A direct approach which determines the Eshelby stress by means of homogenized spatial variables and approaches based on averaging the Eshelby stresses, similar as in the spatial homogenization, have been developed. Focus has been put onto Hill-Mandel type conditions in order to check the consistency of the considered approaches with respect to the virtual work. Therein, two cases are distinguished: At the micro-level graded and non-graded materials are regarded. In the special case of a non-graded material the strain energy functional does not depend explicitly on the material position. For the more general case of graded materials, extra contributions, which depend on the explicit derivative of the stored energy with respect to the coordinates, emerge in the Hill-Mandel type condition for all approaches. If non-graded microscopic materials are considered the Eshelby stress based on averaging methods does not require any extra contribution, whereas the Eshelby stress obtained from the direct approach includes an extra term depending on the gradient of the macroscopic fluctuations. Thus, the direct approach is not virtual work consistent.

The differences in the material responses, which result from these two approaches, have been studied by a wide range of numerical examples. Within these examples, it also has been illustrated that the direct approach is able to capture anisotropic effects, which result from the microscopic geometry, by means of a non-symmetric macroscopic Eshelby stress tensor. On the contrary, the approach based on the average of the Eshelby stress only reflects anisotropic effects which stem from an anisotropic microscopic material law. This observation is reasonable due to the fact that for an isotropic micro-material the averaging process is carried out over isotropic, i.e., symmetric Eshelby stress tensors.

Therefore, the choice of an appropriate approach for the determination of the macroscopic Eshelby stress tensor based on the underlying microscopic structure remains a delicate task. Both considered approaches have their advantages and

disadvantages. Either the Eshelby stress is more sensitive with respect to the microscopic anisotropy and the Hill-Mandel type condition includes extra terms or the Hill-Mandel type condition is consistent in case of a non-graded micro-material but the anisotropy is not captured by means of non-symmetric Eshelby tensors. Thus, further studies on this topic are necessary in the future.

Furthermore, it remains to simulate RVEs which incorporate a continuous graded material. Likewise, the study of other heterogeneities as, e.g., microscopic cracks or macro-heterogeneous continua, i.e., continua for which different RVEs are attached to different simulation points, is still an area of further numerical analysis.

Another topic of the current work is the extension of the computational homogenization scheme towards the homogenization of discrete structures. Therefore, two approaches for the scale-transition have been compared. Unconstrained and Cauchy-Born constrained systems have been considered and compared within basic numerical examples. In the future work, these examples need to be extended towards the simulation of atomistic systems by means of interatomic potentials, as e.g., represented by the Lennard-Jones potential.

A Relation between Spatial and Material Volume Forces

In the following, the connection between the spatial and the material volume forces is elaborated. Starting point is the quasi-static balance of momentum, which yields the material volume force in terms of the Eshelby stress tensor via

$$\boldsymbol{B}_0 = -\mathrm{Div}\boldsymbol{\Sigma}. \tag{A.1}$$

Application of the connection between the material Eshelby stress and the spatial Piola stress –see equation (2.30)– yields

$$\begin{aligned} \boldsymbol{B}_0 &= -\mathrm{Div}\left(U_0\,\boldsymbol{I} - \boldsymbol{F}^t\cdot\boldsymbol{P}\right) &&= -U_{0,K} + \left(F_{Ki}\,P_{iJ}\right)_{,J} \\ &= -U_{0,K} + F_{Ki,J}\,P_{iJ} + F_{Ki}\,P_{iJ,J} &&= -\frac{\partial U_0}{\partial X_K} + P_{iJ}\,F_{iK,J} - F_{Ki}\,b_{0i}. \end{aligned} \tag{A.2}$$

Therein, the derivative of the energy density with respect to the material coordinates can be determined by the chain rule via

$$\frac{\partial U_0}{\partial X_K} = \frac{\partial U_0}{\partial F_{iJ}}\frac{\partial F_{iJ}}{\partial X_K} - \frac{\partial U_0}{\partial X_K}|_{\text{expl.}} = P_{iJ}\,F_{iJ,K} - \frac{\partial U_0}{\partial X_K}|_{\text{expl.}}. \tag{A.3}$$

In the second term of on the right-hand side of (A.2) the indices K and J of the deformation gradient can be exchanged due to compatibility, that is

$$\begin{aligned} F_{iK} &= \frac{\partial x_i}{\partial X_K} \\ \Rightarrow F_{iK,J} &= \frac{\partial^2 x_i}{\partial X_K \partial X_J} = \frac{\partial^2 x_i}{\partial X_J \partial X_K} = F_{iJ,K}. \end{aligned} \tag{A.4}$$

With assistance of these auxiliary results, the material volume force reads

$$\begin{aligned} \boldsymbol{B}_0 &= -P_{iJ}\,F_{iJ,K} + P_{iJ}\,F_{iJ,K} - \frac{\partial U_0}{\partial X_K}|_{\text{expl.}} - F_{Ki}\,b_{0i} \\ &= -\frac{\partial U_0}{\partial \boldsymbol{X}}|_{\text{expl.}} - \boldsymbol{F}^t\cdot\boldsymbol{b}_0. \end{aligned} \tag{A.5}$$

In an analogous manner the connection between the volume forces $\boldsymbol{B}_t$ and $\boldsymbol{b}_t$ is established. Starting point for this relation is the quasi-static balance of momentum

formulated in terms of the Cauchy stress

$$\boldsymbol{b}_t = -\operatorname{div} \boldsymbol{\sigma}, \tag{A.6}$$

and the connection between the Cauchy stress and the material two-point stress, which yields

$$\boldsymbol{b}_t = -\operatorname{div} (U_t \boldsymbol{I} - \boldsymbol{f}^t \cdot \boldsymbol{p}^t). \tag{A.7}$$

Straight-forward computation results in the desired correlation

$$\boldsymbol{b}_t = -\frac{\partial U_t}{\partial \boldsymbol{x}}|_{\text{expl.}} - \boldsymbol{f}^t \cdot \boldsymbol{B}_t, \tag{A.8}$$

or respectively

$$\boldsymbol{B}_t = \boldsymbol{F}^t \cdot \left[-\frac{\partial U_t}{\partial \boldsymbol{x}}|_{\text{expl.}} - \boldsymbol{b}_t \right]. \tag{A.9}$$

B Useful Integral Relations

In the sequel, useful integral transformations which are connected to the homogenization of material stresses are developed and summarized. Please note, that here the more general case of a microscopic graded material is considered, and it is assumed that the spatial volume forces vanish which is a consequence of the assumed periodic boundary conditions. In the case of a non-graded material, the terms depending on the explicit derivative of the strain energy function with respect to the material or spatial position, respectively, cancel out. First of all, the sum of the boundary and the interface integral over the dyadic product of the Eshelby tractions and the spatial positions are regarded.

$$\int\limits_{\partial\mathscr{B}_0} \boldsymbol{T}_0 \otimes \boldsymbol{x}\ \mathrm{d}A + \int\limits_{\mathscr{S}_0} \boldsymbol{T}_0^s \otimes \boldsymbol{x}\ \mathrm{d}A = \int\limits_{\partial\mathscr{B}_0} [\boldsymbol{\Sigma}\cdot\boldsymbol{N}] \otimes \boldsymbol{x}\ \mathrm{d}A + \int\limits_{\mathscr{S}_0} [[\![\boldsymbol{\Sigma}]\!]\cdot\boldsymbol{N}] \otimes \boldsymbol{x}\ \mathrm{d}A. \tag{B.1}$$

In index notation (B.1) reads

$$\int\limits_{\partial\mathscr{B}_0} \Sigma_{IJ} N_J x_k\ \mathrm{d}A + \int\limits_{\mathscr{S}_0} [\![\Sigma]\!]_{IJ} N_J x_k\ \mathrm{d}A = \int\limits_{\partial\mathscr{B}_0} \left[x_k \Sigma_{IJ}\right] N_J\ \mathrm{d}A + \int\limits_{\mathscr{S}_0} \left[x_k [\![\Sigma]\!]_{IJ}\right] N_J\ \mathrm{d}A, \tag{B.2}$$

and thus by application of the Gauß integral theorem and the product rule results in

$$\int\limits_{\mathscr{B}_0} \left(x_k \Sigma_{IJ}\right)_{,J}\ \mathrm{d}V = \int\limits_{\mathscr{B}_0} \left[\underbrace{x_{k,J}}_{F_{kJ}} \Sigma_{IJ} + x_k \underbrace{\Sigma_{IJ,J}}_{-B_{0I}}\right]\ \mathrm{d}V. \tag{B.3}$$

The connection between material and spatial volume elements $\mathrm{d}V = j\,\mathrm{d}v$ and switching back to tensor notation transforms (B.3) into

$$\int\limits_{\mathscr{B}_t} \left[j\,\boldsymbol{\Sigma}\cdot\boldsymbol{F}^t - j\,\boldsymbol{B}_0 \otimes \boldsymbol{x}\right]\ \mathrm{d}v = \int\limits_{\mathscr{B}_t} \left[\boldsymbol{p} - \boldsymbol{B}_t \otimes \boldsymbol{x}\right]\ \mathrm{d}v. \tag{B.4}$$

Finally, by application of (A.9) the desired integral reads

$$\int\limits_{\mathscr{B}_t} \left[\boldsymbol{p} + \left[\boldsymbol{F}^t \cdot \frac{\partial U_t}{\partial \boldsymbol{x}}\Big|_{\text{expl.}}\right] \otimes \boldsymbol{w}\right]\ \mathrm{d}v, \tag{B.5}$$

and thus by means of the definitions of the averaged two-point stress

$$\frac{1}{V_t}\left[\int\limits_{\partial\mathscr{B}_0} \boldsymbol{T}_0 \otimes \boldsymbol{x}\ \mathrm{d}A + \int\limits_{\mathscr{S}_0} \boldsymbol{T}_0^s \otimes \boldsymbol{x}\ \mathrm{d}A\right] = \bar{\boldsymbol{p}}, \tag{B.6}$$

is valid. In an analogous manner, it can be shown that also

$$\frac{1}{V_0}\left[\int\limits_{\partial\mathscr{B}_t} \boldsymbol{T}_t \otimes \boldsymbol{X}\ \mathrm{d}a + \int\limits_{\mathscr{S}_t} \boldsymbol{T}_t^s \otimes \boldsymbol{X}\ \mathrm{d}a\right] = \bar{\boldsymbol{\Sigma}}, \tag{B.7}$$

holds.

Another integral of interest is the sum of the boundary and the interface integral of the dyadic product of the Eshelby tractions and the spatial fluctuations

$$\int\limits_{\partial\mathscr{B}_0} \boldsymbol{T}_0 \otimes \boldsymbol{w}\ \mathrm{d}A + \int\limits_{\mathscr{S}_0} \boldsymbol{T}_t^s \otimes \boldsymbol{w}\ \mathrm{d}A. \tag{B.8}$$

By application of the Gauß integral theorem and the product rule, the integral as given in equation (B.8) can be transformed into

$$\int\limits_{\mathscr{B}_0} \left[\boldsymbol{\Sigma} \cdot \left(\nabla_{\boldsymbol{X}} \boldsymbol{w}\right)^t - \boldsymbol{B}_0 \otimes \boldsymbol{w}\right]\ \mathrm{d}V. \tag{B.9}$$

Therein, the gradient with respect to material coordinates can be substituted by the gradient with respect to spatial coordinates via

$$\nabla_{\boldsymbol{X}} \boldsymbol{w} = \nabla_{\boldsymbol{x}} \boldsymbol{w} \cdot \boldsymbol{F}, \tag{B.10}$$

and thus by a transformation from the material domain $\mathscr{B}_0$ to the spatial domain $\mathscr{B}_t$ (B.10) results in

$$\int\limits_{\mathscr{B}_t} \left[\boldsymbol{p} \cdot \left(\nabla_{\boldsymbol{x}} \boldsymbol{w}\right)^t - \boldsymbol{B}_t \otimes \boldsymbol{w}\right]\ \mathrm{d}v = \int\limits_{\mathscr{B}_t} \left[\boldsymbol{p} \cdot \left(\nabla_{\boldsymbol{x}} \boldsymbol{w}\right)^t + \left[\boldsymbol{F}^t \cdot \frac{\partial U_t}{\partial \boldsymbol{x}}|_{\text{expl.}}\right] \otimes \boldsymbol{w}\right]\ \mathrm{d}v. \tag{B.11}$$

In summary, it holds

$$\int\limits_{\partial\mathscr{B}_0} \boldsymbol{T}_0 \otimes \boldsymbol{w}\ \mathrm{d}A + \int\limits_{\mathscr{S}_0} \boldsymbol{T}_t^s \otimes \boldsymbol{w}\ \mathrm{d}A = \int\limits_{\mathscr{B}_t} \left[\boldsymbol{p} \cdot \left(\nabla_{\boldsymbol{x}} \boldsymbol{w}\right)^t + \left[\boldsymbol{F}^t \cdot \frac{\partial U_t}{\partial \boldsymbol{x}}|_{\text{expl.}}\right] \otimes \boldsymbol{w}\right]\ \mathrm{d}v, \tag{B.12}$$

and in a similar proceeding it can be shown that also

$$\int_{\partial \mathscr{B}_t} \boldsymbol{T}_t \otimes \boldsymbol{w} \, \mathrm{d}a + \int_{\mathscr{S}_t} \boldsymbol{T}_t^s \otimes \boldsymbol{w} \, \mathrm{d}a = \int_{\mathscr{B}_0} \left[\boldsymbol{\Sigma} \cdot \left(\nabla_{\boldsymbol{X}} \boldsymbol{w} \right)^t + \frac{\partial U_0}{\partial \boldsymbol{X}} |_{\text{expl.}} \otimes \boldsymbol{w} \right] \mathrm{d}V, \qquad \text{(B.13)}$$

is valid.

C Material Hill-Mandel Type Conditions

In the sequel, the material Hill-Mandel type conditions in terms of the material two-point stress are derived explicitly for a graded microscopic material for different homogenization approaches. In the case of a microscopic standard material, for which the stored energy functional does not depend on the material position, the same derivations are valid, but the terms containing the explicit derivatives of the stored energy functional with respect to the coordinates vanish.

C.1 Material Homogenization based on Macroscopic Spatial Variables

Starting point is the macroscopic virtual work which for this approach due to the vanishing macroscopic volume forces reads

$$p^*_{tM} = \mathrm{d}_\delta \boldsymbol{f}_M : \boldsymbol{p}^*_M. \tag{C.1}$$

Application of the relation between the macroscopic and the averaged material two-point stress, see equation (4.49), yields

$$p^*_{tM} = \mathrm{d}_\delta \boldsymbol{f}_M : \bar{\boldsymbol{p}} - \mathrm{d}_\delta \boldsymbol{f}_M : \frac{1}{V_t} \int\limits_{\mathscr{B}_t} \left[\left[\boldsymbol{F}^t \cdot \left(\nabla_{\boldsymbol{x}} \boldsymbol{w} \right)^t \cdot \boldsymbol{f}^t \right] \cdot \boldsymbol{p} + \left[\boldsymbol{F}^t \cdot \frac{\partial U_t}{\partial \boldsymbol{x}} |_{\text{expl.}} \right] \otimes \boldsymbol{X} \right] \mathrm{d}v. \tag{C.2}$$

In a next step, the definition of the averaged two-point stress (4.9) is applied

$$\begin{aligned} p^*_{tM} &= \mathrm{d}_\delta \boldsymbol{f}_M : \frac{1}{V_t} \left[\int\limits_{\partial \mathscr{B}_t} \boldsymbol{T}_t \otimes \boldsymbol{x} \, \mathrm{d}a + \int\limits_{\mathscr{S}_t} \boldsymbol{T}^s_t \otimes \boldsymbol{x} \, \mathrm{d}a \right] \\ &- \mathrm{d}_\delta \boldsymbol{f}_M : \frac{1}{V_t} \int\limits_{\mathscr{B}_t} \left[\left[\boldsymbol{F}^t \cdot \left(\nabla_{\boldsymbol{x}} \boldsymbol{w} \right)^t \cdot \boldsymbol{f}^t \right] \cdot \boldsymbol{p} + \left[\boldsymbol{F}^t \cdot \frac{\partial U_t}{\partial \boldsymbol{x}} |_{\text{expl.}} \right] \otimes \boldsymbol{X} \right] \mathrm{d}v, \end{aligned} \tag{C.3}$$

and with the material scale-transition (4.15) the macroscopic virtual work results in

$$\begin{aligned} p^*_{tM} &= \frac{1}{V_t}\left[\int\limits_{\partial\mathscr{B}_t} \boldsymbol{T}_t \cdot \mathrm{d}_\delta \boldsymbol{\Phi}\, \mathrm{d}a + \int\limits_{\mathscr{S}_t} \boldsymbol{T}^s_t \cdot \mathrm{d}_\delta \boldsymbol{\Phi}\, \mathrm{d}a\right] \\ &+ \frac{1}{V_t}\left[\int\limits_{\partial\mathscr{B}_t} \boldsymbol{T}_t\, \mathrm{d}a + \int\limits_{\mathscr{S}_t} \boldsymbol{T}^s_t\, \mathrm{d}a\right] \cdot \left[\mathrm{d}_\delta \boldsymbol{f}_M \cdot \boldsymbol{\varphi}_M\right] \\ &+ \mathrm{d}_\delta \boldsymbol{f}_M : \frac{1}{V_t}\left[\int\limits_{\partial\mathscr{B}_t} \boldsymbol{T}_t \otimes \boldsymbol{w}\, \mathrm{d}a + \int\limits_{\mathscr{S}_t} \boldsymbol{T}^s_t \otimes \boldsymbol{w}\, \mathrm{d}a\right] \\ &- \mathrm{d}_\delta \boldsymbol{f}_M : \frac{1}{V_t}\int\limits_{\mathscr{B}_t}\left[\left[\boldsymbol{F}^t \cdot \left(\nabla_{\boldsymbol{x}} \boldsymbol{w}\right)^t \cdot \boldsymbol{f}^t\right] \cdot \boldsymbol{p} + \left[\boldsymbol{F}^t \cdot \frac{\partial U_t}{\partial \boldsymbol{x}}|_{\text{expl.}}\right] \otimes \boldsymbol{X}\right] \mathrm{d}v. \end{aligned} \tag{C.4}$$

Therein, the first term on the right-hand side can be identified with the average of the microscopic virtual work $\bar{p}_t$ whereas the second term can be transformed via (A.9) to

$$\frac{1}{V_t}\left[\int\limits_{\partial\mathscr{B}_t} \boldsymbol{T}_t\, da \int\limits_{\mathscr{S}_t} \boldsymbol{T}^s_t\, \mathrm{d}a\right] \cdot \left[\mathrm{d}_\delta \boldsymbol{f}_M \cdot \boldsymbol{\varphi}_M\right] = \mathrm{d}_\delta \boldsymbol{f}_M \cdot \frac{1}{V_t}\int\limits_{\mathscr{B}_t}\left[\boldsymbol{F}^t \cdot \frac{\partial U_t}{\partial \boldsymbol{x}}|_{\text{expl.}}\right] \otimes \boldsymbol{\varphi}_M\, \mathrm{d}v. \tag{C.5}$$

The last term in (C.4) can be reformulated by means of the Gauß integral theorem and thus results in

$$\int\limits_{\partial\mathscr{B}_t} \boldsymbol{T}_t \otimes \boldsymbol{w}\, \mathrm{d}a + \int\limits_{\mathscr{S}_t} \boldsymbol{T}^s_t \otimes \boldsymbol{w}\, \mathrm{d}a = \int\limits_{\mathscr{B}_t}\left[\boldsymbol{p} \cdot (\nabla_{\boldsymbol{x}} \boldsymbol{w})^t + \left[\boldsymbol{F}^t \cdot \frac{\partial U_t}{\partial \boldsymbol{x}}|_{\text{expl.}}\right] \otimes \boldsymbol{w}\right] \mathrm{d}v. \tag{C.6}$$

Summing up these auxiliary results the macroscopic virtual work is given by

$$\begin{aligned} p^*_{tM} = \bar{p}_t + \mathrm{d}_\delta \boldsymbol{f}_M : \frac{1}{V_t} \int\limits_{\mathscr{B}_t} & \left[\boldsymbol{p} \cdot (\nabla_{\boldsymbol{x}} \boldsymbol{w})^t - \left[\boldsymbol{F}^t \cdot \left(\nabla_{\boldsymbol{x}} \boldsymbol{w}\right)^t \cdot \boldsymbol{f}^t\right] \cdot \boldsymbol{p}\right. \\ & - \left.\left[\boldsymbol{F}^t \cdot \frac{\partial U_t}{\partial \boldsymbol{x}}|_{\text{expl.}}\right] \otimes \left[\boldsymbol{x} - \boldsymbol{\varphi}_M - \boldsymbol{w}\right] \right] \mathrm{d}v. \end{aligned} \tag{C.7}$$

Finally, application of the spatial scale-transition (3.8) to the last term on the right-hand side yields the internal extra contribution as

$$\bar{p}_t^{*\,\mathrm{int}} = \mathrm{d}_\delta \boldsymbol{f}_M : \frac{1}{V_t} \int\limits_{\mathscr{B}_t} [\, \boldsymbol{p} \cdot (\nabla_{\boldsymbol{x}} \boldsymbol{w})^t - \left[\boldsymbol{F}^t \cdot (\nabla_{\boldsymbol{x}} \boldsymbol{w})^t \cdot \boldsymbol{f}^t \right] \cdot \boldsymbol{p} - \left[\boldsymbol{F}^t \cdot \frac{\partial U_t}{\partial \boldsymbol{x}}|_{\mathrm{expl.}} \right] \otimes \left[\boldsymbol{F}_M \cdot \boldsymbol{X} \right] \,] \, \mathrm{d}v. \tag{C.8}$$

In the case of non-graded microscopic material, the contribution containing the explicit derivative of the stored strain energy vanishes and thus the internal part reduces to

$$\bar{p}_t^{*\,\mathrm{int}} = \mathrm{d}_\delta \boldsymbol{f}_M : \frac{1}{V_t} \int\limits_{\partial \mathscr{B}_t} \left[\boldsymbol{p} \cdot (\nabla_{\boldsymbol{x}} \boldsymbol{w})^t \right] - \left[\boldsymbol{F}^t \cdot (\nabla_{\boldsymbol{x}} \boldsymbol{w})^t \cdot \boldsymbol{f}^t \right] \cdot \boldsymbol{p} \, \mathrm{d}v. \tag{C.9}$$

C.2 Material Homogenization based on Averaged Eshelby Stress Tensor

For this approach the macroscopic virtual work also contains the volume forces due to the fact that they are not vanishing generally. Thus, the virtual work reads

$$p_{tM} = \mathrm{d}_\delta \boldsymbol{f}_M : \boldsymbol{p}_M - \mathrm{d}_\delta \boldsymbol{\Phi}_M \cdot \boldsymbol{B}_{tM}. \tag{C.10}$$

Application of the relation between the macroscopic and the averaged material two-point stress, see equation (4.73), and the corresponding volume forces (4.75) yields

$$p_{tM} = \mathrm{d}_\delta \boldsymbol{f}_M : \bar{\boldsymbol{p}} - \mathrm{d}_\delta \boldsymbol{f}_M : \bar{\boldsymbol{p}}^+ - \mathrm{d}_\delta \boldsymbol{\Phi}_M \cdot \left[\frac{1}{V_t} \int\limits_{\mathscr{B}_t} \boldsymbol{F}^t \cdot \frac{\partial U_t}{\partial \boldsymbol{x}}|_{\mathrm{expl.}} \, \mathrm{d}v - \mathrm{div}\, \bar{\boldsymbol{p}}^+ \right]. \tag{C.11}$$

In a next step, the definition of the material two-point stress (4.9) is inserted

$$\begin{aligned} p_{tM} &= \mathrm{d}_\delta \boldsymbol{f}_M : \frac{1}{V_t} \left[\int\limits_{\partial \mathscr{B}_t} \boldsymbol{T}_t \otimes \boldsymbol{x} \, \mathrm{d}a + \int\limits_{\mathscr{S}_t} \boldsymbol{T}_t^s \otimes \boldsymbol{x} \, \mathrm{d}a \right] \\ &\quad - \mathrm{d}_\delta \boldsymbol{f}_M : \bar{\boldsymbol{p}}^+ - \mathrm{d}_\delta \boldsymbol{\Phi}_M \cdot \left[\frac{1}{V_t} \int\limits_{\mathscr{B}_t} \boldsymbol{F}^t \cdot \frac{\partial U_t}{\partial \boldsymbol{x}}|_{\mathrm{expl.}} \, \mathrm{d}v - \mathrm{div}\, \bar{\boldsymbol{p}}^+ \right], \end{aligned} \tag{C.12}$$

and by means of the definition of the material scale-transition (4.15) the macroscopic virtual work results in

$$\begin{aligned} p_{tM} &= \frac{1}{V_t}\left[\int_{\partial\mathscr{B}_t} \boldsymbol{T}_t \cdot \mathrm{d}_\delta\boldsymbol{\Phi}\,\mathrm{d}a + \int_{\mathscr{S}_t} \boldsymbol{T}_t^s \cdot \mathrm{d}_\delta\boldsymbol{\Phi}\,\mathrm{d}a\right] \\ &+ \frac{1}{V_t}\left[\int_{\partial\mathscr{B}_t} \boldsymbol{T}_t\,\mathrm{d}a + \int_{\mathscr{S}_t} \boldsymbol{T}_t^s\,\mathrm{d}a\right] \cdot \left[\mathrm{d}_\delta\boldsymbol{f}_M \cdot \boldsymbol{\varphi}_M\right] \\ &+ \frac{1}{V_t}\left[\int_{\partial\mathscr{B}_t} \boldsymbol{T}_t \cdot \boldsymbol{w}\,\mathrm{d}a + \int_{\mathscr{S}_t} \boldsymbol{T}_t^s \cdot \boldsymbol{w}\,\mathrm{d}a\right] \\ &- \mathrm{d}_\delta\boldsymbol{f}_M : \bar{\boldsymbol{p}}^+ - \mathrm{d}_\delta\boldsymbol{\Phi}_M \cdot \left[\frac{1}{V_t}\int_{\mathscr{B}_t} \boldsymbol{F}^t \cdot \frac{\partial U_t}{\partial \boldsymbol{x}}|_{\text{expl.}}\,\mathrm{d}v - \operatorname{div}\bar{\boldsymbol{p}}^+\right]. \end{aligned} \tag{C.13}$$

In analogy to the previous section, the first three terms on the right-hand side of this equation are reformulated and thus p_{tM} reads

$$\begin{aligned} p_{tM} &= \bar{p}_t + \mathrm{d}_\delta\boldsymbol{f}_M : \frac{1}{V_t}\int_{\mathscr{B}_t}\left[\boldsymbol{p}\cdot\left(\nabla_{\boldsymbol{x}}\boldsymbol{w}\right)^t + \left[\boldsymbol{F}^t \cdot \frac{\partial U_t}{\partial \boldsymbol{x}}|_{\text{expl.}}\right] \otimes \left[\boldsymbol{w} + \boldsymbol{\varphi}_M\right]\right]\mathrm{d}v \\ &- \mathrm{d}_\delta\boldsymbol{f}_M : \bar{\boldsymbol{p}}^+ - \mathrm{d}_\delta\boldsymbol{\Phi}_M \cdot \left[\frac{1}{V_t}\int_{\mathscr{B}_t} \boldsymbol{F}^t \cdot \frac{\partial U_t}{\partial \boldsymbol{x}}|_{\text{expl.}}\,\mathrm{d}v - \operatorname{div}\bar{\boldsymbol{p}}^+\right]. \end{aligned} \tag{C.14}$$

The definition of the extra term $\bar{\boldsymbol{p}}^+$ –see equation (4.74)– corresponds to the first integral at the right-hand side of (C.14) and thus $\mathrm{d}_\delta\boldsymbol{f}_M : \bar{\boldsymbol{p}}^+$ cancels out. Finally, by insertion of the macroscopic volume forces (4.75), the Hill-Mandel type condition in terms of $\boldsymbol{p}_M$ is given by

$$p_{tM} = \bar{p}_t + \bar{p}_t^{\text{int}}, \tag{C.15}$$

wherein for graded micro-materials

$$\bar{p}_t^{\text{int}} = \mathrm{d}_\delta\boldsymbol{\Phi}_M \cdot \left[\frac{1}{V_t}\int_{\partial\mathscr{B}_t}\left[\boldsymbol{F}^t \cdot \frac{\partial U_t}{\partial \boldsymbol{x}}|_{\text{expl.}}\right]\mathrm{d}v - \operatorname{div}\bar{\boldsymbol{p}}^+\right], \tag{C.16}$$

holds. For the special case of non-graded materials this term reduces to

$$\bar{p}_t^{\text{int}} = -\,\mathrm{d}_\delta\boldsymbol{\Phi}_M \cdot \operatorname{div}\bar{\boldsymbol{p}}^+. \tag{C.17}$$

Bibliography

[1] D. J. Bacon, D. M. Barnett, and R. O. Scattergood. Anisotropic continuum theory of lattice defects. *Prog. Mat. Sci.*, 23:51–262, 1979.

[2] T. Belytschko, W. K. Liu, and B. Moran. *Nonlinear Finite Elements of Contiunua and Structures*. Wiley, Chichester, 2000.

[3] A. Bensoussan, J. L. Lions, and G. Papanicolaoi. *Asymptotic Analysis for Periodic Structures*. Studies in Mathematics and its Applications. North-Holland, Amsterdam, 1978.

[4] Y. Benveniste. A new approach to the application of Mori-Tanaka's theory in composite materials. *MM*, 6:147–157, 1987.

[5] J. Betten. *Kontinuumsmechanik*. Springer, Berlin, 2001.

[6] J. Bonet and R. D. Wood. *Nonlinear Continuum Mechanics for Finite Element Analysis*. Cambridge University Press, Cambridge, 1997.

[7] M. Born and K. Huang. *Dynamical Theory of Crystal Lattices*. Clarendon Press, Oxford, 1954.

[8] V. Buryachenko. *Micromechanics of Heterogeneous Materials*. Springer, Berlin, 2007.

[9] J. L. Chaboche. Continuous damage mechanics: A tool to describe phenomena before crack initiation. *Nucl. Eng. Des.* , 64:233–247, 1981.

[10] R. D. Cook, D. S. Malkus, and M. E. Plesha. *Concepts and Applications of Finite Element Analysis*. Wiley, Chichester, 1989.

[11] F. Costanzo, G. L. Gray, and P. C. Andia. On the definitions of effective stress and deformation gradient for use in MD. Hill's macro-homogeneity and the virial theorem. *Int. J. Eng. Sci.*, 43:533–555, 2005.

[12] R. Denzer, F. J. Barth, and P. Steinmann. Studies in elastic fracture mechanics based on the material force method. *Int. J. Numer. Meth. Eng.*, 58:1817–1835, 2003.

[13] F. Devries, H. Dumontet, G. Duvaut, and F. Lene. Homogenization and damage for composite structures. *Int. J. Numer. Meth. Eng.*, 27:285–298, 1989.

[14] J. L. Ericksen. The Cauchy and Born hypothesis for crystals. In *Phase Transformations and Material Instabilities in Solids*, pages 61–77. Academic Press, 1984.

[15] J. D. Eshelby. The determination of the field of an ellipsoidal inclusion and related problems. *Proc. Roy. Soc. Lond. A*, 241:376–396, 1957.

[16] F. Feyel. Multiscale FE^2 elastoviscoplastic analysis of composite structures. *Comput. Mater. Sci.*, 16:344–354, 1999.

[17] F. Feyel. A multilevel finite element method (FE^2) to describe the response of highly non-linear structures using generalized continua. *Comput. Meth. Appl. Mech. Eng.*, 192:3233–3244, 2003.

[18] F. Feyel and J. L. Chaboche. FE^2 multiscale approach for modelling the elastoviscoplastic behaviour of long fibre SiC/Ti composite materials. *Comput. Meth. Appl. Mech. Eng.*, 183:309–330, 2000.

[19] J. Fish and Q. Yu. Multiscale damage modeling for composite materials. *Int. J. Numer. Meth. Eng.*, 52:161–192, 2001.

[20] J. Fish, Q. Yu, and K. L. Shek. Computational damage mechanics for composite materials based on mathematical homogenization. *Int. J. Numer. Meth. Eng.*, 45:1657–1679, 1999.

[21] P. A. Fotiu and S. Nemat-Nasser. Overall properties of elastic-visoplastic periodic composites. *Int. J. Plast.*, 12:163–190, 1996.

[22] G. Friesecke and F. Theil. Validity and failure of the Cauchy-Born hypothesis in a two-dimensional mass-spring lattice. *J. Nonlinear Sci.*, 12:445–478, 2002.

[23] M. G. D. Geers, V. G. Kouznetsova, and W. A. M. Brekelmans. Multi-scale computational homogenization: Trends and challenges. *J. Comput. Appl. Math.*, 234:2175–2182, 2010.

[24] S. Ghosh, K. Lee, and S. Moorthy. Multiple scale analysis of heterogeneous elastic structures using homogenization theory and Voronoï cell finite element method. *Int. J. Solid Struct.*, 32:27–62, 1995.

[25] S. Ghosh, K. Lee, and S. Moorthy. Two scale analysis of heterogeneous elastic-plastic materials with asymptotic homogenization and Voronoï finite element model. *Comput. Meth. Appl. Mech. Eng.*, 132:63–116, 1996.

[26] S. Ghosh, K. Lee, and P. Raghavan. A multi-level computational model for multi-scale damage analysis in composite and porous materials. *Int. J. Solid Struct.*, 38:2335–2385, 2001.

[27] D. Gross and T. Seelig. *Bruchmechanik: Mit einer Einführung in die Mikromechanik*. Springer, Berlin, 2007.

[28] J. M. Guedes and N. Kikuchi. Preprocessing and postprocessing for materials based on the homogenization method with adaptive finite element methods. *Comput. Meth. Appl. Mech. Eng.*, 83:143–198, 1990.

[29] M. E. Gurtin. *Configurational Forces as Basic Concepts of Continuum Physics*. Springer, New York, 2000.

[30] Z. Hashin. The elastic moduli of heterogeneous materials. *J. Appl. Mech.*, 29:143–150, 1962.

[31] Z. Hashin. Analysis of composite materials. A survey. *J. Appl. Mech.*, 50:481–505, 1983.

[32] Z. Hashin and S. Shtrikman. On some variational principles in anisotropic and nonhomogeneous elasticity. *J. Mech. Phys. Solid.*, 10:335–342, 1962.

[33] Z. Hashin and S. Shtrikman. A variational approach to the theory of the elastic behaviour of polycristals. *J. Mech. Phys. Solid.*, 10:343–352, 1962.

[34] Z. Hashin and S. Shtrikman. A variational approach to the theory of the elastic behaviour of multiphase materials. *J. Mech. Phys. Solid.*, 11:127–140, 1963.

[35] R. Hill. Elastic properties of reinforced solids: Some theoretical principles. *J. Mech. Phys. Solid.*, 11:357–372, 1963.

[36] R. Hill. A self-consistent mechanics of composite materials. *J. Mech. Phys. Solid.*, 13:213–222, 1965.

[37] R. Hill. On constitutive macro-variables for heterogeneous solids at finite strain. *Proc. Roy. Soc. Lond. A*, 326:131–147, 1972.

[38] C. B. Hirschberger, S. Ricker, P. Steinmann, and N. Sukumar. Computational multiscale modelling of heterogeneous material layers. *Eng. Fract. Mech.*, 76:793–812, 2009.

[39] G. A. Holzapfel. *Nonlinear Solid Mechanics*. Wiley, Chichester, 2001.

[40] T. J. R. Hughes. *The Finite Element Method*. Prentice Hall, Englewood Cliffs, 1987.

[41] R. Jänicke, S. Diebels, H. G. Sehlhorst, and A. Düster. Two-scale modelling of micromorphic continua. *Continuum Mech. Thermodyn.*, 21:297–315, 2009.

[42] L. M. Kachanov. Über die Zeit der Zerstörung unter den Bedingungen des Kriechens. *Izv. Akad. Nauk SSSR, Otd. Tekh. Nauk*, 8:26–31, 1958.

[43] L. M. Kachanov. *Introduction to Continuum Damage Mechanics*. M. Nijhoff, Dordrecht, 1986.

[44] P. Kanouté, D. P. Boso, J. L. Chaboche, and B. A. Schrefler. Multiscale methods for composites: A review. *Arch. Comput. Meth. Engng.*, 16:31–75, 2009.

[45] R. Kienzler and G. Herrmann. *Mechanics in Material Space*. Springer, Berlin, 2000.

[46] B. Klein. *Leichtbau-Konstruktion: Berechnungsgrundlagen und Gestaltung*. Vieweg, Braunschweig, 2007.

[47] J. K. Knowles and E. Sternberg. On a class of conservation laws in linearized and finite elastostatics. *Arch. Rat. Mech. Anal.*, 44:187–211, 1972.

[48] V. Kouznetsova. *Computational homogenization for the multi-scale analysis of multi-phase materials*. PhD thesis, Technische Universiteit Eindhoven, Netherlands, 2002.

[49] V. Kouznetsova, W. A. M. Brekelmans, and F. P. T. Baaijens. An approach to micro-macro modeling of heterogeneous materials. *Comput. Mech.*, 27:37–48, 2001.

[50] V. Kouznetsova, M. G. D. Geers, and W. A. M. Brekelmans. Multi-scale constitutive modelling of heterogeneous material with a gradient enhanced computational homogenization scheme. *Int. J. Numer. Meth. Eng.*, 54:1235–1260, 2002.

[51] V. Kouznetsova, M. G. D. Geers, and W. A. M. Brekelmans. Multi-scale second-order computational homogenization of multi-phase materials: A nested finite element method. *Comput. Meth. Appl. Mech. Eng.*, 193:5525–5550, 2004.

[52] E. Kröner. Berechnung der elastischen Konstanten des Vielkristalls aus den Konstanten des Einkristalls. *Z. Phys.*, 151:504–518, 1958.

[53] E. Kuhl, H. Askes, and P. Steinmann. An ALE formulation based on spatial and material settings of continuum mechanics. Part 1: Generic hyperelastic formulation. *Comput. Meth. Appl. Mech. Eng.*, 193:4207–4222, 2004.

[54] J. Lemaitre. Evaluation of dissipation and damage in metals. *Proc. I.C.M. Kyoto*, 1:540–549, 1971.

[55] G. A. Maugin. *Material Inhomogeneities in Elasticity*. Chapman and Hall, Boca Raton, 1993.

[56] C. Miehe. Strain-driven homogenization of inelastic microstructures and composites based on an incremental variational formulation. *Int. J. Numer. Meth. Eng.*, 55:1285–1322, 2002.

[57] C. Miehe. Computational micro-to-macro transitions for discretized microstructures of heterogeneous materials at finite strains based on the minimization of averaged incremental energy. *Comput. Meth. Appl. Mech. Eng.*, 192:559–591, 2003.

[58] C. Miehe and A. Koch. Computational micro-to-macro transitions of discretized microstructures undergoing small strains. *Arch. Appl. Mech.*, 72:300–317, 2002.

[59] C. Miehe, J. Schröder, and M. Becker. Computational homogenization analysis in finite elasticity: Material and structural instabilities on the micro- and macro-scales of periodic composites and their interaction. *Comput. Meth. Appl. Mech. Eng.*, 191:4971–5005, 2002.

[60] C. Miehe, J. Schröder, and J. Schotte. Computational homogenization analysis in finite plasticity simulation of texture development in polycrystalline materials. *Comput. Meth. Appl. Mech. Eng.*, 171:387–418, 1999.

[61] T. Mori and K. Tanaka. Average stress in matrix and average elastic energy of materials with misfitting inclusions. *Acta Metall.*, 21:571–574, 1973.

[62] H. Moulinec and P. Suquet. A numerical method for computing the overall response of nonlinear composites with complex microstructure. *Comput. Meth. Appl. Mech. Eng.*, 157:69–94, 1998.

[63] R. Müller, S. Kolling, and D. Gross. On configurational forces in the context of the Finite Element Method. *Int. J. Numer. Meth. Eng.*, 53:1557–61574, 2002.

[64] R. Müller and G. A. Maugin. On material forces and finite element discretizations. *Comput. Mech.*, 29:52–60, 2002.

[65] T. Mura. *Micromechanics of Solids with Defects*. Martinus Nijhoff Publishers, Dortrecht, 1987.

[66] S. Nemat-Nasser. Averaging theorems in finite deformation plasticity. *Mech. Mater.*, 31:493–523, 1999.

[67] S. Nemat-Nasser and M. Hori. *Micromechanics: Overall Properties of Heterogeneous Materials*. North-Holland, Amsterdam, 1999.

[68] R. W. Ogden. *Non-Linear Elastic Deformations*. Ellis Horwood Limited, Chichester, 1984.

[69] A. Reuss. Berechnung der Fliessgrenze von Mischkristallen auf Grund der Plastizitätsbedingung für Einkristalle. *Z. Angew. Math. Mech.*, 9:49–58, 1929.

[70] J. R. Rice. A path independent integral and the approximate analysis of strain concentrations by notches and cracks. *J. Appl. Mech.*, 35:379–386, 1968.

[71] S. Ricker, J. Mergheim, A. Menzel, and P. Steinmann. On variational issues in the homogenization of discrete mechanical systems. In *ECCOMAS Thematic Conference on Multi-Scale Computational Methods for Solids and Fluids, Cachan, France*, pages 221–227, 2007.

[72] S. Ricker, J. Mergheim, and P. Steinmann. On the multiscale computation of defect driving forces. *Int. J. Multiscale Comput. Eng.*, 7:457–474, 2009.

[73] S. Ricker, J. Mergheim, P. Steinmann, and R. Müller. A comparison of different approaches in the multi-scale computation of configurational forces. *Int. J. Fract.*, 166:203–214, 2010.

[74] E. Ross and K. Maile. *Werkstoffkunde für Ingenieure*. Springer, Berlin, 2008.

[75] E. Sanchez-Palenzia. Nonhomogeneous media and vibration theory. *Lecture Notes in Physics*, 217:193–278, 1980.

[76] R. Schmitt. Mikromechanische Modellierung von glasfaserverstärkten Thermoplasten. Studienarbeit, Technische Universität Kaiserslautern, Germany, 2010.

[77] J. Schröder. Homogenisierungsmethoden der nichtlinearen Kontinuumsmechanik unter Beachtung von Instabilitäten. Habilitation thesis, University of Stuttgart, Germany, 2000.

[78] H. Schürmann. *Konstruieren mit Faser-Kunststoff-Verbunden*. Springer, Berlin, 2007.

[79] J. C. Simo and J. W. Ju. Strain- and stress-based continuum damage models – I. Formulation. *Int. J. Solid Struct.*, 23:821–840, 1987.

[80] J. C. Simo and J. W. Ju. Strain- and stress-based continuum damage models – II. Computational aspects. *Int. J. Solid Struct.*, 23:841–869, 1987.

[81] R. J. M. Smit, W. A. M. Brekelmanns, and H. E. H. Meijer. Prediction of the mechanical behaviour of nonlinear heterogeneous systems by multi-level finite element modeling. *Comput. Meth. Appl. Mech. Eng.*, 155:181–192, 1998.

[82] P. Steinmann. Application of material forces to hyperelastostatic fracture mechanics I: Continuum mechanical setting. *Int. J. Solid Struct.*, 37:7371–7391, 2000.

[83] P. Steinmann, D. Ackermann, and F. J. Barth. Application of material forces to hyperelastic fracture mechanics II: Computational setting. *Int. J. Solid Struct.*, 38:5509–5526, 2001.

[84] P. Steinmann, S. Ricker, and E. Aifantis. Unconstrained and Cauchy-Born constrained atomistic systems: Deformational and configurational mechanics. *Arch. Appl. Mech.*, 2010. accepted for publication.

[85] C. Stolz. Large plastic deformation of polycrystals. In *CISM Courses and Lectures*, pages 81–108. Springer, Wien - New York, 1997.

[86] R. Sunyk. *On aspects of mixed continuum-atomistic material modelling*. PhD thesis, University of Kaiserslautern, Germany, 2004.

[87] R. Sunyk and P. Steinmann. On higher gradients in continuum-atomistic modelling. *Int. J. Solid Struct.*, 40:6877–6896, 2003.

[88] R. Sunyk and P. Steinmann. Transition to plasticity in continuum-atomistic modelling. *Multidisc. Mod. Mat. Struct.*, 2:1–38, 2006.

[89] P. M. Suquet. Local and global aspects in the mathematical theory of plasticity. In S. Sawczuk and G. Bianchi, editors, *Plasticity Today: Modelling, Methods and Applications*, pages 279–310. Elsevier, London, 1985.

[90] P. M. Suquet. Elements of homogenization for inelastic solid mechanics. In E. Sanchez-Palenzia and A. Zaoui, editors, *Lecture Notes in Physics*, volume 272, pages 193–278. Springer, Berlin, 1987.

[91] K. Tanaka and T. Mori. Note on volume integrals of the elastic field around an ellipsoidal inclusion. *J. Elasticity*, 2:199–200, 1972.

[92] K. Terada and N. Kikuchi. A class of general algorithms for multi-scale analyses of heterogeneous media. *Comput. Meth. Appl. Mech. Eng.*, 190:5427–5464, 2001.

[93] W. Voigt. Über die Beziehung zwischen den Elastizitätskonstanten isotroper Körper. *Wied. Ann.*, 38:573–587, 1889.

[94] J. R. Willis. Bounds and self-consistent estimates for the overall properties of anisotropic composites. *J. Mech. Phys. Solid.*, 25:185–202, 1977.

[95] P. Wriggers. *Nichtlineare Finite-Element-Methoden*. Springer, Berlin, 2001.

[96] G. Zanzotto. The Cauchy-Born hypothesis, nonlinear elasticity and mechanical twinning in crystals. *Acta Cryst.*, 52:839–849, 1996.

[97] O. C. Zienkiewicz and R. L. Taylor. *The Finite Element Method, Volume 1, The Basics*. Butterworth-Heinemann, Oxford, 2000.

Curriculum Vitae

Name:	Sarah Ricker
Geburtsdatum:	06.11.1980
Geburtsort:	Kaiserslautern
Nationalität:	deutsch
Familienstand:	ledig

08/1987 – 07/1991	Stresemann Grundschule, Kaiserslautern
08/1991 – 07/1997	Hohenstaufen-Gymnasium, Kaiserslautern
08/1997 – 06/2000	Albert-Schweitzer-Gymnasium, Kaiserslautern Abschluss: Allgemeine Hochschulreife
10/2000 – 07/2005	Studium der Technomathematik, Technische Universität Kaiserslautern Abschluss: Diplom Technomathematikerin
10/2005 – 09/2008	Stipendiatin im DFG-Graduiertenkolleg 814: *Ingenieurmaterialien auf verschiedenen Skalen: Experiment, Modellierung und Simulation*, Lehrstuhl für Technische Mechanik Technische Universität Kaiserslautern
10/2008 – 01/2009	Stipendiatin der TU Kaiserslautern, Lehrstuhl für Technische Mechanik
seit 02/2009	Wissenschaftliche Mitarbeiterin, Lehrstuhl für Technische Mechanik Technische Universität Kaiserslautern